Report No. BRUCRD-ESACCD-95-1R

FINAL REPORT ON

ESTEC Contract 8815/90/NL/LC(SC)

BRUNEL
UNIVERSITY

Further Radiation Evaluation of X-ray Sensitive Charge Coupled Devices (CCDs) for the XMM Telescope
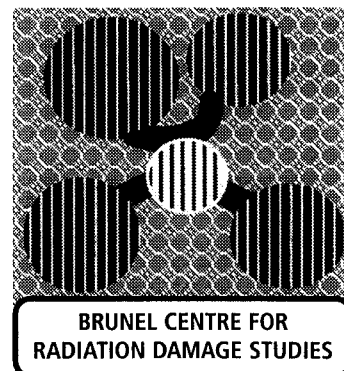
By Stephen Watts

Andrew Holmes-Siedle

Andrew Holland

20 October 1995

Prepared by Brunel University for the European Space Agency

BRUNEL CENTRE FOR
RADIATION DAMAGE STUDIES

BIBLIOGRAPHIC INFORMATION

Andrew Holmes-Siedle, Stephen Watts and Andrew Holland

FINAL REPORT ON: FURTHER RADIATION EVALUATION OF X-RAY SENSITIVE CHARGE COUPLED DEVICES (CCDs) FOR THE XMM TELESCOPE

Report No. BRUCRD-ESACCD-95-1R

FINAL REPORT ON

ESTEC CONTRACT 8815/90/NL/LC(SC)
"SUPPORT ON RADIATION EFFECTS"

FURTHER RADIATION EVALUATION OF X-RAY SENSITIVE CHARGE COUPLED DEVICES (CCDs) FOR THE XMM TELESCOPE

by

Stephen Watts
Andrew Holmes-Siedle
Andrew Holland

20 October 1995

Prepared by:

Centre for Radiation Damage Studies
Physics Department, Brunel University
Uxbridge, UB8 3PH, Middlesex, U.K.
Telephone: +44 1895 27 40 00
Fax: +44 1895 27 23 91
Technical Management by: Dr. Stephen Watts
Principal Investigator: Prof. Andrew Holmes-Siedle
Co-Investigator: Dr. Andrew Holland of Leicester University

Prepared for:
ESTEC-QCA, PO Box 299
2200AG Noordwijk-zh, The Netherlands
Tel: 00 31 1719 83335
Fax: 00 31 1719 46437   Technical Manager : Mr Bengt Johlander

Andrew Holmes-Siedle, Stephen Watts and Andrew Holland

FINAL REPORT ON: FURTHER RADIATION EVALUATION OF X-RAY SENSITIVE CHARGE COUPLED DEVICES (CCDs) FOR THE XMM TELESCOPE

Abstract

The report discusses the collaboration of Brunel and Leicester Universities, on the evaluation of new CCD technology for X-ray astronomy, in particular the XMM mission (EPIC and RGS instruments). Two tasks, work orders 1 and 2 of ESA-ESTEC contract 8815/90/NL/LC(SC) are described. Work Order 1 in 1990-91 is briefly described. A new set of CCD devices irradiated in Work Order 2 of ESA Contract 8815 was irradiated with high-energy protons in late1994. The latter experiments are described in detail and extensive analysis and discussion is presented. The discussion section deals with many of the topics required for the understanding of radiation effects in CCDs. The report is rounded off with a description of tools for in-flight prediction, recommendations for further work and an appendix giving the basic measurement results.

LIST OF CONTENTS

LIST OF FIGURES

EUROPEAN SPACE AGENCY CONTRACT
REPORT

The work described in this
report was done under ESA
contract. Responsibility for
the contents resides with the
author or the organisation
that prepared it.

FURTHER RADIATION EVALUATION OF X-RAY SENSITIVE CHARGE COUPLED DEVICES (CCDs) FOR THE XMM TELESCOPE

1. INTRODUCTION

1.1 General

The CCD radiation test project is part of ESA's Technological Research Programme, supervised by the QCA Department, ESTEC. Contract No. 8815/90/NL/PB(SC), Work Order 2 with Brunel University formed a part of this. The objective of the above contract is to characterise the effect of space radiation on scientific Charge-Coupled Devices (CCDs), specifically the devices made by EEV, Chelmsford, England, for use in X-ray astronomy. Measurements of Charge Transfer Inefficiency (CTI), dark current and other parameters relevant to the detection of low signals were made. Many of the methods were developed on a project known as Work Order 1 of this contract, which is abbreviated hereafter to "WO1" and referenced as the "WO1 Report" (Holmes-Siedle 1991); this was conducted by the same principal investigator at BNF-Fulmer Research, Leicester University and SRON, Utrecht, before the contract was transferred to Brunel's Centre for Radiation Damage Studies (hereafter referred to as "Brunel". An objective of the new series of tests by Brunel and Leicester is the improved characterization of the performance of CCDs in conditions equivalent to the core period of the XMM mission. The orbit for this mission is shown in Fig. 1.1. It intersects the Van Allen Belts but the major hazard is solar flare proton damage during its long dwell time outside the magnetosphere.

Reports by Brunel and Leicester issued earlier in this contract include the CCD Test Plan Report (Holmes-Siedle, Holland and Watts, 1994), which presented detailed proposals for the tests such as the numbers of samples, the measurements of CTI, dark current and other parameters relevant to low-signal (X-ray photon) detection, methods of proton beam exposure, dosimetry, anneal periods and other experimental parameters; and the Data Analysis Report (Holmes-Siedle, Watts and Holland, 1995a) which described a joint data analysis effort of Brunel and Leicester Universities, in preparation for the measurements to be made. The technical issues concerning CCD design in relation to radiation in space have been discussed widely (see e.g. Holmes-Siedle et al 1991; Holland et al 1991; Dale et al 1994; Janesick et al 1991),

We have made much use of recent developments in the understanding of silicon device damage including:

(a) an improvement in the understanding of the defect picture in the silicon as it exists in the active region of CCDs (implanted, epitaxial silicon), including the development of defects under irradiation and during annealing and the precise origins of dark current in damaged CCDs (see e.g. Watts et al 1995).

(b) models showing the importance of photon hit rate and X ray energy in determining the charge transfer inefficiencies, CTI and dark-current damage constants etc.

(c) new theoretical models describing the effects on CTI of clock rate in serial and parallel registers and the sizes of microvolumes occupied by stored signal charge as a function of electrode and channel design

In the present report, we give a concise account of WO1 and a detailed description and analysis of the experimental work done in WO2, which included three types of CCD. The work included a two-part irradiation by protons, with supplementary experiments including annealing of the samples at elevated temperatures. The continued study of the CCD samples with respect to monitoring of long-term annealing or further testing will be discussed with ESTEC.

Fig 1.1

Apogee
70,000km
approx

Scientific
Orbit

High Equatorial
Orbit (GEO)

Earth radii

Geostationary Orbit

Polar
Orbit

Low
Equatorial
Orbit

Inner Belt-
Trapped
Protons

Outer Belt-Trapped
Electrons and Protons

1 Earth Radius
= 6371km
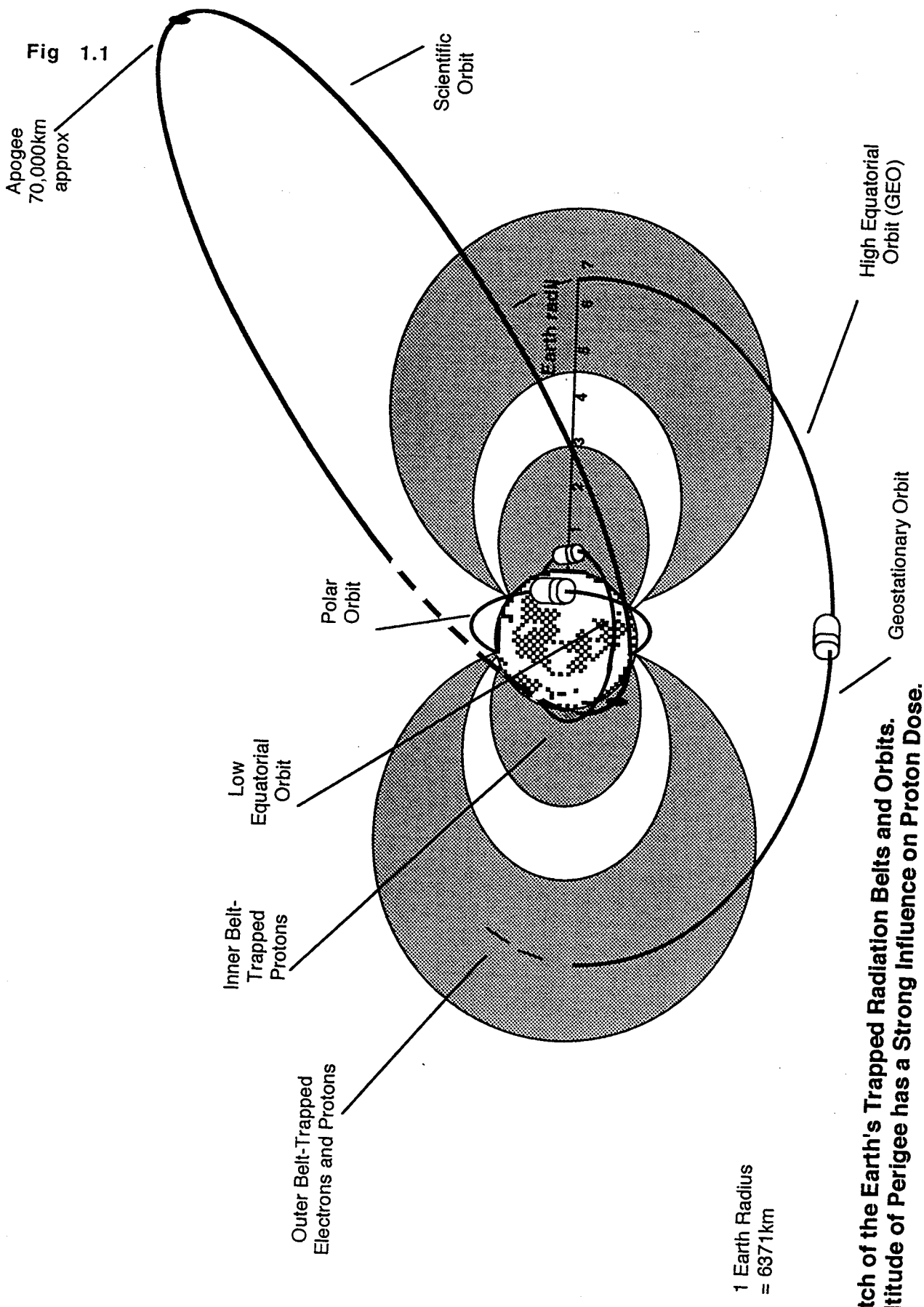
Fig. 1.1   A Sketch of the Earth's Trapped Radiation Belts and Orbits.
The Altitude of Perigee has a Strong Influence on Proton Dose.

1.2. Technical background of project

After the findings of Work Order 1 and other ESTEC funded work, it was decided that two objectives would be emphasized, as follows:

(a) BETTER STATISTICS ON CCD DAMAGE

Better statistics than heretofore can be obtained from the study of a statistically significant number of CCD chips from an single wafer. The aim is to improve our knowledge of the statistical spread of proton-induced change in X-ray CTI and dark current, especially at cryogenic temperatures. The main interest is the effect of proton irradiation on X-ray astronomy measurements in operational conditions similar to those in the XMM X-ray astronomical cameras, as described in Table 1.1. To understand and predict these effects, a precise knowledge is needed of the type and energy level of radiation-induced defects (various combinations of vacancies, interstitial silicon atoms and impurities) created by radiation in the active regions, especially the buried channel. While the well-known techniques of deep level transient spectroscopy (DLTS) cannot be applied directly to the EEV CCD structure, it is possible to apply the same principles by studying the dependence of certain electrical parameters of the CCD on measurement temperature, clock rate and photon hit-rate, as explained herein. For economic reasons, a chip produced in large numbers, the CCD02, was chosen as the test vehicle for this study.

(b) EVALUATION OF XMM DEVICE TECHNOLOGY

The object of this technology evaluation was to characterize the CCD12 and the CCD15 chips. CCD12 will be used in the EPIC camera and CCD15 will be used in the XMM RGS astronomical spectrometer. The nominal CTE degradation model was developed in WO 1 (Holmes-Siedle 1991; Holland et al 1991). This model includes the influence on CCD degradation of important factors such as clock rate and temperature. The main aim of the present work is to improve knowledge of these factors and of processing dependence; this will advance procedures for quality control of CCDs for XMM. The approach includes the refinement of constants required for degradation equations. Several of these constants are known roughly. Tests in part (a) will improve accuracy but, in part (b) we are exploring whether, in the degradation characteristics of new designs, there may be any gross effects of the new processing.

The measurement system was based on that developed at Leicester University Space Centre (hereafter referred to as "Leicester") by Holland and co-workers for the XMM EPIC camera project. Additional measurements were made based on the CCD parametric tests developed by Watts and co-workers at Brunel (see Robbins 1992, Roy 1994). Further background can be obtained from recent reports and papers by Brunel, SIRA, SRON and JPL, quoted in our references; and extensive treatments of damage effects given in recent books and ESA standards. The books include Ma and Dressendorfer (1991) on surface damage, Messenger and Ash (1989) on bulk damage and Holmes-Siedle and Adams (1993) on the space environment and the CCD as a device and the standards include ESA 1991 and other standards given therein.

TABLE 1.1 : CCD TEST CONDITIONS RELATED TO PROJECT REQUIREMENTS

Operation	Leicester Test	Typical XMM Satellite Values EPIC	RGS
SPARSENESS OF DATA			
a: X-RAY SPOT IMAGE	n/a	1 hit/1200s/mm² upto 100/s/mm²	3000hits/slit
b: UNIFORM X-RAY ILLUMINATION	10/s/cm²	2-4hits/s/cm² (cosmic ray background)	30hits/slit image
CLOCK CONDITION			
mission	Note 1	Note 2	Note 3
scientific tests	Rate dependence study leading to a standard setting		
SIGNAL SIZE			
min. electrons	400 electrons	~100 electrons	~100
max.	2000 electrons		
TEMPERATURE (°C)			
Range	-70/-90/-110/-130	-90 to -130	-60 to-120
ANNEALS			
operational at130 °C	+130 °C/48h	TBD	Start
scientific	5 devices isochronal	-	-

Note 1: Image integration time, 2-60s. Sampling time, 3 -10μs. Readout clock period, 7-50μs. Readout clock (RΦ) bin period, 5μs. Image clock (IΦ/SΦ) period, 10 μs. CCD12 device has 520 x 800 pixels and is operated in frame transfer mode. CCD15 device has 380 x 280 pixels and is operated in Full Frame mode with 3 by 3 binning.

Note 2: Image integration time 2.4s. Sampling time, 3μs. Readout clock period, 6μs. RΦ bin period, 2μs. IΦ/SΦ period 10 μs. Read 602 rows by 610 columns.

Note 3: RΦ bin period, 1.8 μs. Readout rate is 19.6 μs between each bin. IΦ/SΦ binned at 18 μs/pixel. Device is read out with 3 by 3 binning.

2. Summary of Work Order 1, Harwell 1991

2.1 General

A short account of Work Order 1 (WO1) measurements is given here as a background to the approaches adopted in WO2. In WO1, performed by BNF-Fulmer, Leicester and SRON, Utecht, eleven cooled CCD02 devices were exposed to protons of 10 MeV, four at 2 MeV, three at 1.5 MeV and one at 0.7 MeV. Extensive data were recorded at cryogenic temperatures on site. Table 2.1 gives the doses used at 10 MeV.

TABLE 2.1 : FLUENCES AND DOSES OF PROTONS USED IN AUGUST 1990
10-MeV VAN DE GRAAFF ACCELERATOR TEST

FLUENCE OF PROTONS ($p.cm^{-2}$)	IONIZING DOSE ($rad[Si]$)
1.8E8	100
3.6E8	200
9.0E8	500
1.8E9	1000
3.6E9	2000
9.0E9	5000

Conversion factor for 10 MeV protons: 1 rad (Si)= 1 cGy (Si) = 1.8E6 p cm^{-2}.

The results confirmed hopes for accurate mission prediction, and showed that lowering the operating temperature gave a strong improvement in performance under radiation. The narrow-channel technology exhibited improved radiation tolerance, giving encouragement for radiation hardening by solid state techniques.

The experience gained led to new features in the plan for WO2. Devices were irradiated at room temperature; shields were arranged to give several fluence values on one chip, including always an area receiving no fluence. This allowed faster throughput, better comparative measurements of damage as a function of fluence and the ability to subject a given chip to further irradiation if necessary.

2.2 Dosimetry

The measurement of particle fluxes in accelerator beams is physically difficult (see e.g. Holmes-Siedle and Adams 1993) and care is required to obtain accurate fluences at the surface of the chip and to estimate the deposition of energy as the particles or photons pass through the media making up the CCD. For protons, the primary measurement is beam current, measured with a Faraday Cup, which is simply a metal beam stop of well-defined acceptance area, with provisions to reduce the possibility of loss of charges by secondary emission or other conduction mechanisms. In WO1, such a cup was used on the Harwell and Utrecht accelerators but, in WO2, the accuracy of cup measurements was reduced by the physical geometry of the cyclotron and high levels of RF noise. In WO2, the "master" measurement was counts recorded in a nuclear diode particle counting system (see Section 3), with the diode placed off-axis and close to the CCD. The counts could then be converted to particle fluence on the beam axis.

Radiation-Sensitive Field Effect Transistors (RADFETs) contain special oxide insulators of calibrated response to ionizing radiation (Holmes-Siedle 1974, 1986). They can be called a "solid-state ionization chamber with a built-in memory". The sensors are not absolute dosimeters but are useful for the correlation of beam dose delivery from shot to shot and machine to machine, using calibrations based on accurate CO-60 gamma-ray exposures. RADFETs were used to monitor most CCD exposures in the Harwell proton beam; it proved difficult to do the same in the smaller Utrecht and Birmingham beams. The RADFET response

was lower than expected for a given proton dose in rads (Si). The lower response to a given dose is caused by the higher track density in the case of low energy protons versus Compton electrons generated by gamma rays, which leads to higher electron-hole recombination rates and hence lower charge build-up per unit dose.

Transient radioactivity was observed in the frames stored shortly (say 1 minute) after 10 MeV proton irradiation of CCD02s. This interferred with CTI measurement but faded quickly. The readings gave a useful supplemetary check that the proton beam was uniform.

2.3 Charge Transfer Inefficiency (CTI)

The spectroscopic performance of the CCD is affected by proton damage in the channel region, as shown in the W01 report. As damage increased, the K peaks first broadened, then merged and, at the higher damage values, became so broad as to be meaningless, virtually disappearing on the scale used. Charge Transfer Inefficiency (CTI) is the appropriate parameter for measuring the above effects and this was extracted from stacked line traces (SLT) collected during and after the experiment. Fig 2.1 summarizes the general model of CTI degradation emerging from the tests (Holmes-Siedle 1991).

The stepwise irradiations, with proton fluences increasing logarithmically, led to a smooth increase in CTI. The increase in CTI was linear with dose once the change was fairly large. Fig 2.2 gives a typical plot for front - illuminated CCDs. Degradation was visible after 1E8 10 MeV protons cm-2. A straight line with a slope of 2.0E-13 cm^{-2} can be fitted to the curve for the CCD02 device. This slope is the proton damage constant for the parallel CTI, which is crucial quantity in methods of CCD radiation testing and quality control. The degradation of serial CTI is considerably less than the parallel. The reasons are now understood and are discussed later. The narrow buried channels showed a definite improvement over the normal channels in the parallel registers, as expected. The supplementary buried channels did not show this same improvement.

CTI measurements after irradiation were made with Al and Ti photons from an X-ray tube - 1.5 and 4.5 keV respectively. These measurements gave a useful comparison of CCD performance at widely separated points on the X - ray spectrum. In general, degradation was worse for Al than for Ti by a factor near two. Temperature dependence curves gave important design guidance and scientific information. Fig. 2.3 a and b show CTI as a function of operating temperature. The striking features of all of the curves was the much stronger change with temperature after irradiation. The explanation of the good low-temperature operation is that trapped electrons are immobilized in the radiation -induced defects, so that, once filled, the traps cannot degrade new image information. The slope of the curve is determined by the relation of trap release time constant and the clock timing.

In W01, several cryogenic anneals were carried out on the beam line. **Isochronal**: a high-resistivity device was rapidly warmed but in controlled stages. After each stage, it was re-cooled and a CTE measurement taken before proceeding to the next higher stage. The CTE changes observed in this cryogenic isochronal anneal were not large. **Isothermal**: a device was measured several times at -90°C after 10 MeV bombardment. There was little detectable change over an hour, suggesting that defects are either still "frozen" or have evolved to a stable condition before the first measurement. High-temperaure anneals were carried out later in the laboratory. Annealing of many of the defect complexes in silicon is known to take place between about 100 and 400°C. **Long-term isochronal**: at temperatures of 112 or 127°C, a parallel CTI reduction by a factor of 3 is possible by heating for a hundred hours. Both low and high - resistivity samples annealed by about the same amount. It should be noted that this is based just one and two low resistivity and high resistivity devices respectively. This is not full recovery, but if a factor of 3 could be achieved by long - term, low-temperature treatment, then attempting to recover serious damage by heating during flight would be a worthwhile measure.
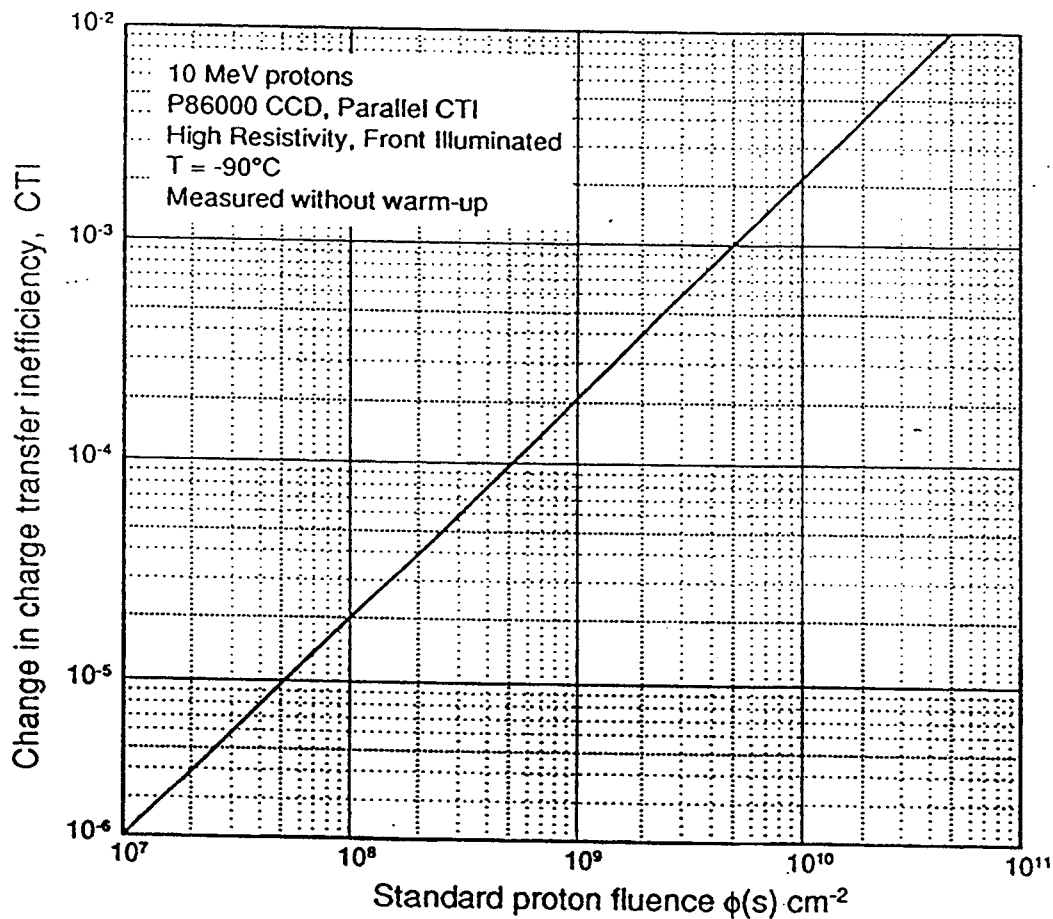
Parallel CTI Response Prediction Model :
CTI at -90°C vs. Standard 10 MeV Proton Damage Units.
High - Resistivity P86000.
Slope $\dfrac{CTI}{\phi(s)}$ = 2×10^{-13} cm² (E(s) = 10 MeV)

Fig 2.1 Prediction model for 10 MeV proton damage to the CTI of EEV high resistivity CCD02 devices at -90 Centigrade. Slope is 2.0E-13 cm-2. From Work Order 1.
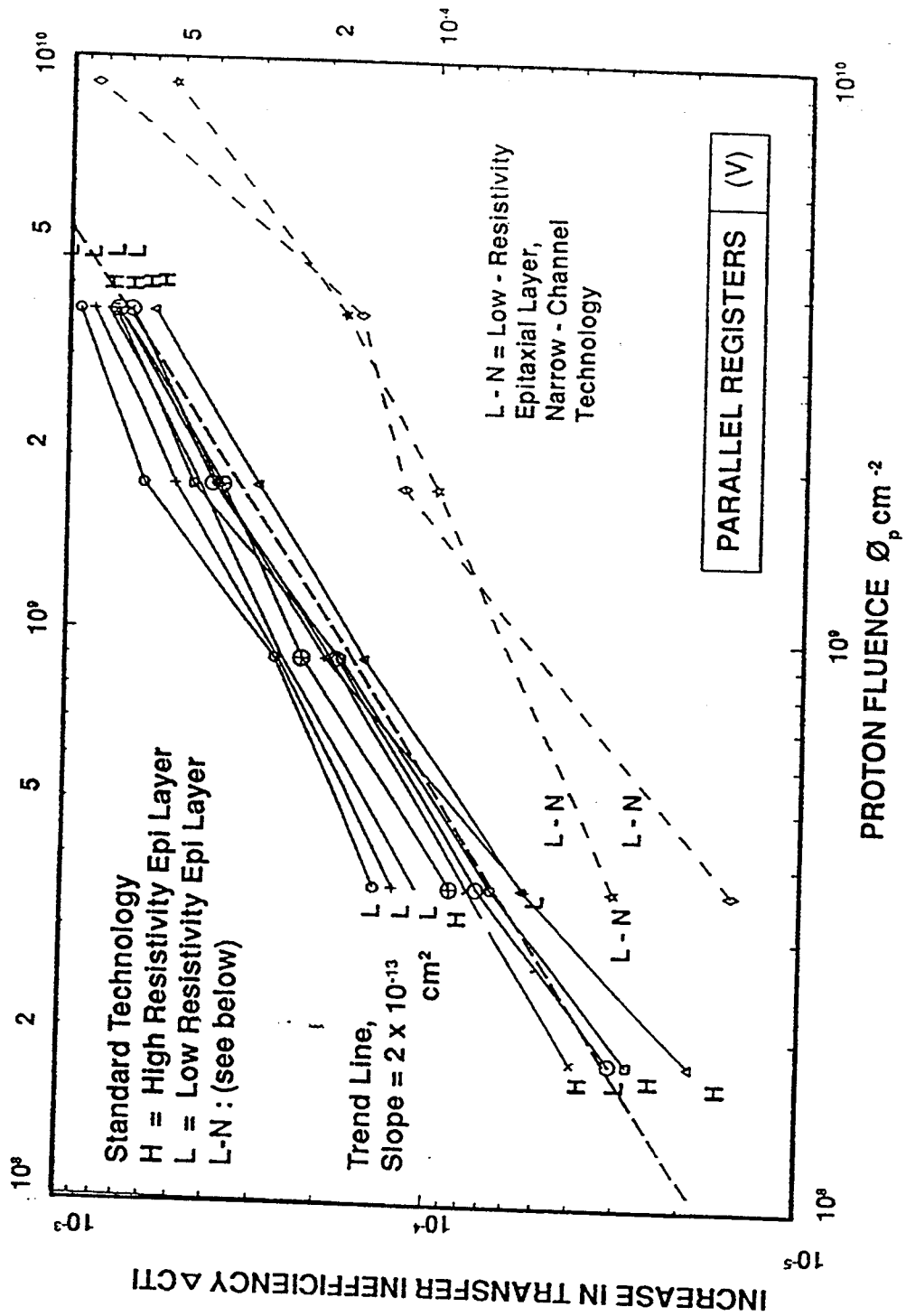
Fig 2.2 A collection of curves from WO1. Parallel charge transfer inefficiency (CTIP) of EEV CCD02 devices (purchased 1990) versus 10 MeV proton fluence, measured at -90 Centigrade. Dotted lines denote special channel implant technology.
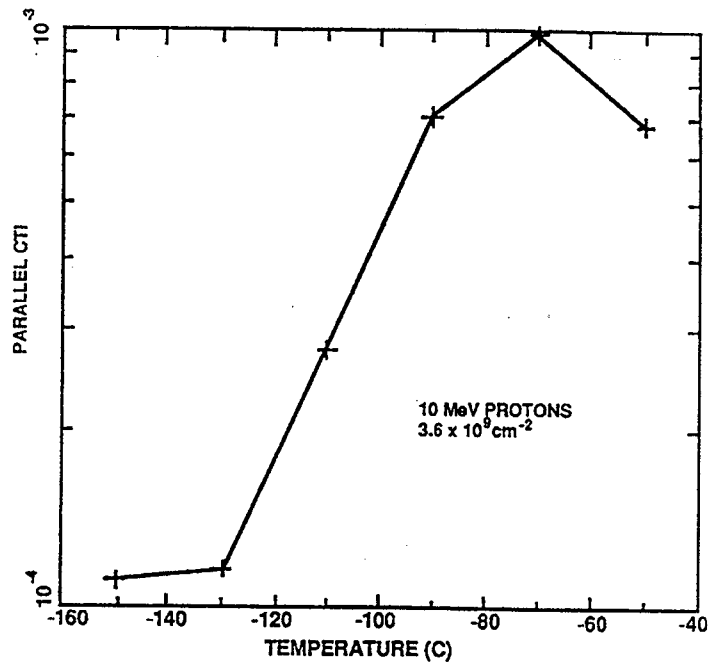
(a)

Variation of "Damage" with Temperature of Operation. EEV P86000 CCD Damaged
with 10 MeV Protons at -90°C. Parallel CTI vs. Measurement Temperature from -50 to -150°C.
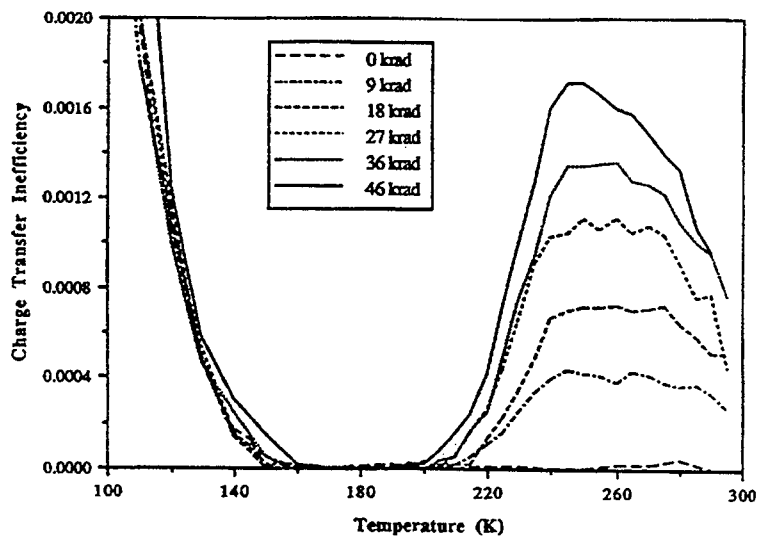
(b)

The CTI versus temperature for a signal size of 1000 electrons and a t_0 of 5 ms.

Fig. 2.3 Temperature dependence of CTI in radiation
damaged CCDs (a) EEV CCD02 devices, WO1 and
(b) Robbins 1992, Sr90 beta rays.

2.4 Dark Current

Immediately after irradiation with protons, the CCD image was affected by a dark current increase. This, however, decayed after about 15 minutes back to a barely detectable level and may be connected with the short-lived radioactivity reported above. A detectable level of dark current was not expected at -90°C. The transient effect described above is thus considered to be an artefact of the rapid proton exposure. It would not be of great importance in the much lower dose rates expected in space.

Dark current spectra were not measured at the test site. Histograms of the type shown in Fig. 2.4 were made in the laboratory several days later. The figure shows the frequency of occurrence of a given bin of current per pixel values, expressed in ADC bin number, convertible to e/pixel/sec. Table 2.2 provides some CTI and dark current results from WO1. The table shows the increases for three high-resistivity front-illuminated samples.

In summary, at cryogenic temperatures, dark current is only mildly increased after the full exposure, typically by a factor of 2.5 at all temperatures measured.

It was possible to draw some conclusions on the source of the dark current. In the cases shown in the table, CTI had increased to approximately the same severe damage level in all samples, well over ten times the original value. That is proton bulk damage values for the buried channel region were about the same (the 1.5 MeV protons are 7.5 times as effective as 10 MeV). If the dark current were caused by bulk damage in the channel, then the factors of increase might also be expected to be about the same. Instead, the factors varied quite widely, and it is noticeable that the factors for the 1.5 MeV case are the lowest (barely detectable increase of dark current by a factor of 1.04 at -70 °C). This is the trend expected if dark current increases were controlled by ionizing energy deposition (lower for the 1.5 MeV test) in the silicon - silicon dioxide interface, which is known to be more sensitive to processing variation than the buried channel or the bulk silicon. It is important to note that the devices were NOT operated in inversion mode and as a result the dark current is dominated by the surface component. This is also true for the devices tested in WO2.

In dark - current histograms (cf. Fig 2.4), the statistical distribution of the dark - current for irradiated pixels exhibited a Gaussian peak - as before irradiation. However, added to it was a "tail", representing major radiation - induced current in a few pixels. These dark current "spikes" are well known. One explanation is that proton - induced defects can be affected strongly by position in the pixel volume. Where the local field is strong, the release rate of electrons from traps is greatly increased. Brunel workers are considering a model in which the spikes are caused not by P-V centres but by a different defect. It has become clear that dark current measurements contain information about bulk silicon defect concentrations and could possibly act as a convenient control measurement during lot acceptance testing as well as a measure of damage levels in orbit.

In the later stages of WO2, it had become apparent that (a) dark -current spikes annealed at a temperature lower than the CTE defects; (b) Random Telegraph Signals (RTS) anneal below 100 °C and (c) in p-i-n diodes, annealing of dark current occurs at room temperature. These observations suggest that certain defects in silicon are labile at room temperature and therefore some changes in CCDs, particularly of dark-current spikes and other hot spots, may occur during warmup from -90 °C to room temperature, despite the cryogenic annealing tests cited above.

In WO1 we concluded that, in the XMM flight condition, dark current will not present a problem. However, the same devices, if used at or near room temperature, would experience severe problems (see Holmes-Siedle et al 1991a ; Hopkinson 1992 1995). Dark current measurements are however being developed as a tool for use in all CCD damage studies.

Table   2.2

Proton-Induced Increases in CTI and Dark Current (e/pixel/s) for Three Typical High-Resistivity Charge - Coupled Devices, Type CCD02 (Holmes-Siedle 1991). WO1 data.

- -

Type	Temp. (deg C)	Unirr- adiated	Irrad- iated	Factor Increase

- -

HRF1: Exposed 1.5 MeV Protons
Fluence 5.1E8 cm^{-2} (1106 rad(Si))

Type	Temp. (deg C)	Unirr-adiated	Irrad-iated	Factor Increase
CTI	-90	8.0E-6	8.5E-4	110x
I(D)	-30	216	394	1.8x
	-50	12.5	23.6	1.9x
	-70	0.49	0.51	<1.1x

HRF2: Exposed 10 MeV Protons
Fluence 3.6E9 cm^{-2} (2000 rad(Si))

Type	Temp. (deg C)	Unirr-adiated	Irrad-iated	Factor Increase
CTI	-90	1.1E-5	2.5E-4	22x
I(D)	-30	156	435	2.7x
	-50	9.8	36.7	3.8x
	-70	0.33	0.64	1.9x

HRF6: Exposed 10 MeV Protons
Fluence 3.6E9 cm^{-2} (2000 rad(Si))

Type	Temp. (deg C)	Unirr-adiated	Irrad-iated	Factor Increase
CTI	-90	7.0E-6	6.0E-4	86x
I(D)	-30	227	432	1.9x
	-50	8.7	18.8	2.1x
	-70	0.18	0.30	1.6x
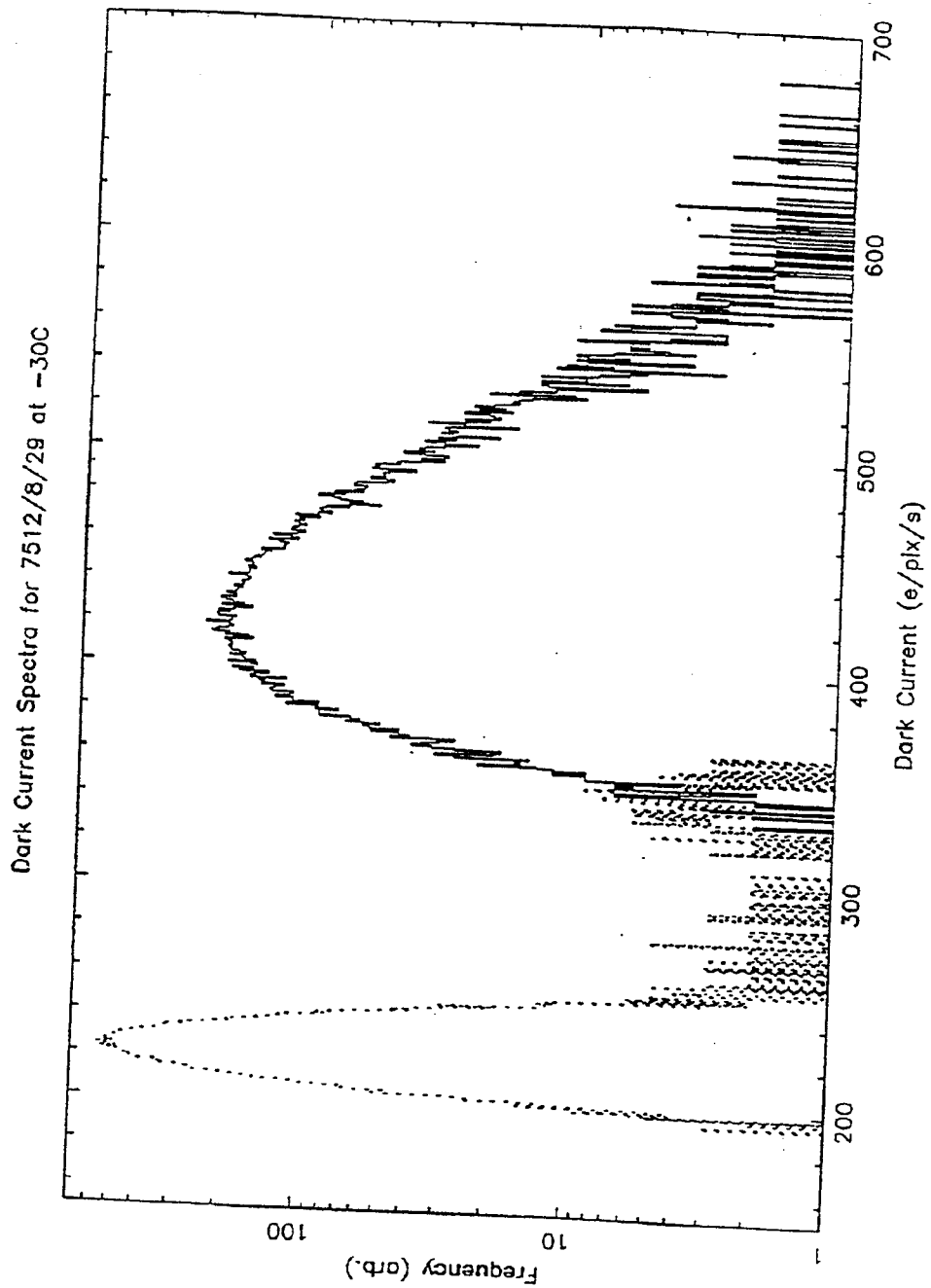
Fig. 2.4 Typical dark current spectra for an EEV High Resistivity CCD02 irradiated by 3E9 10 MeV protons per square cm. Measured at -30 Centigrade. From Work Order 1. The figure also shows the spectrum before irradiation.

2.5 Noise and Amplification

The output noise generated at -90 °C did not rise above the electronic readout system noise, which was itself very low. The noise, measured in all cases before and after irradiation, was about 8 electrons, to an accuracy of 0.2 electrons. A careful re-examination of one apparent noise increase (device R369) showed it to be spurious: the extra signal came not from output noise but an increased "tail" in the partial-event spectrum .

Below a fluence of 2 E9 p cm^{-2}, changes in the gain of the output amplifier remained in the region of 1 per cent. Increases became significant at 2E9 cm^{-2}, especially in the case of a narrow buried channel device. In back-illuminated devices, the output node was protected by the packaging and so normally experienced no degradation.

2.6 Flat-Band Voltage

No direct measurements were made of this parameter in the Leicester measurements, the electrical settings for the clocks and reset device did not require alteration for top-quality performance. This lack of sensitivity to oxide field effects was found whether the device was irradiated in a powered or unpowered condition. It was concluded that the values of flatband voltage shift were probably less than 2.5 volts and more likely to be between 1 and 2 volts. The maximum 10 MeV proton dose values were only about 5000 cGy (5 krads). Measurements with X-rays and isotope radiation tests (Jansen et al 1995: Robbins et al 1993) led to estimates of responsibility in EEV's standard CCD dielectrics lying between 100 and 550 mV/krad (μV/cGy), depending on the precise fields across the dielectric during irradiation. We would thus predict shifts between 0.5 and 2.5 volts of the maximum proton fluences used (i.e. 5000 cGy (5 krad)). There appeared to be little difference in CTI between CCDs which were powered up during irradiation and others which were powered down.

3. Work Order 2 - Plan and Irradiation Setup

3.1 Plans for Work Order 2

The irradiations in this work were designed to fit the aims stated earlier - better statistics and evaluation of the products of new masks and improved technology for X-ray sensitivity. Coupled with this aim were improvements of analytical methods and operational techniques. Reports on the irradiation test plan (Holmes-Siedle et al 1995a) and an improved analysis of Work Order 1 (Holmes-Siedle et al. 1995b) describe the preliminary work. The irradiation setup is described below. After the irradiations, Leicester issued a Proton Test and Calibration Report, which is included in this section.

This section details, results of beam calibration, and device CTI post-irradiation characterisation tests that were conducted under ESTEC contract number 8815/90/NL. Calibration and beam monitoring at the Birmingham Cyclotron was performed by Leicester University using a photodiode intercepting the proton beam off-axis. Details are given of the measurement technique and the results obtained for each of the detectors irradiated. An analysis of errors is made providing an overall estimate of proton flux to within 10%.

The irradiation plan, with details of CCD sample, fluence and measurements is summarized in Table 3.1. Due to problems with the Fluorine (F at 700 eV) x-ray source, measurements were made using the Cu-L line (900 eV). The output amplifiers received zero fluence (i.e. were shielded) except in the special cases noted.

Table 3.1

Proton Irradiation Test Plan
(A. Holland, Leicester, 1994)

Table 3.1 Test plan matrix

Test Device	Device No.	Silicon	Fluence (cm^{-2}, 10MeV)			Anneal	X-Ray Tests	
			Left	Mid	Right			
CCD02-1	A0962-15	20μm Epi	1E9	N/A	Contrl	Yes	Tests 1,2	Note 2
CCD02-2	A0962-16	20μm Epi	1E9	N/A	Contrl	Yes	Tests 1,2	Note 2
CCD02-3	A0962-19	20μm Epi	1E9	N/A	Contrl	Yes	Tests 1,2	Note 2
CCD02-4	A0962-20	20μm Epi	1E9	N/A	Contrl		Tests 1,2	
CCD02-5	A0962-21	20μm Epi	1E9	N/A	Contrl		Tests 1,2	
CCD02-6	A0962-24	20μm Epi	1E9	N/A	Contrl		Tests 1,2	
CCD02-7	A0962-26	20μm Epi	1E9	N/A	Contrl		Tests 1,2	
CCD02-8	A0962-31*	20μm Epi	1E9	N/A	Contrl		Tests 1,2	
CCD02-9	A0962-33*	20μm Epi	1E9	N/A	Contrl		Tests 1,2	
CCD02-10	A0962-49	20μm Epi	Control					
CCD15-1	A2027/3/6	50μm Epi	1E8	5E7	Contrl	Yes	Tests 1,2	Note 2
CCD15-2	A2028/15/1	50μm Epi	2E8	1E8	Contrl		Tests 1,2	
CCD15-3	A2028/15/6	50μm Epi	5E8	2E8	Contrl		Tests 1,2	Note 2
CCD12-1 OE	A3197/5/4	100μm E	1E8	5E7	Contrl		Tests 1,2	Note 2
CCD12-2 OE	A3197/5/5	100μm E	1E8	5E7	Contrl		Tests 1,2	
CCD12-3 OE	A3197/5/9	100μm E	2E8	1E8	Contrl		Tests 1,3,4	Notes 1,2
CCD12-4 OE	A3197/5/10	100μm E	2E8	1E8	Contrl		Tests 1,2	
CCD12-5 OE	A3196/6/7	100μm E	5E8	2E8	Contrl	Yes	Tests 1,3,4	Notes 1,2
CCD12-6 OE	A3196/6/8*	100μm E	5E8	2E8	Contrl		Tests 1,2	
CCD12-7 OE	A3188/17/7	Bulk	1E8	5E7	Contrl	Tested outside this contract		
CCD12-10a	JET-X	65μm Epi	5E7	N/A	Contrl	Tested outside this contract		
CCD12-10b	JET-X	65μm Ep	2E8	N/A	Contrl			
CCD12-10c	JET-X	65μm Ep	5E8	N/A	Contrl			

Tests performed on devices

Test No.	Name	Condition
Test 1	Dark current spectra	Temp=-30,-50,-70°C, Image integration=30s
Test 2	X-Ray CTI	Temp=-70,-90,-110,-130°C, Fe X-rays, Flux ~10cm^{-2}s^{-1}
Test 3	CTI vs. X-ray Energy	Temp=-70,-90,-110,-130°C, Fe, Ti, Al, F X-rays, Flux ~10cm^{-2}s^{-1}
Test 4	CTI vs. X-ray Flux	Temp=-70,-90,-110,-130°C, Fe X-rays, Flux ~1-1000cm^{-2}s^{-1}
Note 1	*CTI Correction*	*X-ray data to be used for CTI correction investigation*
Note 2	*Post anneal CTI*	*Post-anneal test flux rates same as for Test 2*

* indicates shielded output amplifier

3.2 Proton Dosimetry

3.2.1 Beam Monitoring and Reference Detector

The beam was broadened using an aluminium scattering foil of thickness 1 mm and by using the focussing magnets in a "de-focussing mode". This produces a beam at the CCD of typically 2-5 cm diameter. To irradiate the whole of a large area CCD uniformly, the beam was then swept in the vertical and horizontal directions giving an effective beam of >6 cm diameter. During the second series of exposures it was found that the beam sweeping was not necessary and a uniform beam was obtained with the scattering foil and de-focussing magnets alone. Beam monitoring was effected using a deep depletion photodiode which, due to the breadth of the beam, could be mounted in close proximity to the CCD undergoing irradiation. The details are depicted in Figure 3.1 below.

The CCD was located centrally on the beam axis and portions of the device were shielded from irradiations using formed copper plates. These shields were manufactured for each device and exposure (i.e. 1/2, 1/3 and 2/3 for CCD02, and CCD12 and CCD15s) to enable the irradiated zones to be approximately the same from device to device within one CCD type. The photodiode was mounted on a support arm which enabled the diode to be moved in a locus which intersected the beam centre. The photodiode was supported from the cryostat front plate and could be moved in a locus passing through the beam axis. Rotation of the cryostat plate with respect to the beampipe enabled the beam to be profiled in two dimensions.

TABLE 3.2 Details on the UDT PIN-3CD photodiode used for beam monitoring

Parameter	Value	Units
Active Area	3.2	mm^2
Capacitance	10	pF @ 10V/1 kHz
Leakage Current	2	nA
Rise Time	15	ns (50 Ω load)

The photodiode used was a UDT sensors diode, part no. PIN-3CD. The device details are given in Table 3. 2. The active area of the diode was given by the manufacturer for optical photons as being 0.05x0.1 inches, corresponding to total quoted active area of 3.2 mm^2. During the proton tests, the active thickness of the diode was determined to be 27 μm from the total charge liberated in the photopeak from ionisation. It can be inferred that the active region did not extend appreciably beyond the defined window area of 3.2 mm^2.

3.2.2 Interpretation of Proton Spectra

The monitoring photodiode was used in photon counting mode and spectra were accumulated on an Oxford Instruments PC-based PCA system. Figure 3.2 gives a typical spectrum recorded from the diode during an exposure. The main ionisation peak is seen to be clearly separated from the noise thereby enabling accurate determination of the number of protons passing through the active region. In addition, pileup events or double proton hits which occur during the same shaping time period are also observed. The relative intensity of this second, higher, peak depended upon the proton rate. The number of events in this second peak was also counted and two times the number was included in the estimation of proton fluence. In general, the proportion of pileup events was kept to below 5% of the total number. Both of the peaks sit on a background continuum which was believed to arise from secondary electrons produced in the beam and which did not represent an additional component to the displacement damage in the detector.
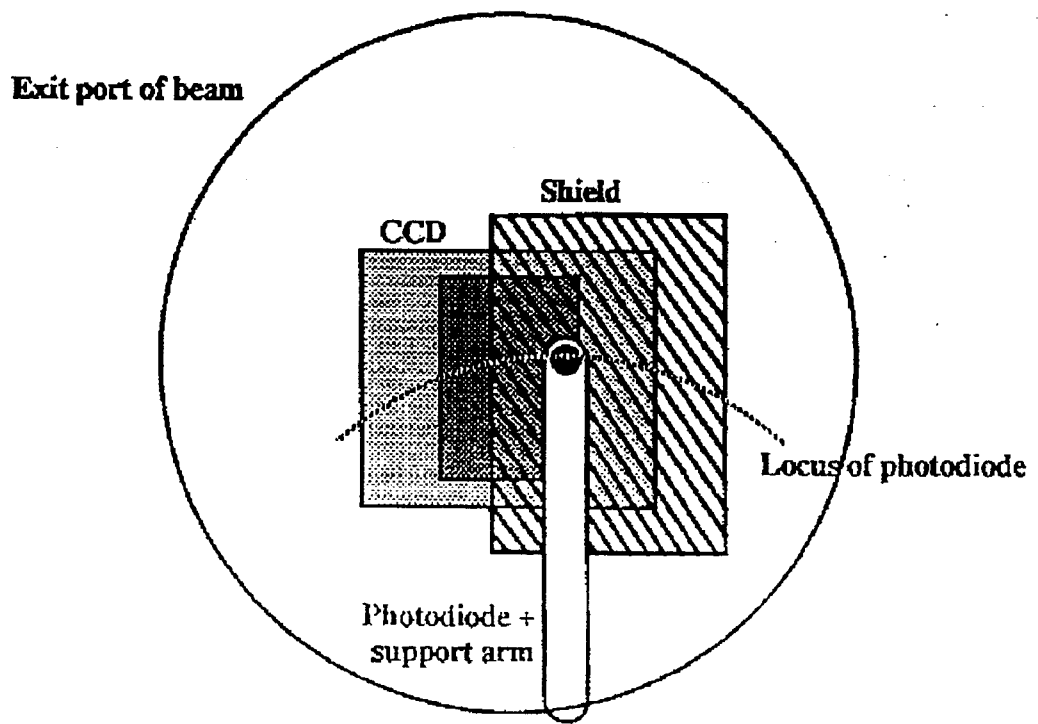
Fig. 3.1 Schematic of CCD irradiation geometry and photodiode monitor, looking along the beam axis
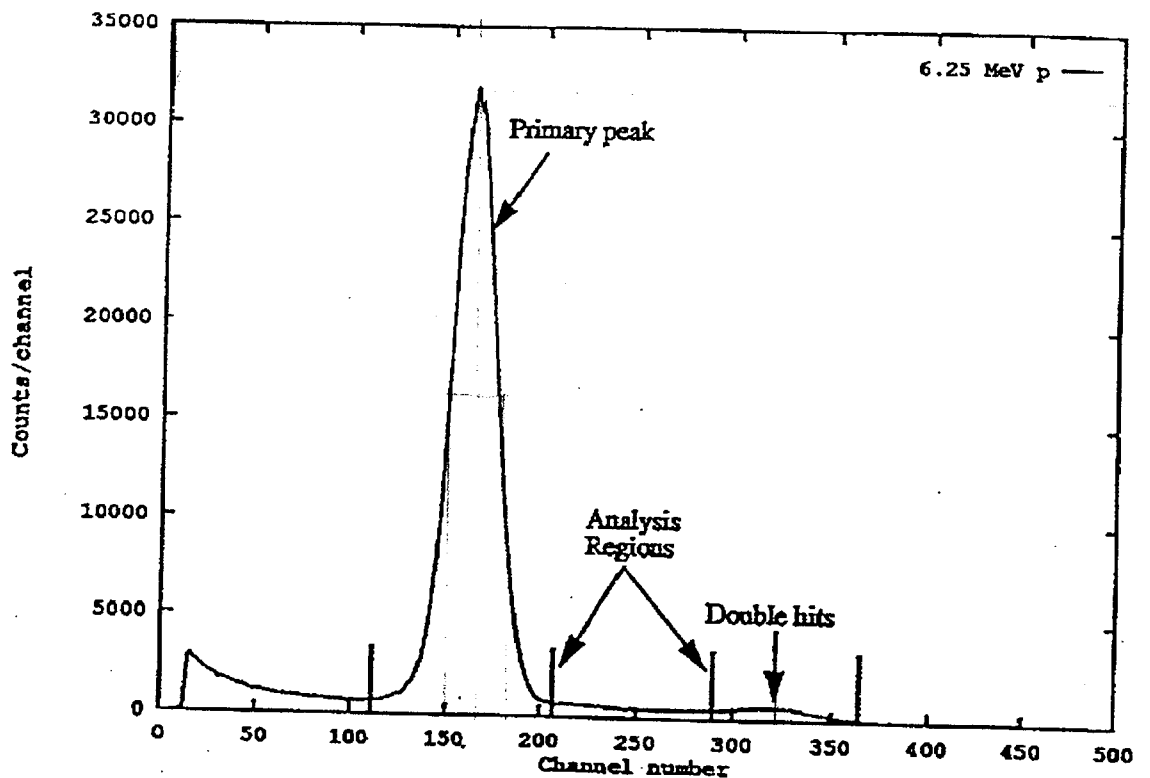
Fig. 3.2. Pulse height spectrum given by the photodiode in the 6.25 MeV proton beam

October 1994

December 1994

+/- 5%

+/- 5%

Intensity (arb.)

Intensity (arb.)
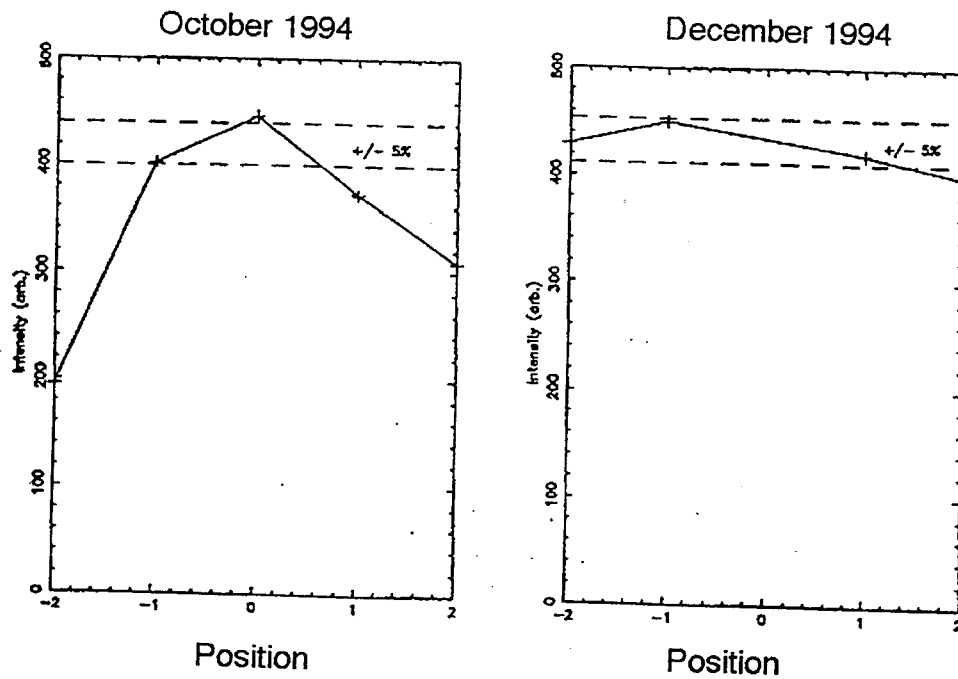
Position

Position

Fig. 3.3 Beam profiles for the two proton irradiation campaigns. Photodiode count vs. position

To evaluate the total fluence at the CCD after an exposure, the spectrum was evaluated for primary and double hits by placing cursors as indicated around the two ionisation peaks. The net number of events in "the peak, after background continuum subtraction, was used. In addition, the dead time of the system was logged by recording the elapsed time, $T_{elapsed}$, and the system live time, T_{live}. These data were used to correct the measured number of events to that actually delivered. Finally , corrections were made for the ratio between beam intensities on the axis and at the diode position, C_{oa} and the Area A. The overall calculation is given below;

$$Fluence(10MeVequiv.) = \frac{(N_{primary} + 2 \times N_{Double})}{A_{Diode}} \times \frac{T_{elapsed}}{T_{live}} \times Coa \times \frac{NIEL(10MeV)}{NIEL(6.25MeV)}$$

where C_{oa} = correction for fluence due to the fact that the diode is off-axis.

The fluence is normalised to 10 MeV equivalent protons using the NIEL damage relationship, where the 6.25MeV protons are a factor 1.61 times more damaging than 10 MeV protons.

3.2.3 Beam Profile

The irradiations were conducted in two sessions, with a break for beamline repair between sessions. For each campaign the beam profile was evaluated to provide an estimate of uniformity over the irradiated device, and to enable generation of a correction factor to be applied to the results of the monitor photodiode due to it being located off the beam axis.

Figure 3.3 gives the profiles of the proton beam measured for the two irradiation campaigns at the Birmingham cyclotron. Lines are also given indicating the limits where the beam uniformity exceeds +/- 5%. For reference, the dimensions of the active areas of the CCDs are given in the table below.

TABLE 3.3. Dimensions of the CCDs used for irradiation

CCD Type	Serial Dimension (mm)	Parallel Dimension (mm)	Campaign
CCD02	8.5	12.6	1
CCD12	20.7	27.6	1
CCD15	27.6	20.7	2

Since the irradiations were conducted over two sessions at the cyclotron, knowledge gained in the first campaign were applied to the later tests. In particular, the beam uniformity was improved. As can be seen in Figure 3.3, for the first series of irradiations, the +/- 5% sweet spot extended over 17mm, thus the uniformity was fairly uniform over the image area for the CCD02 devices. However, non-uniformity was slightly greater than +/- 5% for the extremities of the CCD12 in the parallel (vertical) direction. In the second series of irradiations the beam uniformity was much improved, leading to a beam uniformity of better than +/- 5% over the device surface.

3.2.4 Systematic Errors in the Measurement

The systematic errors in beam exposure calibration may be broken down into the following:-

1)   An error of 200 keV was estimated for the proton energy. Using the NIEL relationship, this produces a corresponding error of 2.5% on the dosimetry.

2)   A 3% error was attributed to the interpretation of the monitor photodiode spectrum due to placement of cursors and evaluation of pileup.

3) A 3% error on the determination of the active area of the photodiode, given a 20 µm depletion with a defined active area of 3.2 mm².

4) The error in correcting for the off - axis location of the monitoring photodiode (relevant for the first series of irradiations) was 5%

5) Errors due to the beam profile of 5%.

These errors combine in quadrature to produce a total uncertainty in the dosimetry of 10%.

3.3 Auxiliary dosimetry

3.3.1 General

To characterize the proton beam overall, several relative dose measurement techniques were used; film, TLD, RADFETs and caesium iodide (CsI) scintillator. Because of the beam dimensions and profile, none of these were suitable for shot-to-shot beam monitoring They are described here as lending support to the photodiode pulse counting used as shot-to-shot dosimetry and also supplementing the information on the beam profile.

Beam uniformity was studied as follows: at the start of the first proton irradiation campaign, the cyclotron operator centred the beam as far as possible using the beam currents from collision of the beam edges with the circular collimator at the end of the drift tube. The proton flux profile was then measured by moving a single counting diode across the key central area of about 25 x 25 mm to be occupied by the largest CCD chips. At the same period in the campaign, an array of RADFETs obtained dose responses at five points in the central area. For the second campaign, before CCD exposures, two array methods were used to give better feedback to the operator when centering the beam. These were:-

(a) measurements from an array of photodiodes as given in Section 3.2.3. (b) measurements from an array of CsI crystals, viewed by TV camera, as described below. Other array measurements, such as x-ray film and TLDs gave after-the-fact data on the beam profile at given times in the campaign. In addition, single RADFETs and TLDs were placed beside the CCD socket or on the shield, during most CCD shots but, due to a combination of the requirement to avoid shadowing the CCD and the rapid falloff of the beam outside the chip area, the shot-to-shot results from TLDs and RADFETs were not reliable.

3.3.2 TLDs

A close-spaced array of Harshaw TLD-100 thermoluminescent dosimetry chips was placed in the proton beam at the end of the second campaign. A machined perspex holder gave an accurate pitch spacing of 4mm and an array width of 40 mm. The array thus extended well beyond the edges of any CCD chip which was to be placed in the beam (maximum about 25 mm). The TLDs were held in their slots by a layer of 25µm polymeric cling film which should give negligible attenuation. The assembly was fixed onto the cold finger in the Leicester vacuum chamber or (in the absence of the chamber) centred on a plate bolted to the end of the beam pipe. The TLD-100 chips were read with a Harshaw 2000 reader (on loan from ESTEC) and calibrated against Brunel's Farmer air ionization chamber in the Physics Department Co-60 gamma cell.

Fig. 3.4 shows the setup for one exposure of 2 seconds in the proton beam, running with a typical current, collected from the proton scattering foil, of 10 pA. Fig 3.5 shows the TLD doses recorded. The profile lies within a 10 percent band over a length of about 14 mm but falls off rapidly outside this area. The responses of TLDs placed off-axis in every other CCD shot was erratic and that could be explained by this rapid fall-off.

3.3.3 Film

Kodak DE X-ray crystallography film was selected for use because this film is processed regularly at Brunel and repeatability of development is an important part of dosimetric accuracy in film. The optical density of small areas (about 1 sq. mm) was read using an EEL Universal Optical Densitometer used for reading X-ray film in Brunel Physics Department.

The response of the film to ionization was calibrated against a Farmer air ionnization chamber in the Brunel Co-60 cell. A virtually flat field of 0.01 rad/sec gave an optical density change of 0.6 for 1 rad(air) after film development in closely defined conditions of developer concentration and time. Fig. 3.6 shows the profile obtained from a 2-second exposure in the proton beam in a region of the film 5mm from an edge placed near to and parallel with the TLD array discussed above.

3.3.4 RADFETs

RADFET devices of type REM 501C, in 14-lead DIL polymeric chip carrier packages without encapsulation, were exposed as arrays and also individually in every other CCD shot. The devices were exposed in the unbiassed condition (all leads grounded in conductive foam).

The results of several shots on an array of five TLDs at a spacing pitch of 11 mm are shown in Fig 3.7. These were carried out before the first CCD exposure campaign and confirmed the readings of the photodiode counter with respect to the uniformity to be expected within and outside the CCD chip area.

The responses of RADFETs placed off-chip in every other CCD shot was erratic. Due to the size of the DIL package, the chip positions were usually at least 20 mm from the chip centre. This could be explained by the rapid fall-off of the proton beam outside the chip area - see section 3.3.2

3.3.5 Caesium Iodide Crystals

It is in the interest of the cyclotron user to provide feedback to the machine operator with respect to beam position and profile. The object of the crystal array was to give the operator a visual indication of an actual dose rate profile in two dimensions. After experimenting with plastic scintillator sheets and powder phosphor screens, it was decided that the necessary efficiency for the cyclotron conditions would be obtained with a mosaic of CsI crystals. Eight crystals, of size 10x10x20 mm were clamped together to form a mosaic. These were clamped in a metal frame, attached to a perspex plate, which was in turn bolted onto the end of the cyclotron drift tube. The crystals were separated into quadrants by thin opaque foils. The metal frame was drilled to accept photodiodes which could monitor the luminescence from each quadrant and hence detect imbalances between parts of the proton beam. A miniature TV camera was cantilevered to the outside of the perspex plate and other CCTV cameras could view the array from different angles as required. Metal crosswires on the frame were designed to act both as shadows for the proton beam and as Faraday cups. To improve light intensity viewed from outside, thin reflective aluminium foil was placed between the proton beam and the crystals.

Fig. 3.8 shows the physical arrangement on the end of the beam tube, with a TV monitor and TV camera. Fig. 3.9 shows the proton beam magnetically scanned in one direction and Fig 3.10 shows beam scanning in two directions. The use of images like these in real time to guide the operator led to improvements in beam uniformity as demonstrated in the diode count profiles shown in Section 3.2. Limitations of beam time did not allow an extensive study of photodiode responses as a check on drift but measurements were made which showed that adequate signals were available using conventional DC transimpedance amplifiers; that is, scintillation counting was not necessary at the dose rates used.
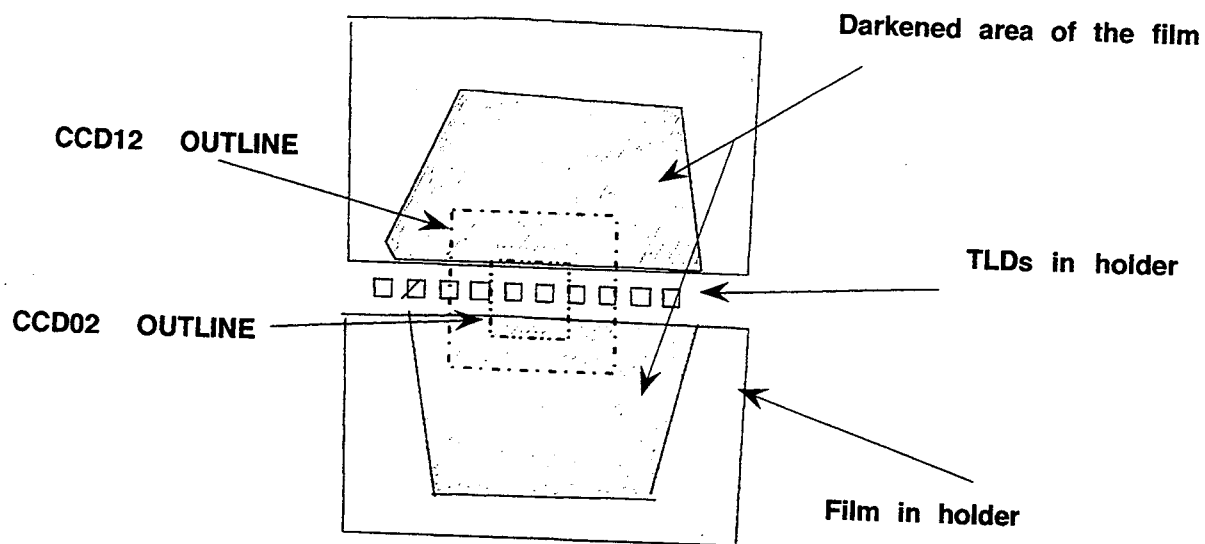
Fig. 3.4 X-ray film and TLD array exposure setup on the University of Birmingham radial ridge 6.25 MeV cyclotron
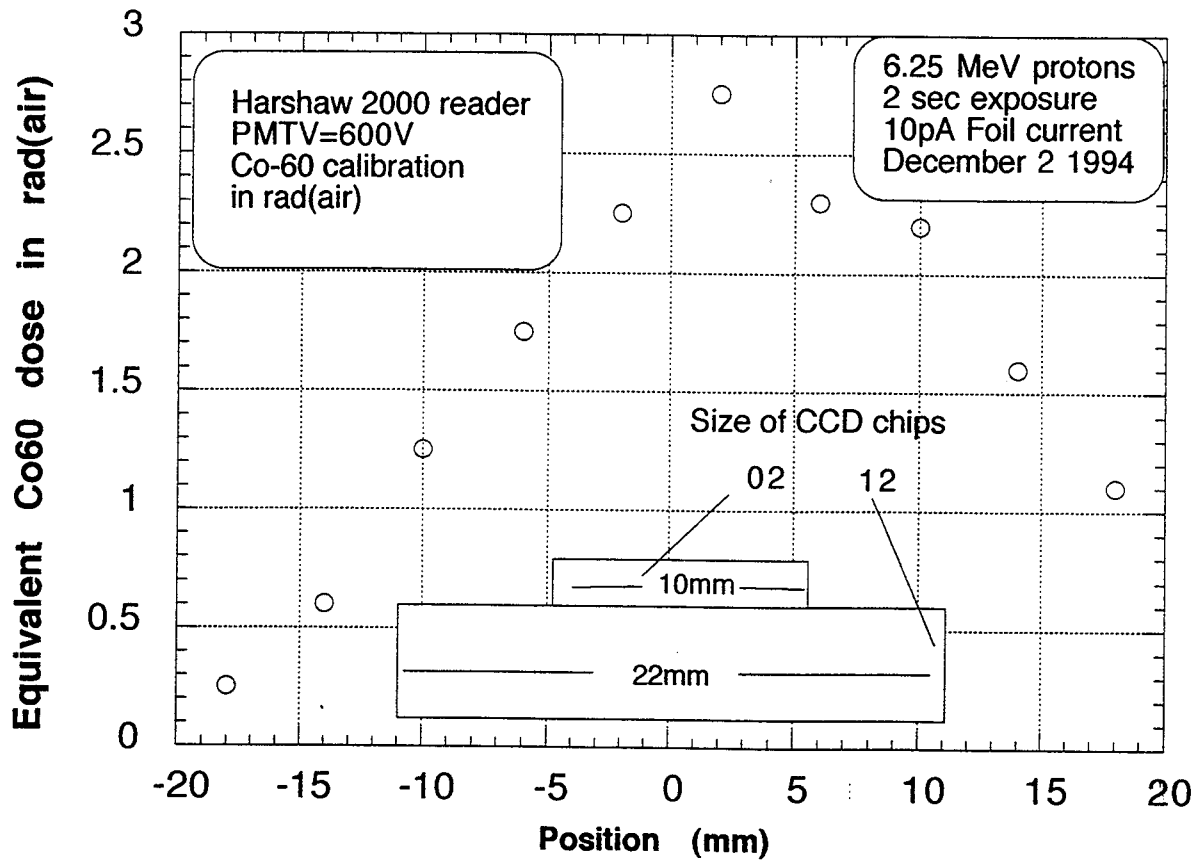
Fig. 3.5 Dose versus position for TLDs exposed in the University of Birmingham radial ridge 6.25 MeV cyclotron.
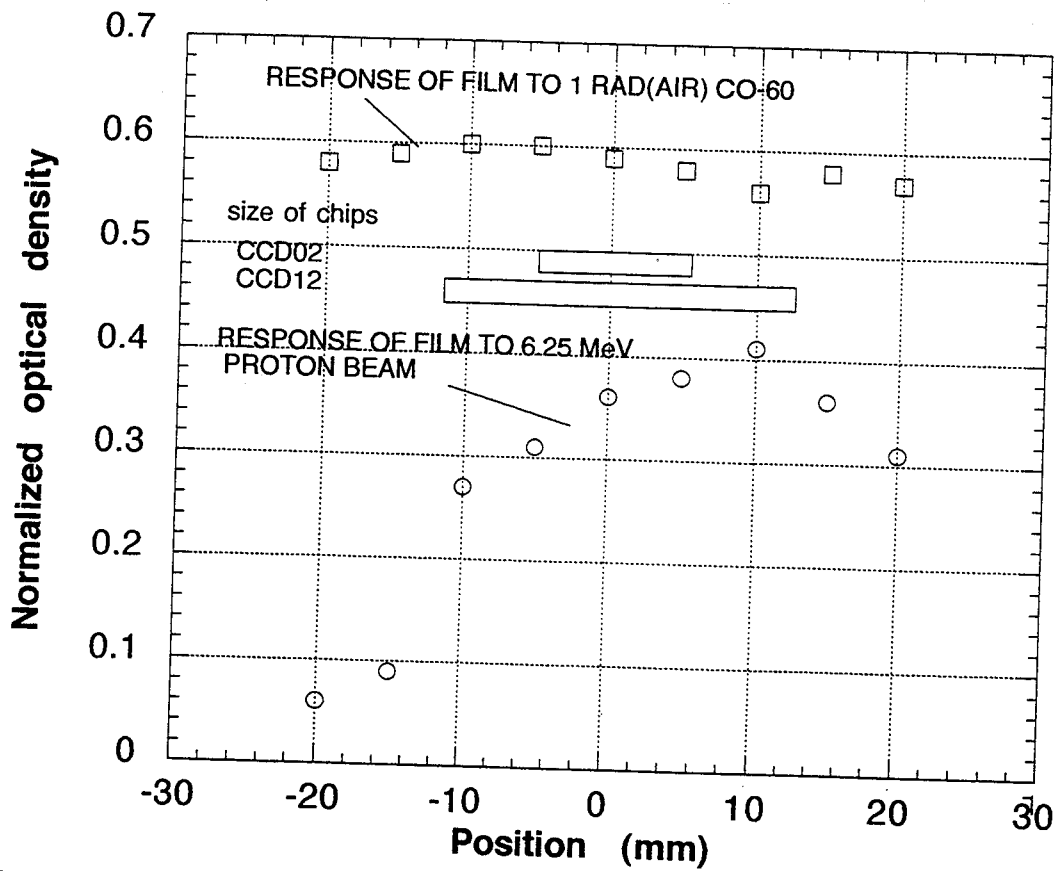
Fig. 3.6 Optical density versus position for X-ray film exposed in the University of Birmingham radial ridge 6.25 MeV cyclotron. Exposure 2 secs Dec 2 1994. Compared to flat-field gamma ray exposure of 1 rad(air)
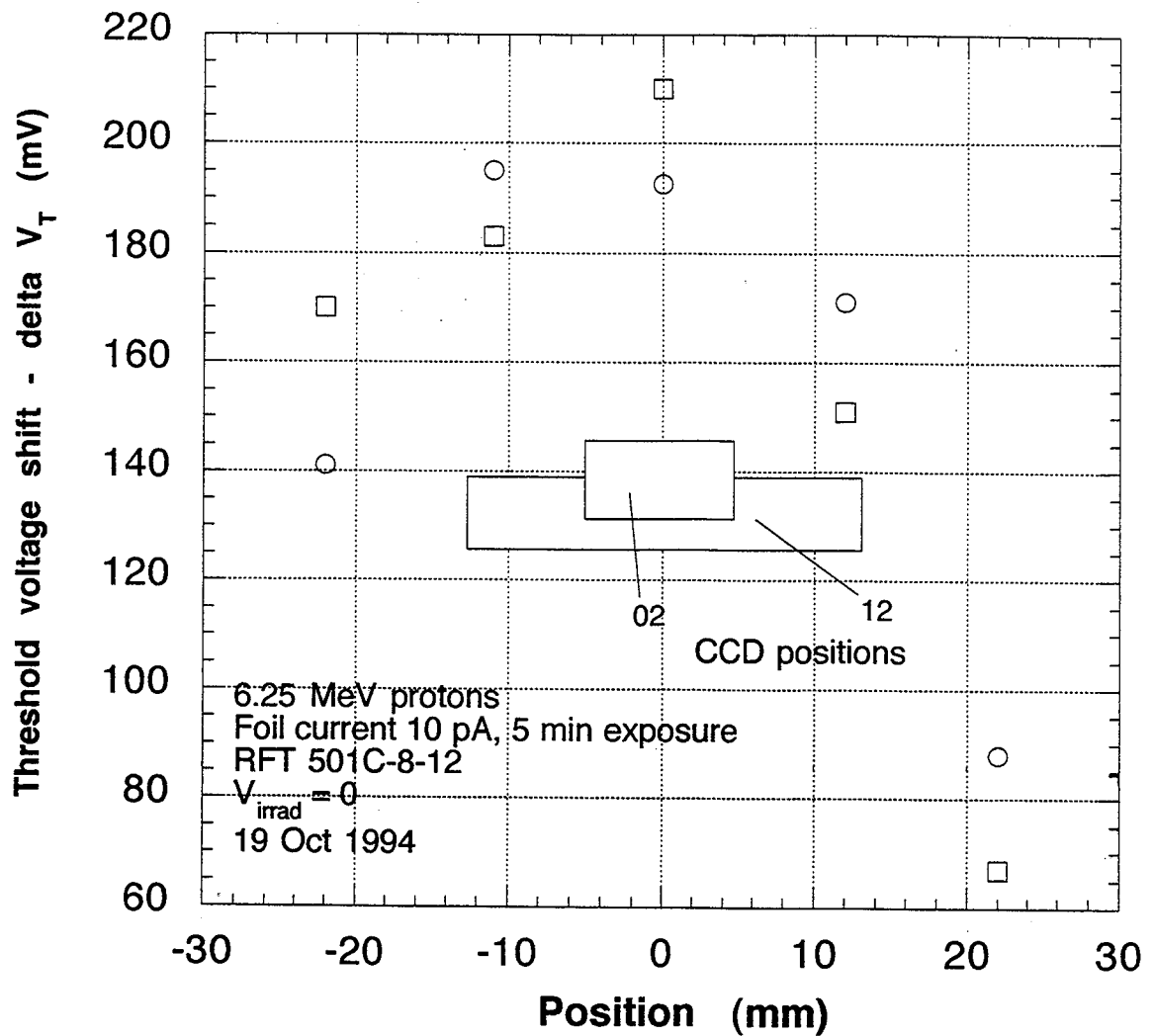
Fig. 3.7 Response of 5 RADFETs as a function of position.
Exposed in the University of Birmingham radial ridge 6.25 MeV cyclotron.
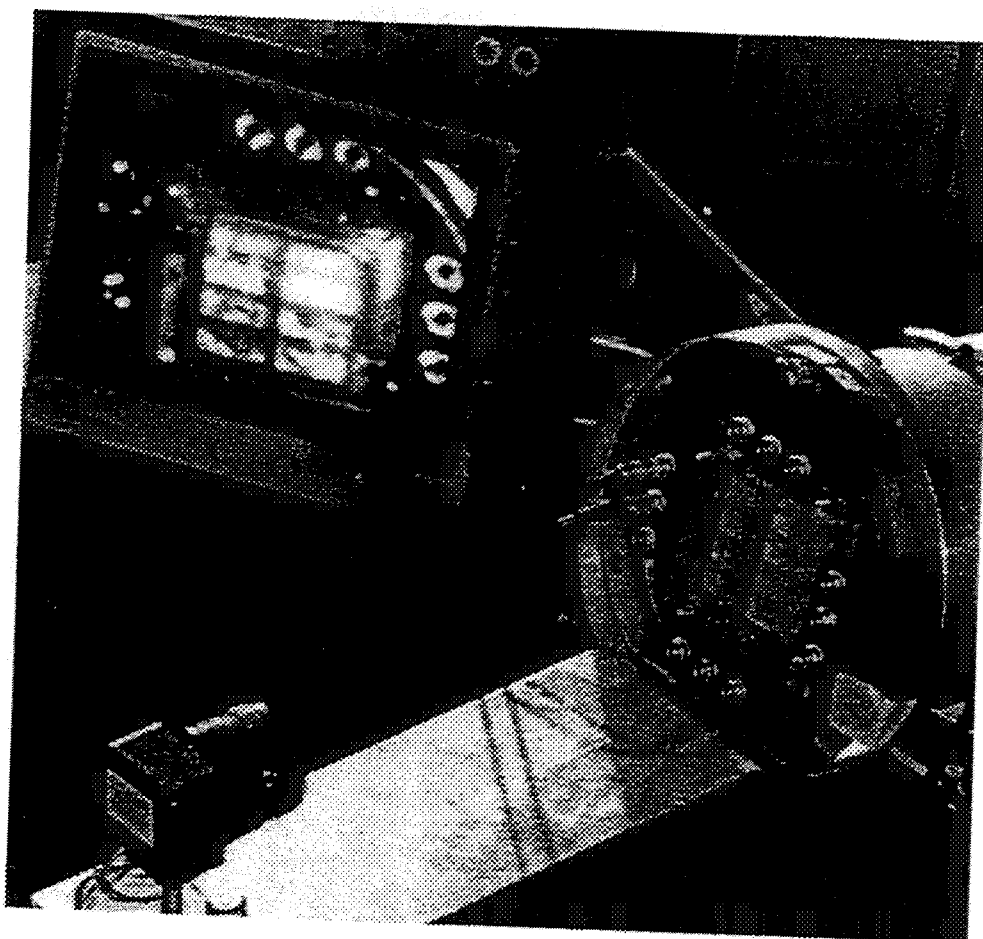
Fig. 3.8 View of Caesium Iodide crystal assembly at the
end of the cyclotron drift tube including (a) assembly
of crystals behind a perspex window (b) TV camera
(c) TV monitor
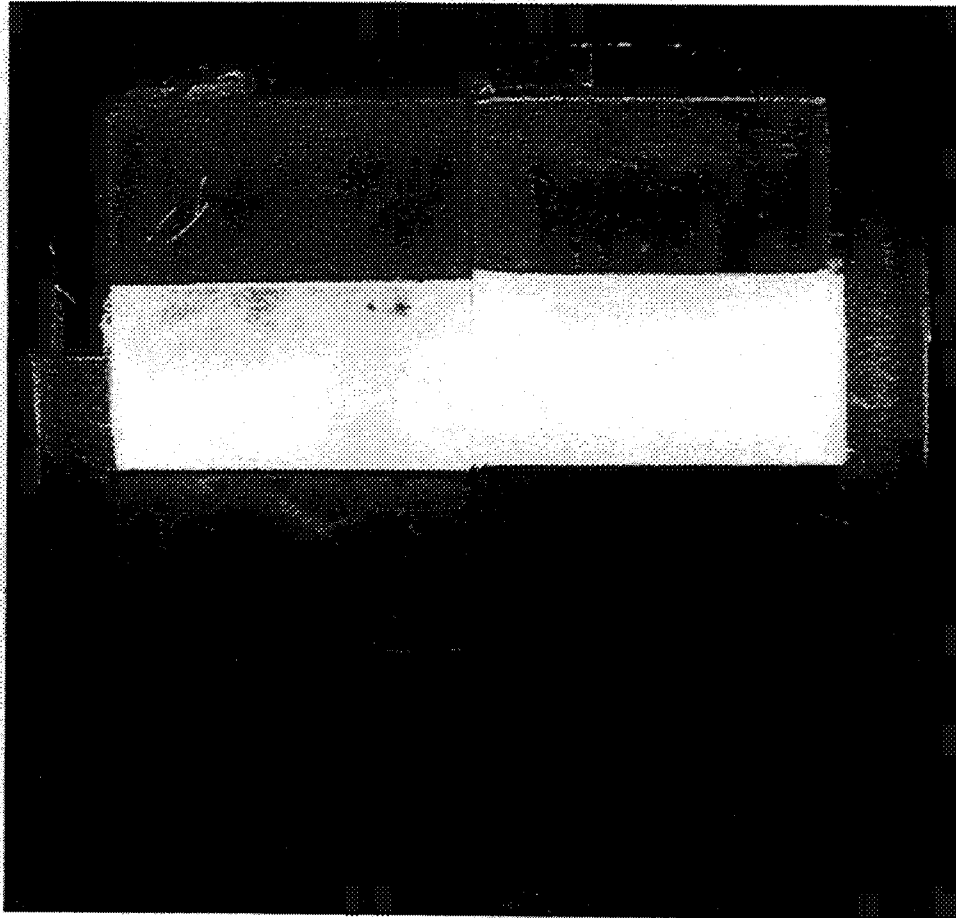
Fig. 3.9 Luminescence of the Caesium Iodide crystal
assembly in the 6.25 MeV proton beam of the
University of Birmingham radial ridge cyclotron.
Magnetic scan in the x direction.
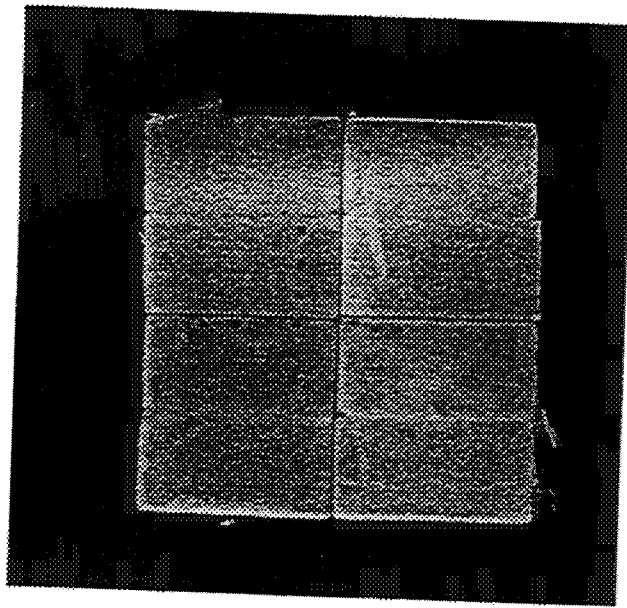
Fig. 3.10 Luminescence of the Caesium Iodide crystal
assembly in the 6.25 MeV proton beam of the University
of Birmingham radial ridge cyclotron. Scan in x and y
directions

3.3.6 Dark current frames and video traces

Evidence as to the uniformity of the proton beam is within the limits of the CCD02 chip is obtainable from the CCD damage profiles themselves. For example, Fig. 3.11 shows a video line from one of CCD02 devices, half of which received the proton flux and half which was shielded. The flatness of the dark current signals from the two halves is virtually the same, indicating uniformity of proton damage well within ten percent from edge to middle. The accuracy of this as a dosimetric method is limited by the distortions introduced by AC coupling of the video output in the present circuit. Caution is needed, however, because of the the presence of fixed patterns in dark current, while time-dependent (e.g. annealing) phenomena are common. These are limitations on the use of use of dark current signals as an absolute dosimetry method.

Fig. 3.12 shows a video trace of one of the back-illuminated CCD02 chips (see e.g Verhoeve 1991) irradiated uniformly with protons by SRON Utrecht in the WO1 project. The dark current exhibits several steps. These are are not due to irradiation. These devices were back-thinned, and the non-uniform dark signal is undoubtedly associated with current collected from the back of the device. It should be noted that these devices date from around 1990 and are not representative of the current state of this technology.

Finally, Fig. 3.13 shows a frame of dark current signal from an irradiated CCD12 device. The boundaries of the irradiation are roughly the same as the boundaries of photolithographic mask stepping known as stitching. However, detailed analysis shows that certain regions of the device, associated with the same mask - whether irradiated or not- show more dark current than others. These non-uniformities are related to the processing not to the proton irradiation.

3.4 Proton exposure values

Table 3.4 shows the actual proton exposure values administered. The 6.25 MeV fluences have been converted into equivalent 10 MeV fluences in order to assist comparison with WO1 and other projects.
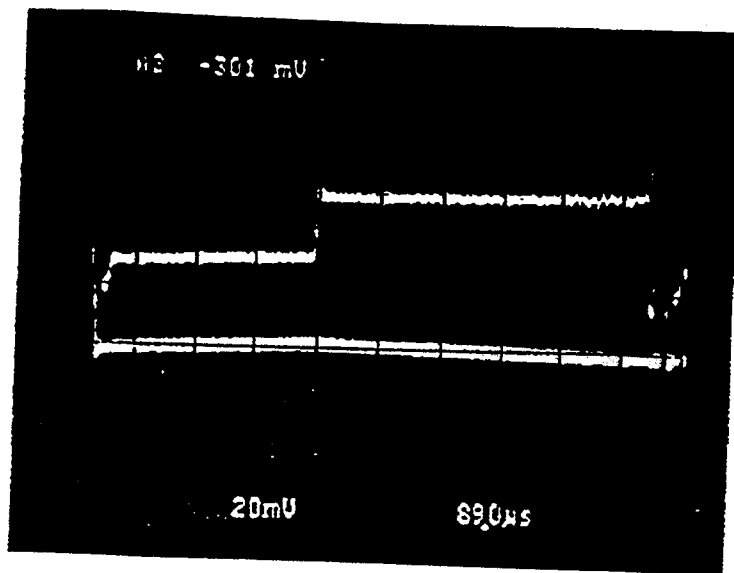
Fig 3.11 Video trace of dark signal; EEV CCD02-9 after
irradiation of half the area with 6.25 MeV protons at a
fluence of 1.22E9 per square cm. Oscilloscope image
of one line, scanned at 2 microseconds per pixel.

The dark signal is the difference between the bright,
near-flat baseline and the bright upper line. The step
in the centre represents the transition from shielded to
exposed areas of the chip. Temperature is 299.3K. The
dark current is of order 1 nA. Vss was 6V.

This trace indicates that the proton beam profile was
uniform to 10% or less
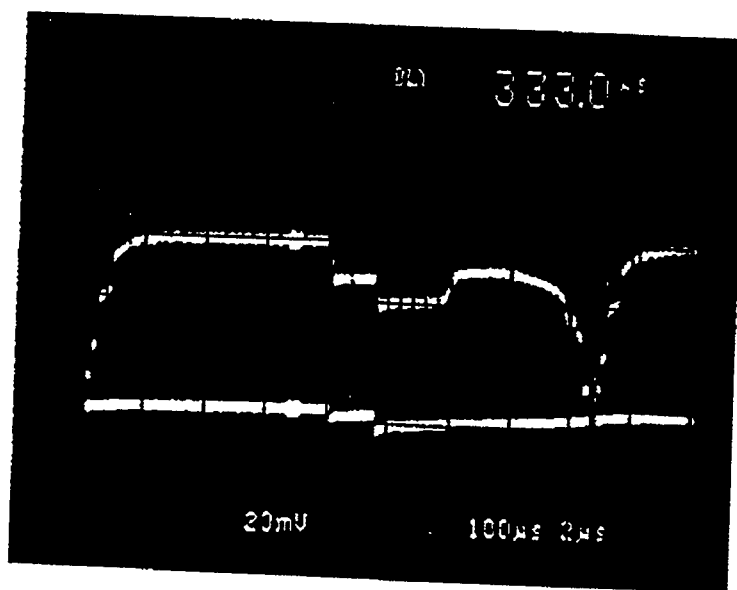
Fig. 3.12 Video trace of dark signal; EEV CCD02 sample
R437 after total irradiation by 2.0 MeV protons at a
fluence of 2.3E8 per square cm. Readout and temperature
conditions are as in Fig. 3.11.

The steps in the centre represent material transitions
probably associated with backside thinning and are
definitely not due to the proton irradiation. The
dark current is of order 1 nA.

See text for further comments.
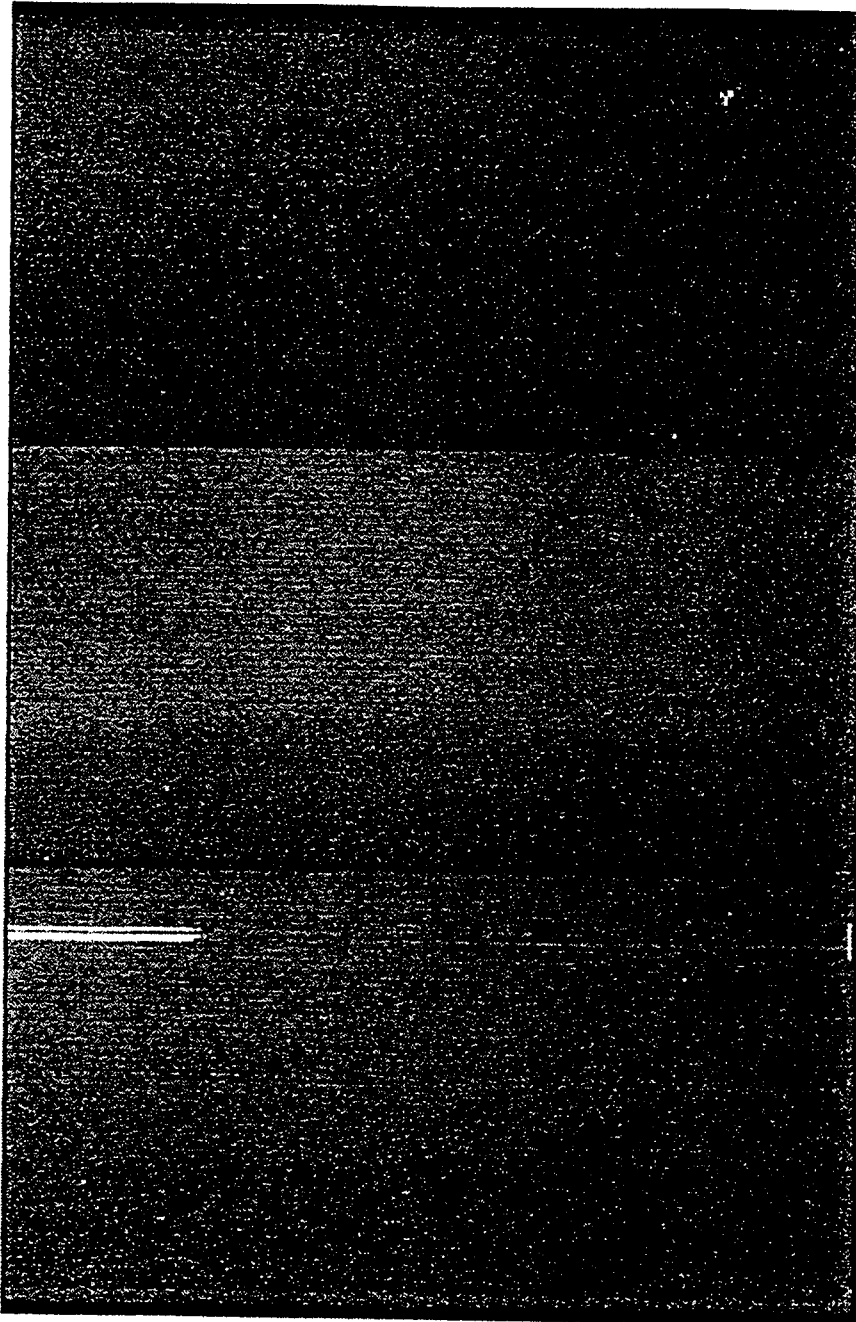
Fig. 3.13 Dark signal fixed patterns; frame from an EEV
CCD12 sample after irradiation with 6.25 MeV protons.
The image was acquired under slow scan conditions
at cryogenic temperature. High dark current is indicated
by lighter shading.

The boundaries of the photolithographic mask stepping,
known as stitching, are visible. The radiation shield was
moved to give one-third of the chip the largest dose.

The dark current non-uniformity is not associated
with the proton irradiation but with the processing.

Table 3.4 Fluence Equivalents delivered to the CCDs

Test Device	Device No.	Silicon	Fluence (cm^{-2}, 10MeV equiv.)		
			Left	Mid	Right
CCD02-1	A0962-15	20μm Epi	1.46E9	N/A	Contrl
CCD02-2	A0962-16	20μm Epi	1.48E9	N/A	Contrl
CCD02-3	A0962-19	20μm Epi	1.43E9	N/A	Contrl
CCD02-4	A0962-20	20μm Epi	1.41E9	N/A	Contrl
CCD02-5	A0962-21	20μm Epi	1.46E9	N/A	Contrl
CCD02-6	A0962-24	20μm Epi	1.44E9	N/A	Contrl
CCD02-7	A0962-26	20μm Epi	1.43E9	N/A	Contrl
CCD02-8	A0962-31*	20μm Epi	1.43E9	N/A	Contrl
CCD02-9	A0962-33*	20μm Epi	1.22E9	N/A	Contrl
CCD02-10	A0962-49	20μm Epi	Contrl		
CCD15-1	A2027/3/6	50μm Epi	1.02E8	5.36E7	Contrl
CCD15-2	A2028/15/1	50μm Epi	2.58E8	1.34E8	Contrl
CCD15-3	A2028/15/6	50μm Epi	6.47E8	2.36E8	Contrl
CCD12-1	A3197/5/4	100μm E	1.20E8	6.60E7	Contrl
CCD12-2	A3197/5/5	100μm E	1.74E8	1.20E8	Contrl
CCD12-3	A3197/5/9	100μm E	2.40E8	1.21E8	Contrl
CCD12-4	A3197/5/10	100μm E	2.05E8	8.46E7	Contrl
CCD12-5	A3196/6/7	100μm E	6.56E8	4.17E8	Contrl
CCD12-6	A3196/6/8*	100μm E	6.18E8	3.89E8	Contrl
CCD12-7	A3188/17/7	Bulk	1.09E8	5.40E7	Contrl
CCD12-10a	JET-X	65μm Epi	5.78E7	N/A	Contrl
CCD12-10b	JET-X	65μm Epi	2.44E8	N/A	Contrl
CCD12-10c	JET-X	65μm Epi	6.28E8	N/A	Contrl

4. ANALYSIS OF RADIATION EXPERIMENTS

4.1 Theoretical background to CTI degradation

The increase of Charge Transfer Inefficiency (CTI) with irradiation is measured in this project by analysis of computer captured image frames, including the compilation of stacked line traces. Peak values for X-ray signals, e.g. from Fe-55 "hits" or other X-ray photons, at different distances from the output register, show different amounts of charge loss. Fitting a curve to the peak signal values, plotted as a function of pixel number, yields CTI values as small as 1E-6 before irradiation.

In proton-damaged CCDs, important differences between serial and parallel CTI degradation are apparent. A clear temperature dependence is observed. The full explanation of these effects requires a deeper knowledge of the microscopic properties of the defects produced by protons. Here, we will make use of the model developed at Brunel by Robbins 1992. This model is theoretically complete and can explain all the data presented here. The CTI due to one trap species can be written as:-

$$CTI = \left[\frac{n_T}{n_s}\right] \times G(t_o, T) \times \sum_{j=1}^{j=ngates} F_j \qquad ..4.1$$

where n_t is the trap density (cm^{-3}) and n_s is the signal density (cm^{-3}) and to is the time between charge packets. The G-factor, $G(t_0, T)$ depends on t_0 and the temperature T (Kelvin). The G-factor is given by:-

$$G = (1-\exp(-t_0/\tau)) \qquad ...4.2$$

where, τ is the emission time constant for the trap which depends very strongly on the temperature.

τ is given by:-

$$\tau^{-1} = \sigma_n X_n v_{th} N_c \exp((E_t - E_c)/kT). \qquad ...4.3$$

The parameters in this equation are well known. See Robbins 92 for further information. The most critical parameter is the position of the trap in the bandgap given by (E_t-E_c), where E_t is the energy level of the defect. Defects can be in the original material, or produced by irradiation. For the Si-E, or vacancy-phosphorus centre, τ is known to be described by (Robbins 92, using electron irradiation);

$$\tau^{-1} = 42600 \, T^2 \exp(-5446/T) \text{ milliseconds.} \qquad ...4.4$$

Data from Hopkinson (1995) for proton irradiated EEV CCDs gives;

$$\tau^{-1} = 6902T^2 \exp(-4821/T) \text{ milliseconds.} \qquad ...4.5$$

This gives a value of 2.6 milliseconds and 6.1 milliseconds at -40 °C for equations 4.5 and 4.4 respectively. The difference between these formulae is due to the more complicated nature of defect production in proton irradiated devices.

The fill-factor, F_j for phase i, is

$$F_j = 1-\exp(-t_g/t_c) \qquad ...4.6$$

where t_g is the time the charge packet spends under one gate and t_c is the capture time constant for the trap. t_c is sensitive to the signal density and temperature. F is less than 1.0 if some traps are not filled as the charge packet is transferred under a gate. This only happens

at high clock rates. For the clock rates used in this report and for most slow-scan systems, the fill factor term will effectively be 1.0. The EEV CCDs tested in this project are all three-phase devices. Thus the last factor in the Equn.4.1 above is 3.0.

For several trap species the total CTI is just the sum of CTI terms given by equation 4.1.The maximum CTI occurs when the G-factor and fill-factor are unity. The CTI is then:

$$CTI_{max} = 3(n_t/n_s).$$

...4.7

From this formulation, we can identify all the CTI effects seen in CCDs:-

a) The trap density, n_t, depends upon the irradiation source and defect kinetics in the device. The only way to reduce the radiation-induced trap density is by defect engineering.

b) The signal density, n_s, is affected by X-ray energy and the volume of the n-channel containing the electron signal. Therefore, radiation tolerance can be improved by the use of either supplementary or narrow channel technology.

c) The G-factor controls a large number of the observed effects, namely:-

i)   The strong temperature dependence of the CTI, which is linked to τ.
ii) The hit-rate and clock-rate dependence of the CTI, which is linked to t_o.
iii) The temperature dependence of stacked-line traces.

4.2   CTI Degradation vs. Operating Temperature

4.2.1   Temperature dependence, WO1 data

In proton-irradiated CCDs tested in WO1, we found strong changes of CTI with temperature in the range -50°C to -120°C in CCDs after irradiation. Further analysis since the end of WO1 has been extensive (see, for example, Holland 1993, Robbins 1993). The information on defect levels produced by measuring CTI at a few discrete temperatures is analogous to but not so precise as that produced by DLTS scans on diodes. The measurements of these peaks in the temperature dependence curves (see Fig. 2.3) show that, in the EEV CCD buried channel, at least three trap species are active.

Table 4.1 summarizes the trap situation in proton irradiated epitaxial CCDs (CCD02) after a fluence of 3.6E9 10 MeV protons cm^{-2} (Holland 1992):

Table 4.1   Trap levels found in proton-irradiated CCD02 devices

Trap	Energy Level (ev)	Pre-irradiation Concentration (cm^{-3})	Post-irradiation Concentration (cm^{-3})
E1	Ec-0.12	3E10	6E10
E2	Ec-0.30	7E8	7E9
E3	Ec-0.42	-	3E10

E3 probably consists of a pair of defects; 85% is due to the VP centre, which is removed by annealing to +150 °C. The un-annealed concentration (15%) is highly likely to be due to the divacancy (VV). There may be a small amount of another defect, denoted by EX which is mentioned further in Section 4.10 and which anneals at around 80 °C. The E3 complex dominates the CTE degradation in the temperature range -120 to -50 °C .

The E1 and E2 centres are observable before irradiation and provide the limitation on the as-processed CTE. Concentrations increase after irradiation as shown in the table. Recent work with CCD02 devices suggests that the trap designated E2 may not be present before irradiation in CCDs fabricated on float-zone silicon.

In Table 4.1, the radiation-induced concentrations of E1 and E3 are both $3E10$ cm^{-2}. If the tentative assignments given in the table are correct, then defect kinetics considerations (Section 5.2.2) imply a free oxygen concentration in the material of about $1E17$ cm^{-3}.

4.2.2 Energy level extraction, WO2 data

In WO2, CCD02 devices were irradiated to a fluence equivalent to about $1E9$ 10MeV p cm^{-2}. The CTI values were then measured at -70, -90, -110 and -130 ^{o}C. The values are shown in Fig. 4.1. These devices are all from the same wafer - A0962. The data has been normalised to a fluence of $1E9$ 10 MeV p cm^{-2}. The curves shown are fits to the data using the form;

$$CTI= CTI_{background} + CTI_{max}(1-exp(-42600t_0T^2exp(-\Delta E/kT)) \qquad ...4.8$$

where ΔE was fixed as 0.42eV and t_0 was allowed to vary. Using constants from equation 4.5 gives the same values of CTI_{max}, and values of t_0 which are a factor 4.9 times smaller.

The data is well grouped for devices CCD02-1 to 5. The data for CCD02-7 to 9 suggests that measurement conditions affecting the time between charge packets may have been different. Later study of the log book shows that the integration period was doubled to ensure that the number of hits per frame was constant. This would also affect background charge levels. Despite such information it has proven impossible to explain the variance in the data due to such a change in conditions.

This data is consistent with the previous interpretation that, for the operating temperatures used on XMM, the main damage is a defect centre(s) lying at $E_t = 0.43 \pm 0.04$ eV below the conduction band. This defect(s) gives rise to a sharp sensitivity to temperature which makes it highly preferable to operate below -90 ^{o}C. Not enough measurements were available to allow the trap energy to be extracted from fits to the data.

A comparison of the CCD02 devices is best done for a measurement condition in which both the G-factor and F-factor are 1.0, i.e. determining the maximum CTI. This is equivalent to asking whether each has a similar radiation induced trap density. This is the logic for selecting the -70 ^{o}C parallel CTI measurements. Fig. 4.2 shows this CTI normalised to $1E9$ 10 MeV pcm^{-2} for each CCD02. The square and circle points are from the fit- Fig.4.1 - or measured CTI respectively. All devices, except CCD02-1, are consistent within 10% with a CTI of (385 +/- 34) E-6. CCD02-1 is further discussed in Section 4.9.2.1. Rewriting equation 4.1;

$$n_t = \frac{CTI.n_s}{G.\Sigma F}$$

$$...4.9$$

We can use the CCD02 data to calculate n_t. This is best done at -70 ^{o}C, where G and F are well established, being 1 and 3 respectively. n_s is taken to be $7E13$ cm^{-3} - see Section 4.4. Thus, the CCD02 data implies that there is a density of;

$$(385E-6)\times\frac{7E13}{3}=0.9E10 \quad cm^{-3}$$ "0.4eV" defects in these devices after $1E9$ 10 MeV

equivalent protons cm^{-2}. This uses a signal density from the discussion in section 4.2 below. This is consistent with Holland 1992 - see above table.

4.3   Hit -rate and clock-rate dependence of CTI.

In the testing performed in WO1, the electron packet in the serial pixels was replaced about every 33 microseconds. For the parallel registers, the clock rate was 400 times slower (say 13,000 microseconds). It is clear from equn. 4.2 (G-factor) that it is essential to relate the dwell times of the electron packets to the release time constant for electrons from the radiation-induced defects. In WO1 the release time constant, τ, for the dominant centre in our samples was measured by EPER experiments to be the order of 10,000 microseconds at -90 °C, thus matching the parallel register rate quite closely. Recent analyses by Holland have shown that -90 °C is indeed an inconvenient working temperature and tradeoff studies are being made in the EPIC design project to avoid such a match. The WO2 data also indicates that -90 °C is not suitable for the XMM CCD operating conditions .

Holland (1993) developed a model in which the parameters of X-ray hit rate, temperature, trap species and clock rate were linked. In brief, temperature affects the trap release time constant, while this parameter and X-ray hit rate define the effective density of traps, N_{eff}, as follows:

$$N_{eff} = N_t [1\text{-exp} (-n_x t/\tau)]$$

..4.10

where N_t is the density of traps, n_x is the average number of unexcited pixels i.e. pixels which have not recently received X-ray hits, t is the pixel clocking rate (serial or parallel) and τ is the trap release time constant. The term in the square brackets is called the G-factor in section 4.1. It is the decrease in N_{eff}, brought about by an increase in τ, which produces the decrease in CTI as the device is cooled - see fig. 4.1

The model also shows that if X-ray response tests are done using an artificially high X-ray flux - compared to mission conditions - then an artificially low CTI is measured. A hit-rate dependence of the CTI can be seen in the WO1 data. The model suggests that in the WO1 reports we underestimated CTI by a factor as high as 2 for many of the measurements. For most of the WO2 measurements, we have reduced the X-ray flux to 10 photons. $cm^{-2}.sec^{-1}$. This is chosen to correspond to the expected cosmic ray background in the XMM orbit - the worst case condition in flight.Thus the time between hit pixels is crucial. This can be altered by changing either the hit density, the clock rate, or the amount of dark current. This effect has been quantified in the present work. Figs 4.3 and 4.4 show data for CCD12-5 after 6.56E8 and 4.17E8 protons cm^{-2} 10 MeV equivalent.

The data in Fig. 4.3 has been fitted to the function,

$$CTI*1E6 = A + B*(1\text{-exp}(-(X/(Background\ Rate + Rate)))$$

..4.11

where the following parameters are fixed as A = 20, B =100 and Background Rate = 5. This function follows from equn. 4.1. The values for these parameters were chosen as follows:-

A = lowest CTI at -110 °C, i.e. for high flux; this is the asymptotic level and is not related to the 0.4eV centre.

B = (-70 °C CTI maximum) - A; the CTI cannot go higher than this.

Background Rate = Rate at which the measured CTI does not alter at very low photon rates. If it were not for the background rate, the CTI for all temperatures would be maximal (120E-6) at a rate of zero. Note that one can easily fit the data with the background rate set to zero. In other words, there is not enough data to constrain the background level in the fit.

The fitted values of X were 116, 25 and 5 at -70, -90 and -100 Centigrade respectively, with and error of about 10%.

The same procedure was used for the data in Fig. 4.4 with A=14, B=68 and Background Rate = 10. The fitted values of X were 110, 20 and 3 at -70, -90 and -100 Centigrade respectively, with and error of about 10%. These are in excellent agreement with the values found for the data in fig. 4.3.

Stacked line traces (SLT's) are a useful way to study CTI degradation in CCDs that are to be used for low energy x-ray detection. It is important to test the devices under conditions that are close to the scientific operating conditions. We would argue that the periodic pulse technique using electrical charge injecion, Robbins 92, is to be preferred if one wishes to make detailed studies of bulk defects in the buried channel. It is possible to make such studies down to low signal levels - around 400 electrons. The prime reason for this is that t_0 is well-defined. With x-rays, although one may be able to define an average, t_o, it is subject to large statistical variations. This then causes the G-factor, and hence the CTI to suffer statistical fluctuations.

The G-factor for the PV centre is $1-\exp(t_0/t_e)$ = $1-\exp(42600tT^2\exp(-5446/T))$, where T is the temperature in Kelvin, and t_0 is the mean time between charge packets in milliseconds. Fig. 4.5 shows this time for a 400 by 600 CCD with 100 hits distributed randomly over its area. As one would expect, the average value of t_0 is just 2400 pixels. If the readout period is 20 microseconds, then to is 48 milliseconds. Fig. 4.5 shows that this time is distributed exponentially. This is not surprising - note the similarity to radioactive decay. If one now uses these times to calculate the G-factor at different temperatures a remarkable feature emerges. Fig. 4.6 shows G at 200K, 220K and 240K. 220K marks a transition point. Below this temperature G is close to zero and is distributed exponentially. Above this temperature almost all G values are close to one (worst case). At a **"critical temperature"** , T_c, the distribution is uniform. In other words, the G-Factor can be anywhere between 0 and 1 and the CTI is meaningless. Fig. 4.7 shows some simulated SLT's at these same temperatures. Below (above) T_c, the SLT has a tail to the left (right).

To understand this in more detail, statistical parameters of these distributions have been estimated using a spreadsheet as a function of temperature for various values of t_0. The parameters are the mean, standard deviation, skew and kurtosis. To those who are unfamiliar with skew and kurtosis, the important points about these measures are: positive (negative) skew means the distribution has a tail to the right (left) of the mean value; a positive (negative) kurtosis means that the distibution is more (less) peaked about the mean than a normal distribution of the same mean and variance. A uniform distribution has a skew and kurtosis of 0 and -1.2 respectively. Fig. 4.8 shows the behaviour of these parameters for a mean time of 4.8ms and 48 ms. This corresponds to 100 and 1000 hits per frame in the CCD described above. The critical temperature can be found from this figure (skew=0, kurtosis=-1.2). The low temperature regime is separated from the high temperature regime (G=1) by about 20 °C. In between, the G-factor and the SLT will be very poorly defined. Figure 4.9 shows how the critical temperature varies with mean time between charge packets. It should be remembered that as an irradiated device is warmed up to room temperature, dark current will define the mean time between charge packets, i.e. it will approach the readout period.

For a real irradiated CCD there will be other defects and the CTI model needs to be more sophisticated - emission of trapped charge back into the pixel. Nevertheless, if one looks at SLT's from WO1 - fig. 4.10, the behaviour predicted by this analysis can be clearly seen.

The key point to understand from this analysis, is that one should operate the device well away from the critical temperature otherwise there will be large fluctuations in the CTI resulting in poor x-ray energy resolution.
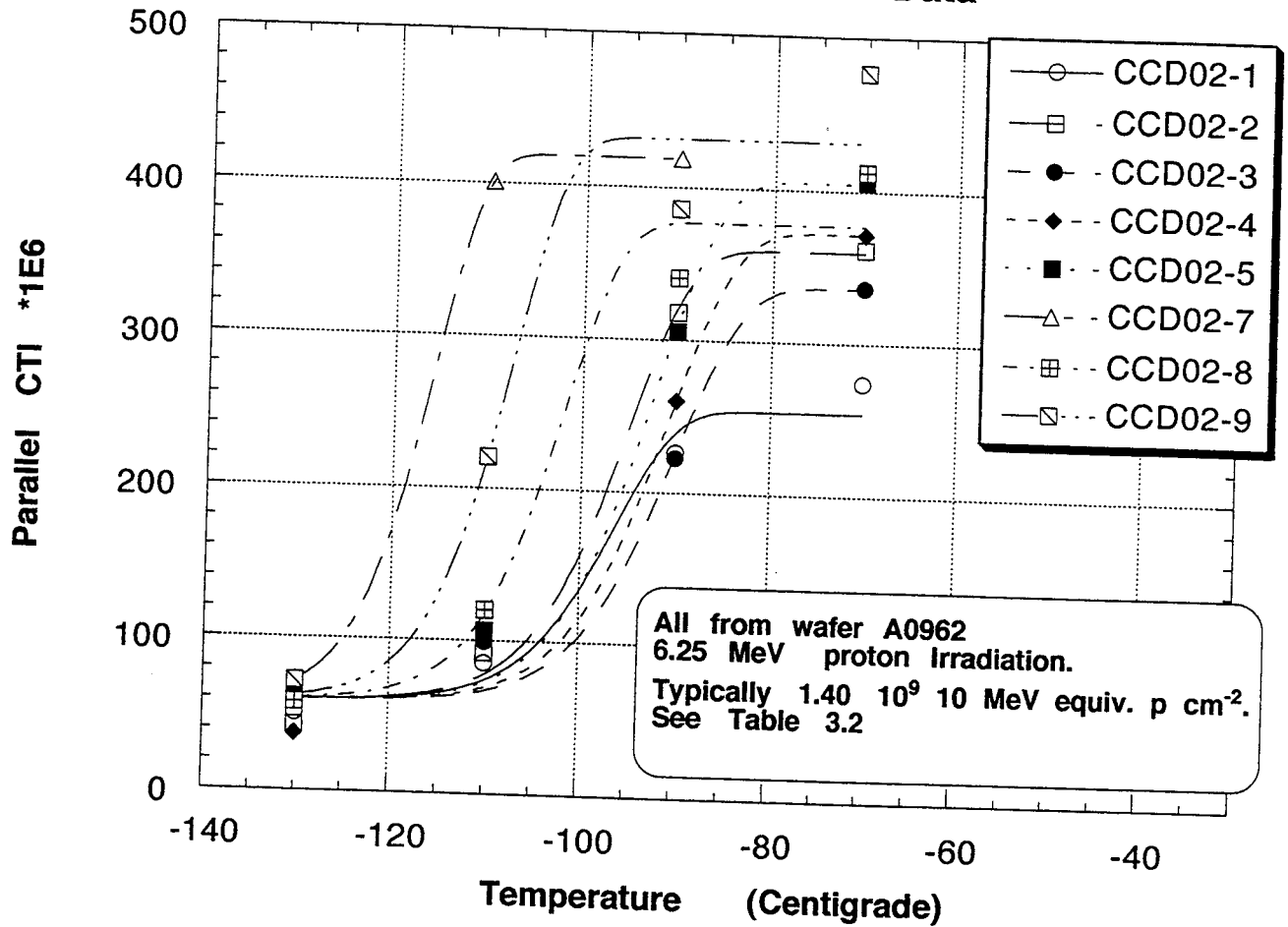
Fig. 4.1 Parallel CTI of CCD02 set after proton irradiation
versus temperature. Curves are fits to data using formula 4.8
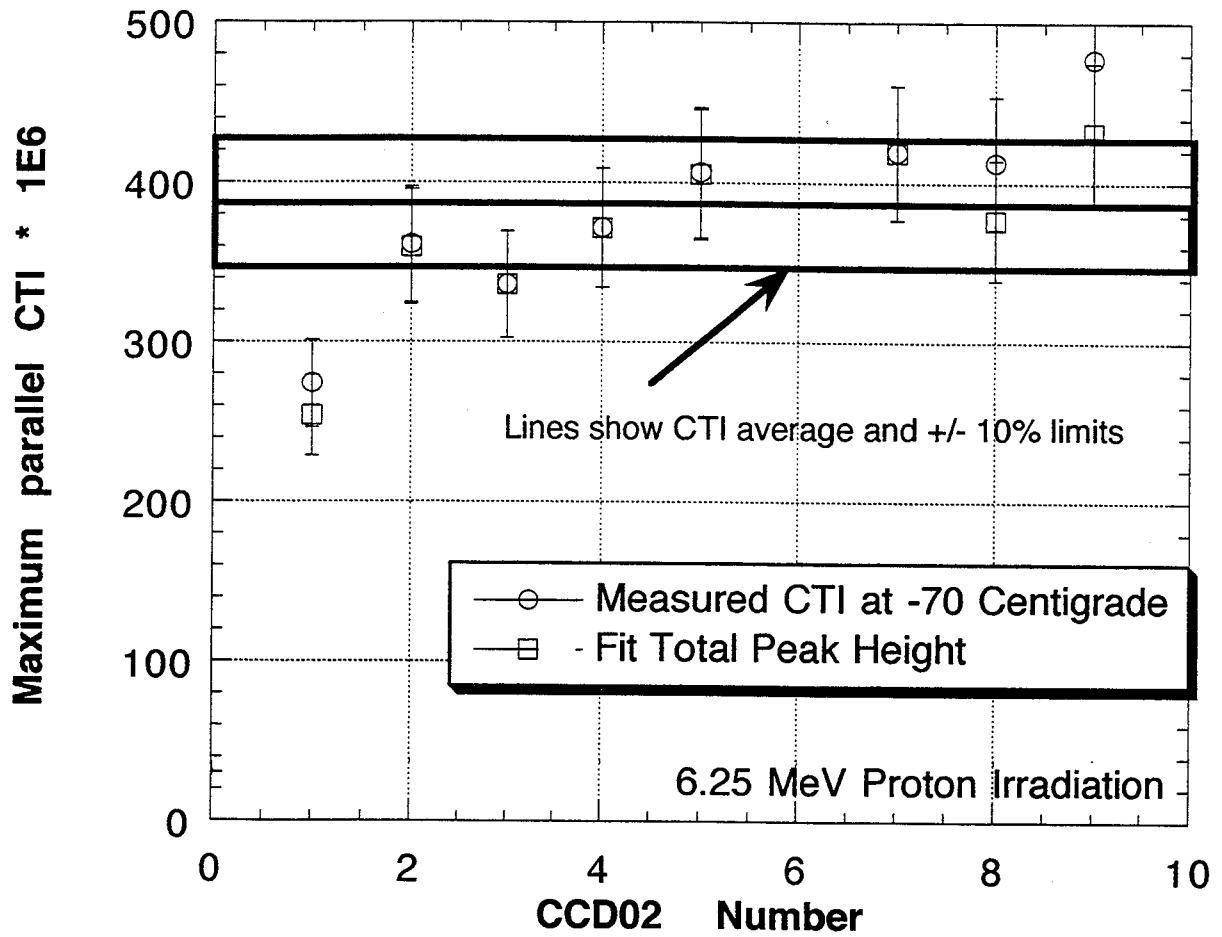
Fig 4.2 Maximum parallel CTI versus device number; all CCD02 devices are from the same wafer. Fluence typically 1.4×10^9 10 MeV equiv. p cm^{-2}.
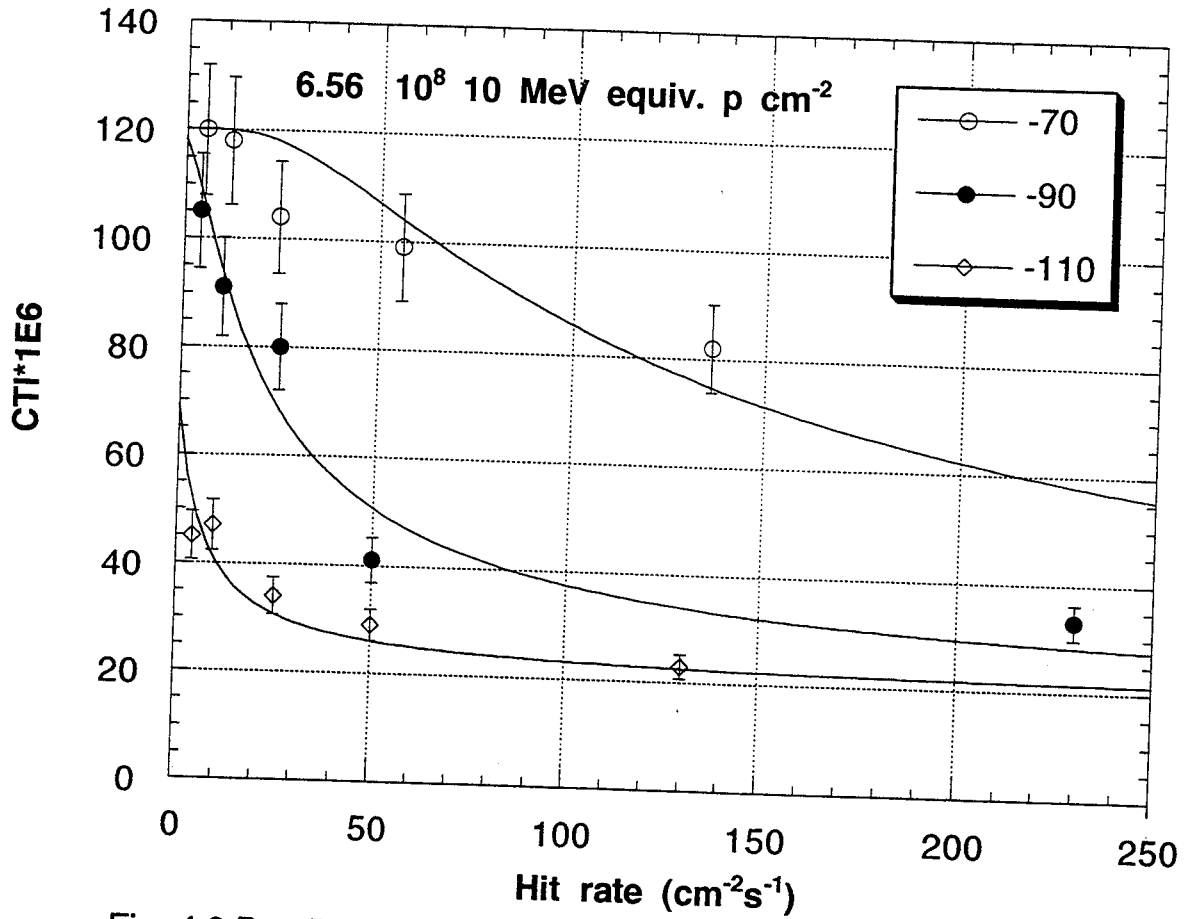
Fig. 4.3 Parallel CTI at -70, -90 and -100 Centigrade of CCD12-5 versus Fe-55 photon hit rate after 6.25 MeV proton irradiation Curves are fits to data using formula 4.11.
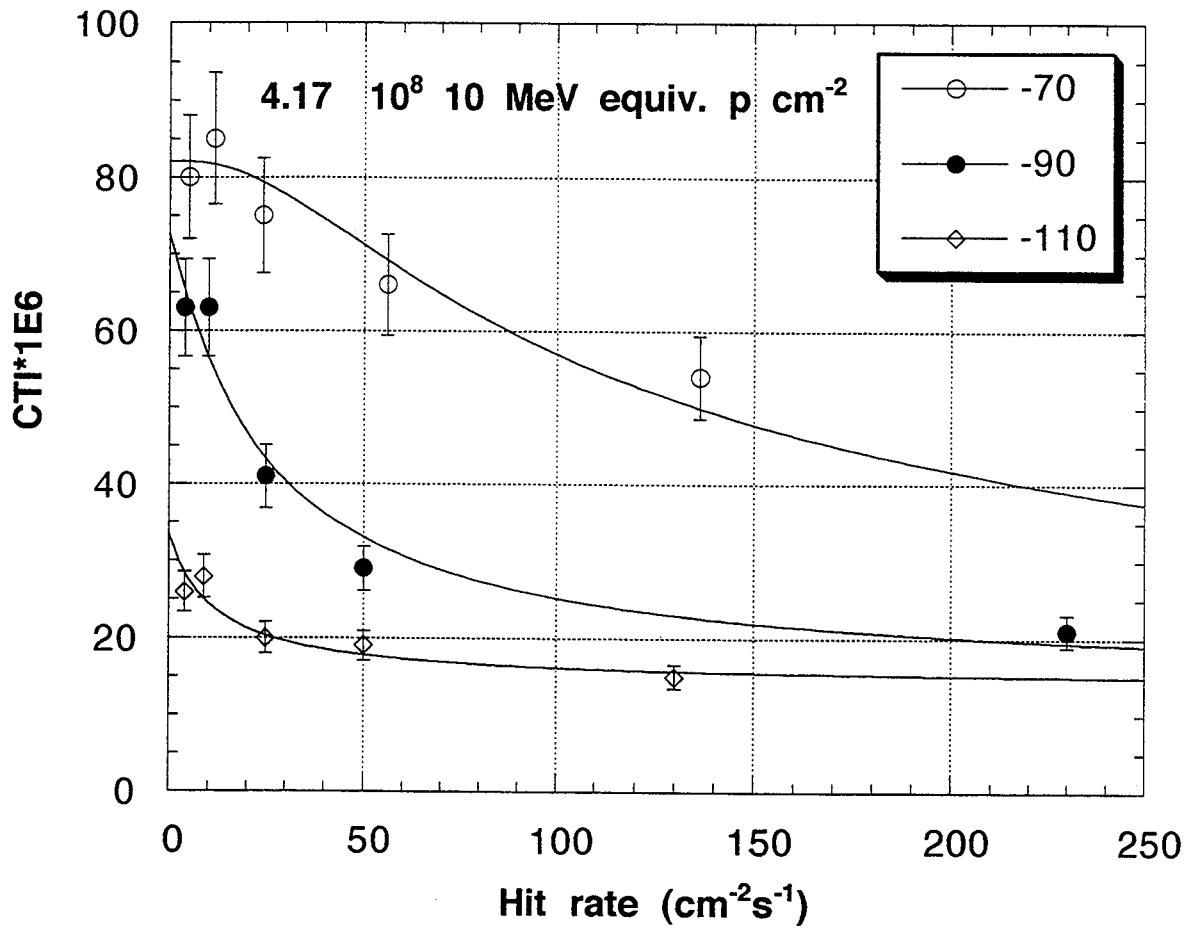
Fig. 4.4 Parallel CTI at -70, -90 and -100 Centigrade of CCD12-5 versus Fe-55 photon hit rate after 6.25 MeV proton irradiation
Curves are fits to data using formula 4.11.
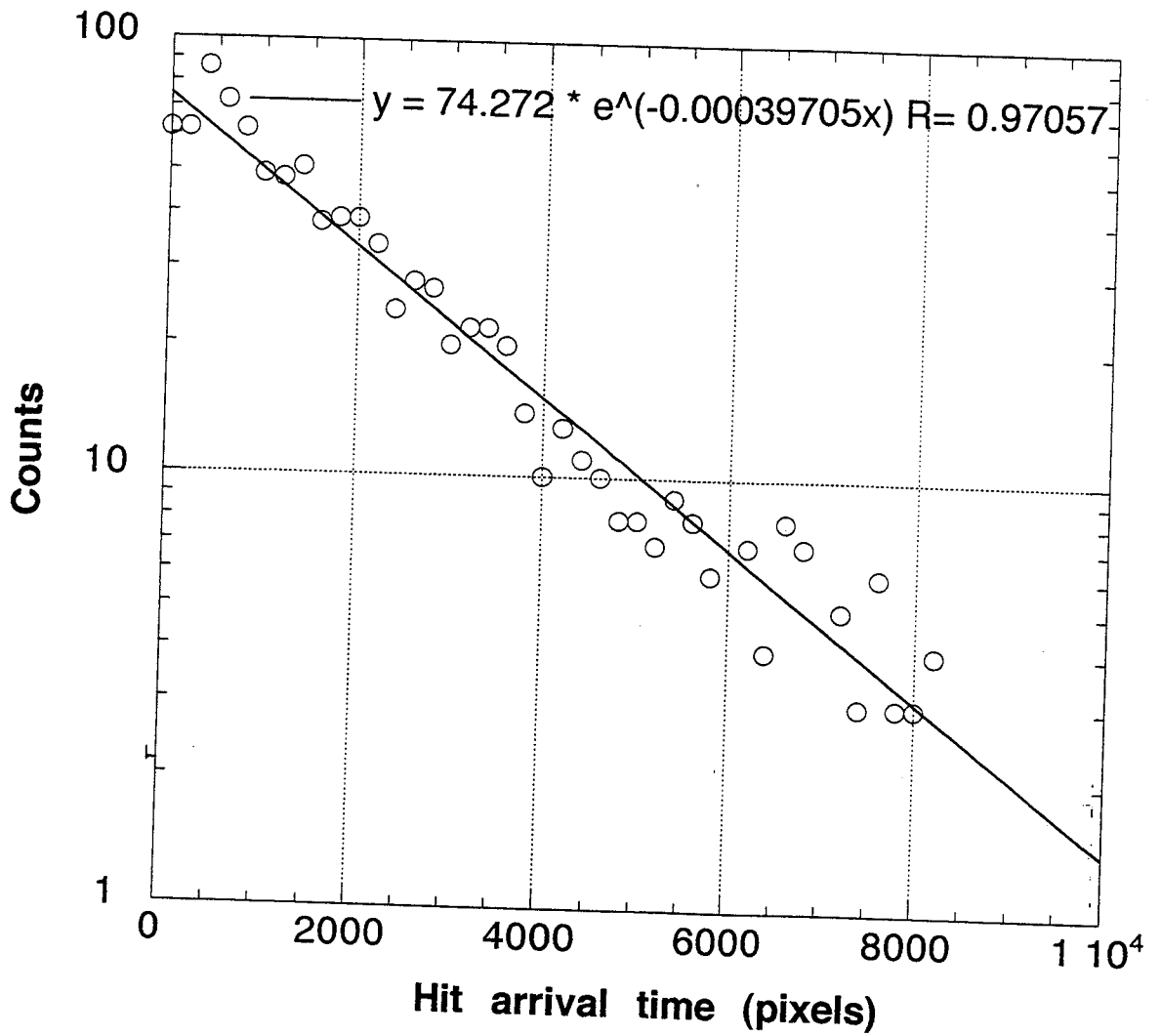
Fig. 4.5 Simulation with 100 hits randomly distributed over a 400 by 600 CCD. Frequency of hit arrival time at CCD output is an exponential distribution.
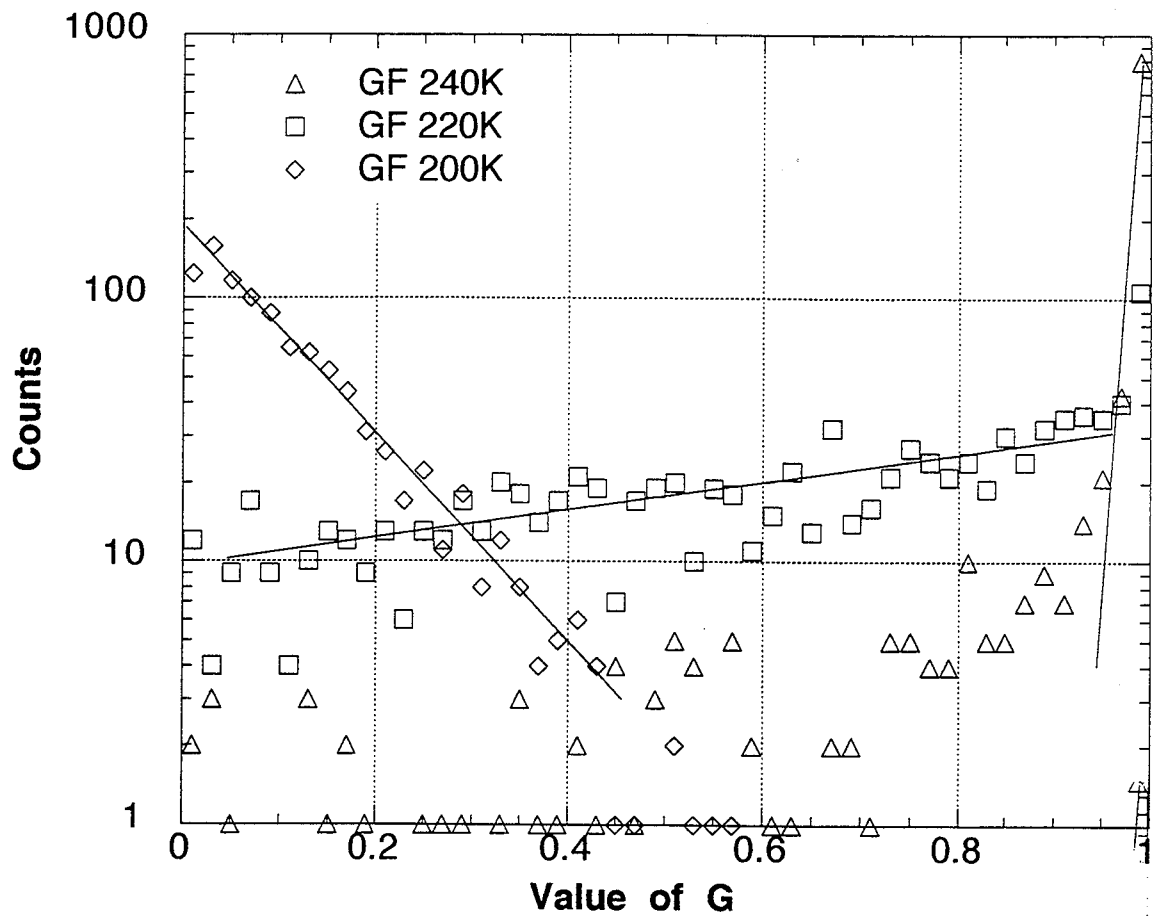
Fig. 4.6 Distribution of G-factor for 100 randomly distributed hits in a 400 by 600 CCD at 200, 220 and 240K.

Simulated SLT at 240K
100 hits in 400 by 600 CCD - 10 frames

Simulated SLT at 220K
100 hits in 400 by 600 CCD - 10 frames

Simulated SLT at 200K
100 hits in 400 by 600 CCD - 10 frames
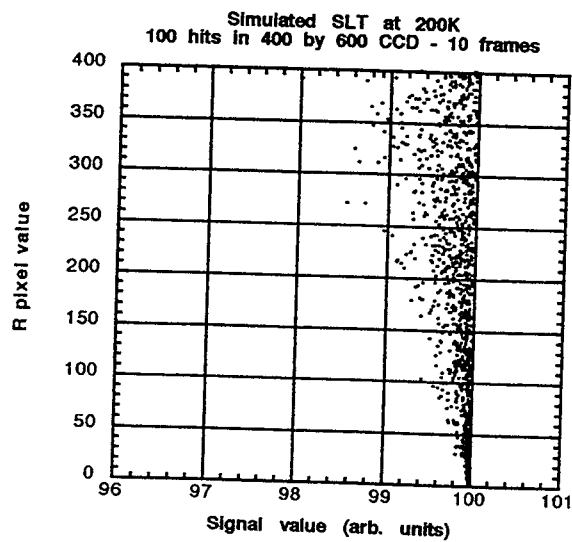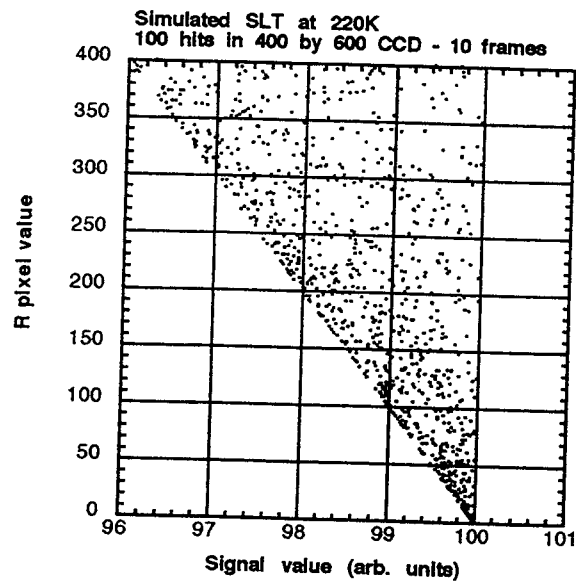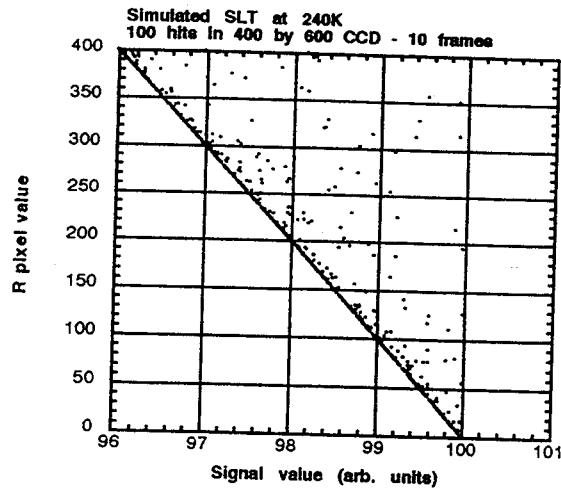
Fig 4.7 Simulations of Stacked Line Traces (SLTs)
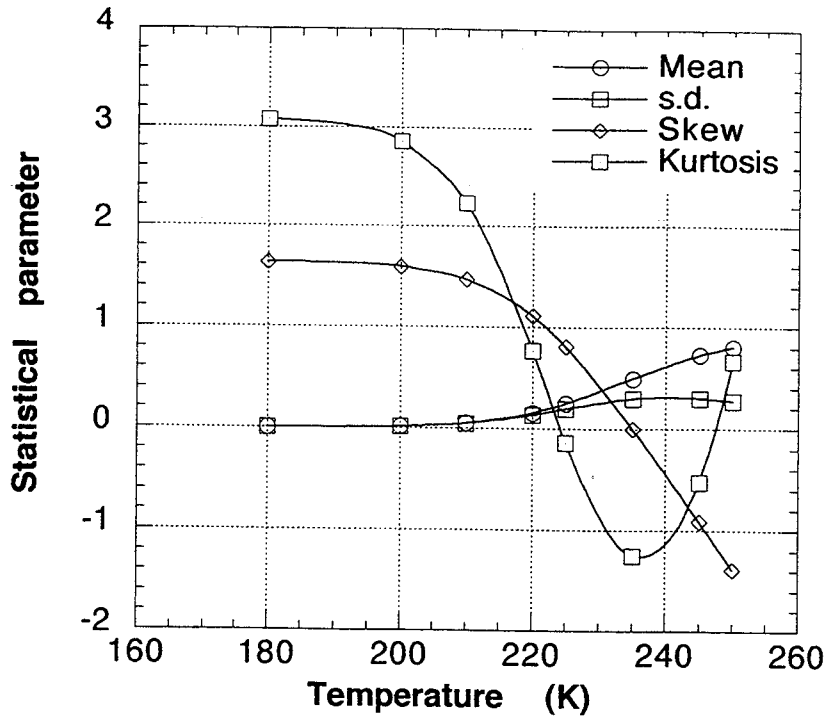
Fig. 4.8a Statistical properties of the G-factor for a mean time between hits of 4.8ms.
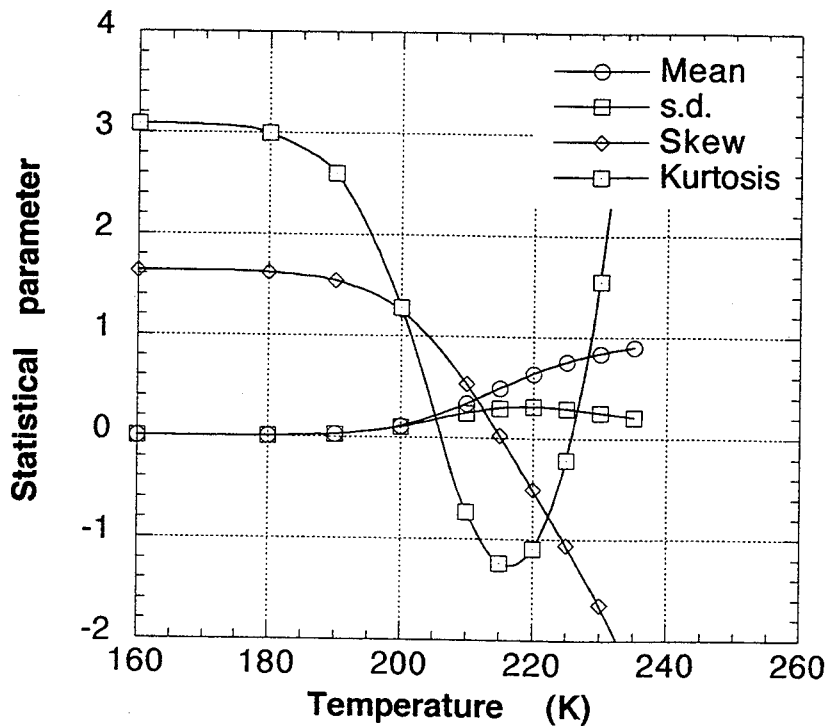
Fig. 4.8b Statistical properties of the G-factor for a mean time between hits of 48ms.
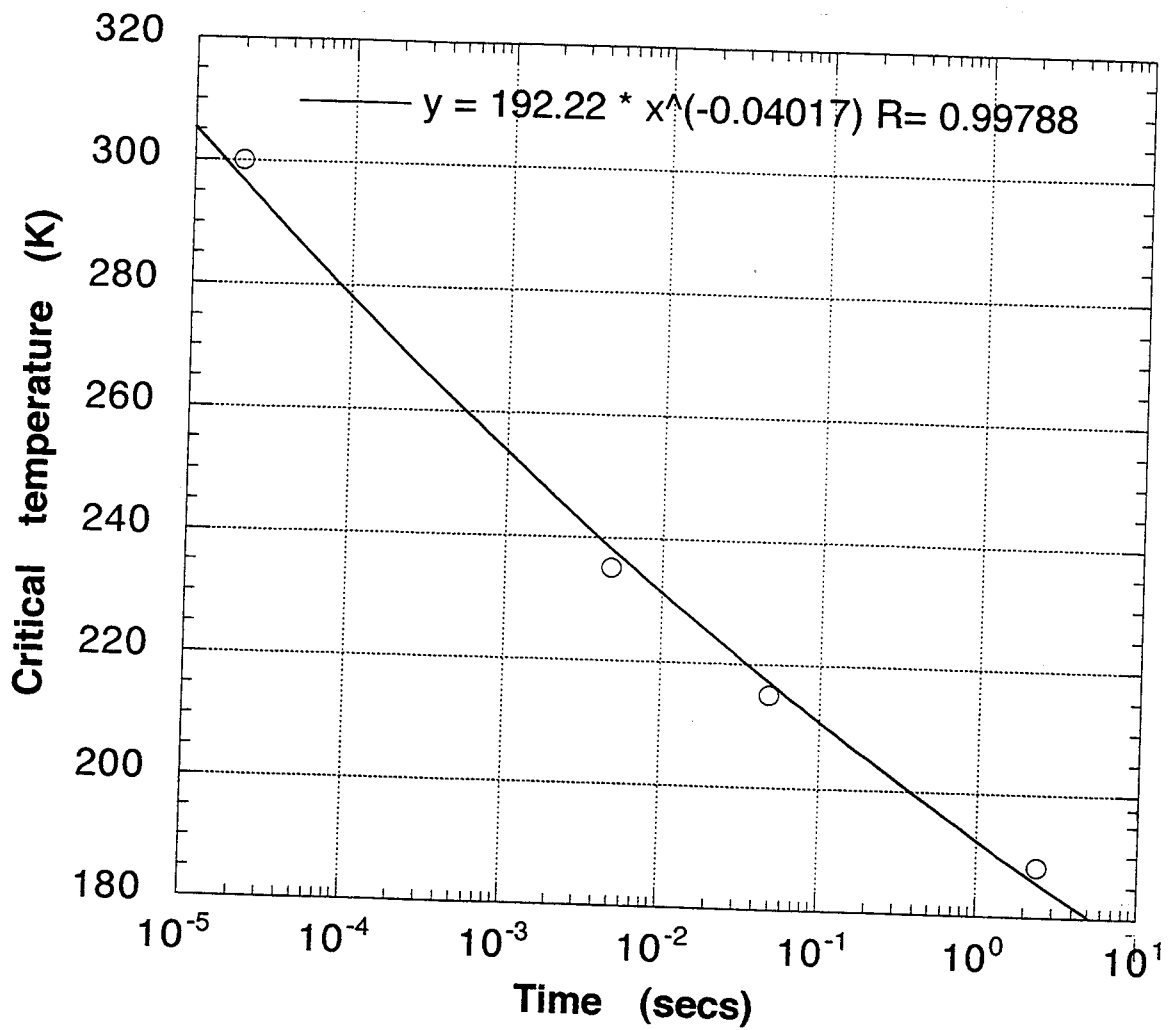
Fig. 4.9 Critical temperature as a function of time between hits. Calculation assumes that the VP defect is the main trapping centre.

SERIAL

PARALLEL

-70 (203K)

-90 (183K)

-110 (163K)

-130 (143K)

-150 (123K)
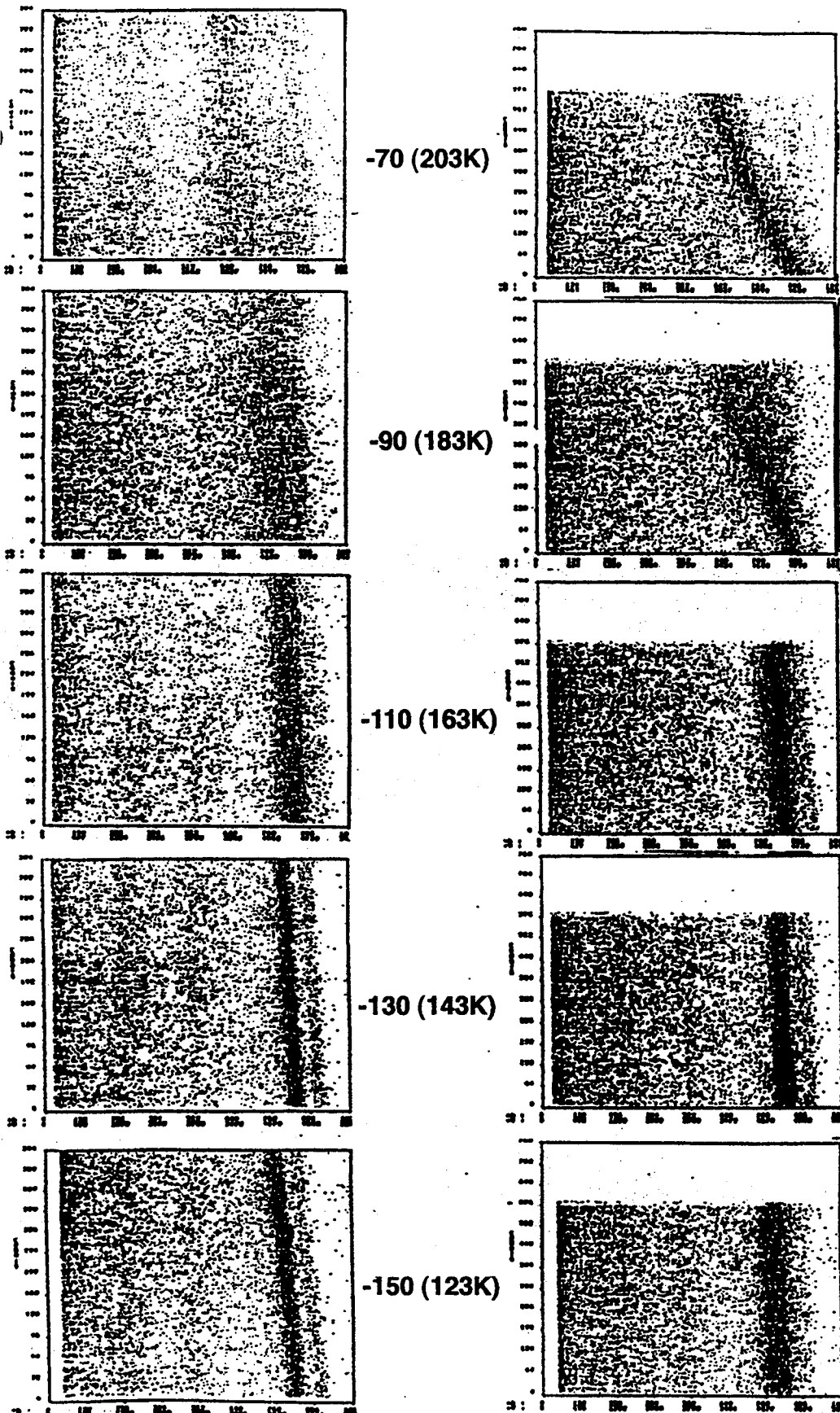
Fig. 4.10 SLT's of proton damaged CCD02 devices
as measured in Work Order 1, for comparison
with foregoing figures.

4.4 X-ray energy dependence of the CTI damage

The CTI is proportional to a factor n_t/n_s, where n_s is the signal density expressed as a volume density of electrons in the CCD potential well. For EEV CCDs the signal density is independent of signal size for signals greater than about 5000 electrons. The signal density falls rapidly for signals below 1000 electrons. Calculations for a standard CCD structure give signal densities of 4E13, 7E13 and 64E13 cm^{-3} for signals of 500, 1000 and 10,000 electrons respectively (Robbins 1992). WO1 data for X-rays of 1.5 KeV (400 electrons) and 4.5 KeV (1200 electrons) show a ratio of 1.5 to 2.0 in CTI values. A factor 2 is expected from calculations given in Robbins (1992). Fig. 4.11 from Robbins 1992 shows how the signal density varies with signal size. Qualitatively the modelling is valid for all CCDs, and the actual values are valid for the CCD02 devices irradiated in this work. As a rule of thumb, the signal density is proportional to signal size for electron packets below 1000 electrons. Above this, it is independent of signal size. Fig. 4.11b shows that the signal density depends on (signal size)$^{0.9}$ using Robbins' calculation. Fig 4.12, also from Robbins 1992, shows this point very clearly. The purpose of using supplementary buried channel (SBC) and Narrow Buried Channel (NBC) technology is to reduce the storage volume and hence increase the signal density for small signals. The WO1 data shows that the NBC technology improves the CTI degradation by a factor 3. No improvement is seen with the SBC technology in WO1 data. This has since been understood by the use of more sophisticated device modelling using EVEREST program. This is described in the next section.

To summarize, for signals above N_c electrons, the CTI will be independent of signal size. Below this value, the CTI will be inversely proportional to the signal size. N_c is typically 1500 electrons for a CCD02 device, which is the size of an Fe 55 x-ray. N_c depends upon the doping concentrations in the device and needs to be determined for a specific CCD design. For elements below iron (eg. Al and Ti) the CTI will be higher and approximately,

$$\text{CTI (X eV)} = \text{CTI (Fe 55)} * (5900 \text{ eV}/ X \text{ eV})$$

..4.12

where X is the energy of the photon. This scaling is for a CTI at a defined hit-rate. Based on the data below this overestimates the CTI at low energy.

This is shown in Fig. 4.13a which shows a clear increase in CTI for the lower elements. The data appears to be better at low energy than one might expect. The data is consistent with a (signal)$^{-0.4}$ dependence. Data from Robbins (Fig. 4.12) is also drawn on Fig. 4.13. It is consistent with a (signal)$^{-0.9}$ dependence, as calclated.

We believe that the reason why the CTI for small signals in the CCD12 (fig. 4.13) is better than expected, is due to the fact that at low signal densities the trapping time constant is longer. If the charge is quickly transferred to the next gate, the "fill factor" - equations 4.1 and 4.6 - is no longer one, and the CTI is lowered. More data is required to confirm this effect. However, such measurements can be found in Robbins '92, and are shown here as Fig. 4.13b. When the time under two of the gates is reduced, the CTI for small signal sizes is reduced.

This result suggests a practical solution for obtaining better CTI with small signals - we recommend the use of asymmetric clocking in which charge is quickly transferred under the gates of two of the three phases - or one of the two phases of a 2-phase CCD etc. In addition, measuring the CTI using the periodic pulse technique (Robbins 92) would be a faster and more efficient way to get the signal size dependence.
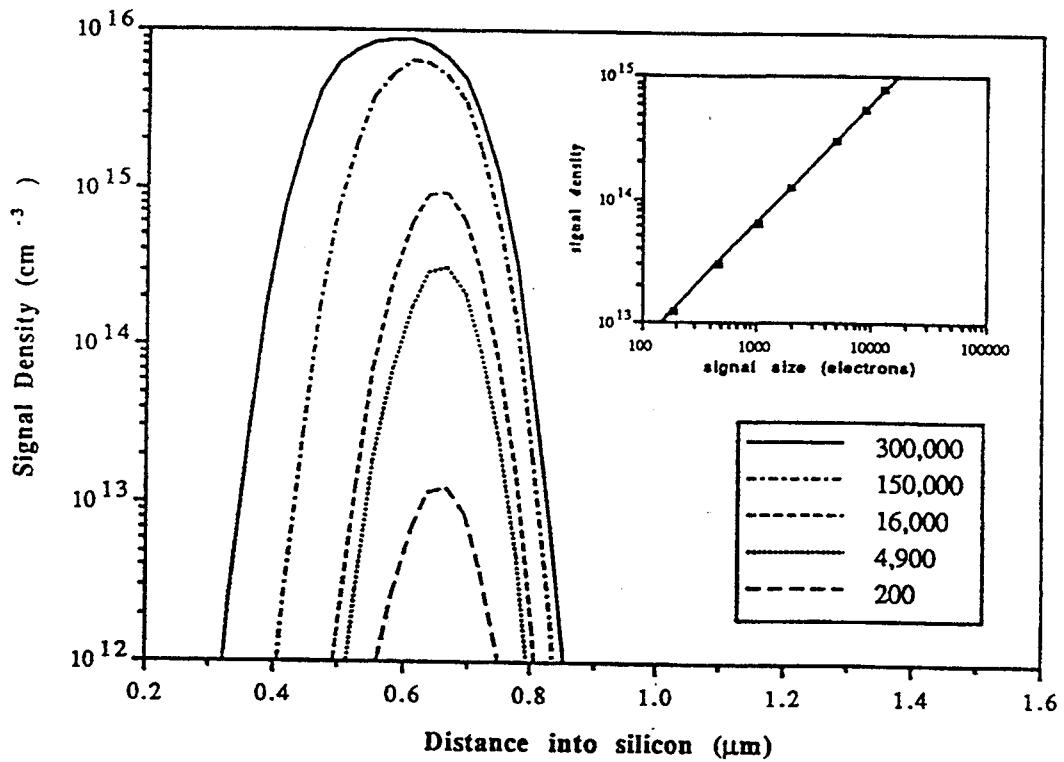
The calculated charge distribution for the UT101 CCD

for various charge packet sizes at 300K. The inset shows the peak

signal density as a function of signal size.

Fig. 4.11a The charge distribution of signal packets of various sizes in the CCD channel. Calculation from Robbins 1992.
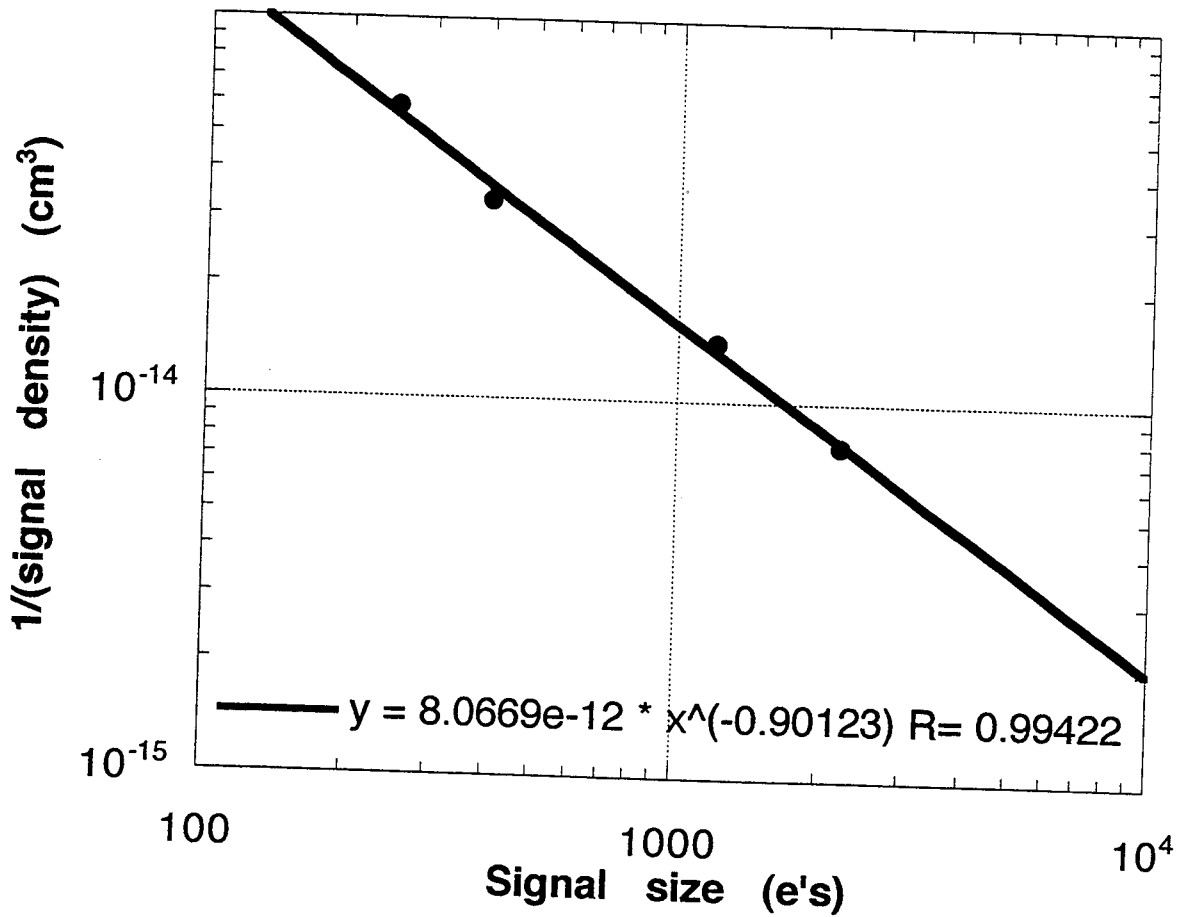
Fig 4.11b Calculated relationship between signal density and signal size from Robbins 1992.

The variation of the CTI as a function of signal size measured at 180K. The device had received 60 krad(Si).
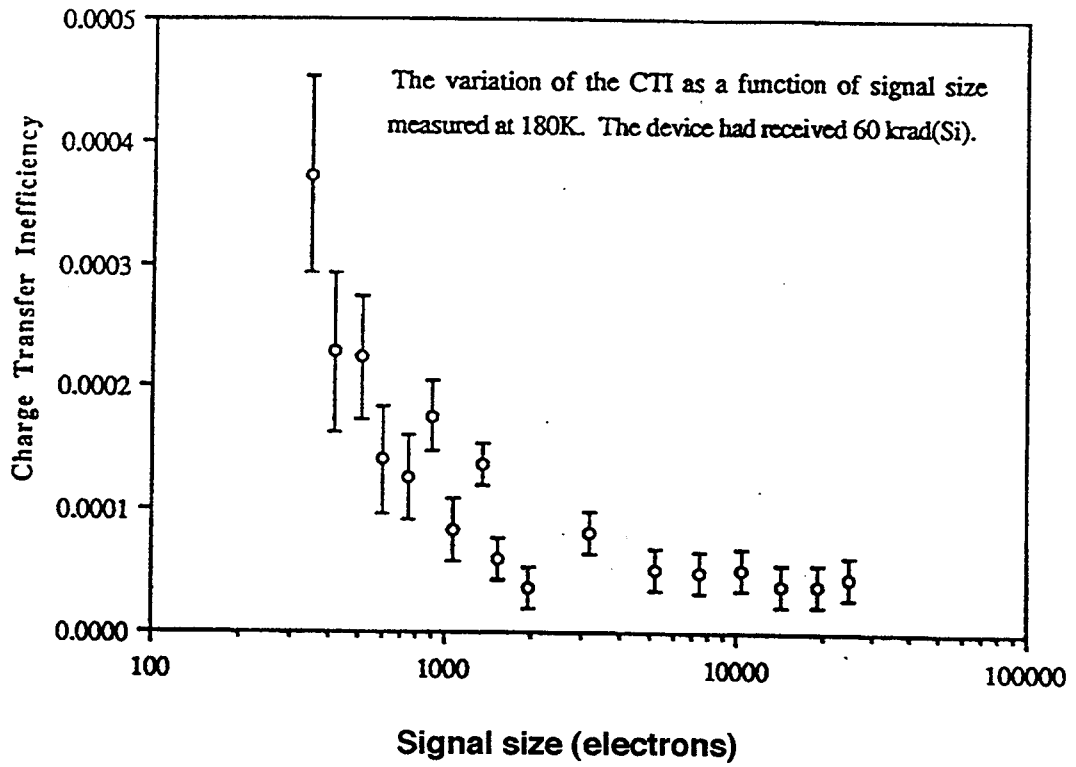
Fig. 4.12 The measured variation of CTI of an EEV CCD01 device irradiated with Sr90 beta particles as a function of signal size at 180K. From Robbins 1992.
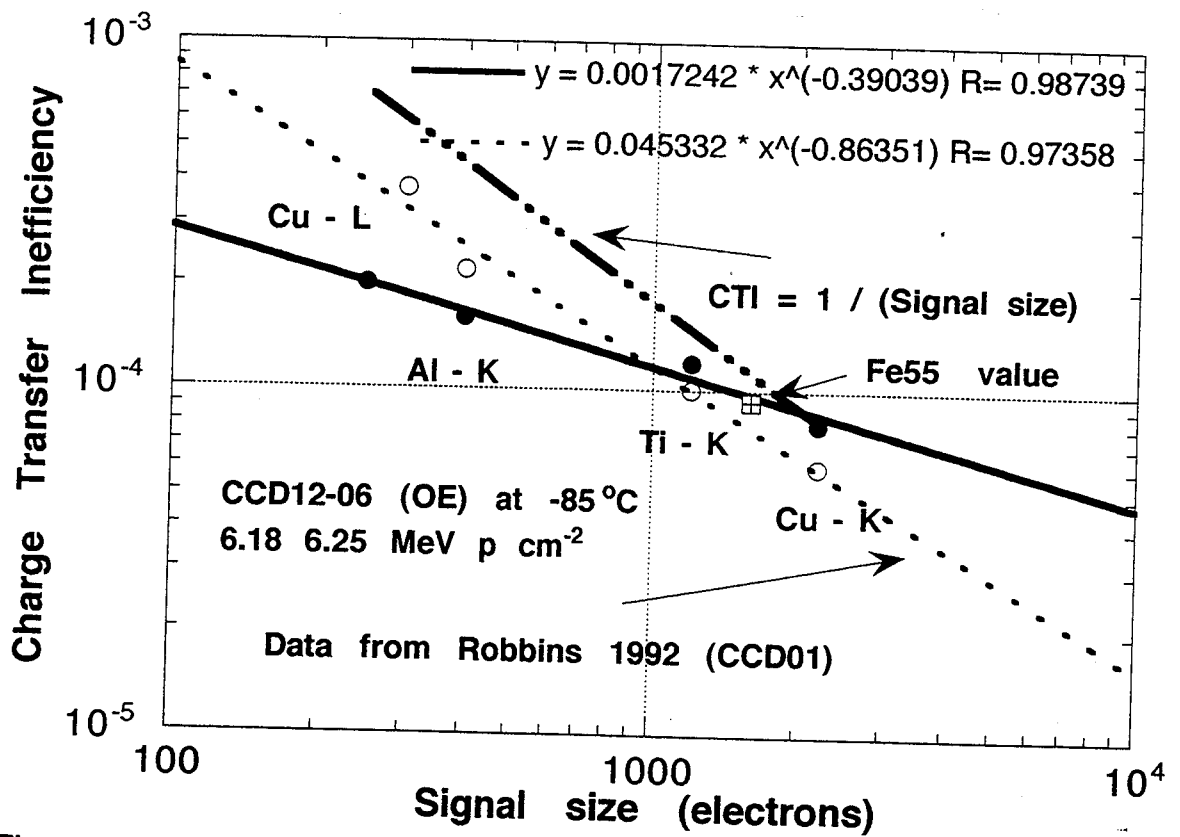
Fig 4.13a Measured CTI versus signal size. Solid curve is a fit to the data. Dashed curves show simple inverse signal dependence and data from Robbins '92 for CCD01
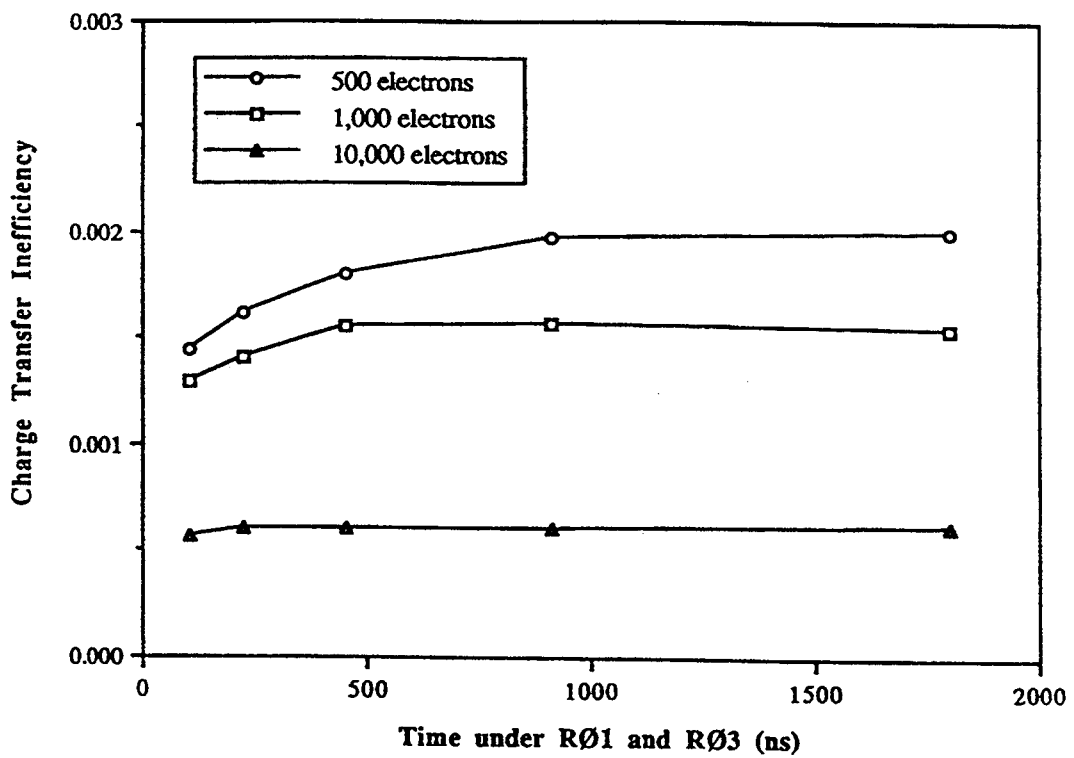
Fig. 4.13b Variation of CTI as a function of the time the signal spends under two of the three phases.
Data from Robbins 1992.

4.5 Modelling of the Buried Channel

In order to understand the relative tolerance of given device structures to bulk damage, a more detailed device simulation was required. Modelling of the pixel structure was performed using the EVEREST 3-dimensional simulation package. This package was developed by a collaboration led by RAL and consists of a device field/potential solver with adaptive mesh generator. The package has been constructed so that device details, in our case pixel size, oxide and electrode details, substrate doping and buried channel doping etc. can be input in a simple manner by building up a block description of the structure. An interative process can then be undertaken to optimise the use of the available mesh points within the structure. The appropriate voltages can then be applied to the pixel structure to provide depletion and the solver routine used to simulate the potentials within the pixel. For the standard device structure, a pixel of 22 μm side was simulated on an epitaxial layer of 20 μm. A gate dielectric of 0.12 μm of oxide was used, together with three contacting electrodes representing the polysilicon gates. For the CCD02 structure these were 7 μm wide with a 0.33 μm gap to represent the inter-phase oxide. The buried channel was defined as an implant representative of the profile used in devices. In the CCD02, the defined buried channel width was 15 μm. In the case of the CCD12 and CCD15 devices, the pixel size was 27 μm, with a defined buried channel width of 25 and 22 μm respectively. In these devices, a supplementary buried channel was also used to improve the charge confinement, of typically 5 μm width. In this report, details of the doping concentrations used in the model cannot be given for commercial reasons. We shall report, however, on the results of the variation of the buried channel width and its impact on CTI in the presence of trapping. The three phase structures were simulated and profiles of the potential distribution taken. Figure 4.14 gives the potential profile below a biased gate into the epitaxial layer. Distance is measured from the epitaxial/substrate boundary. The buried channel can be seen where the potential minimum (for electrons) is located at a distance of about 0.5 μm from the oxide interface. The figure indicates the 80mV region of the potential minimum in which the charge is stored; it represents the 5kT boundary for the charge packet. As can be seen, this indicates a charge storage depth of 0.5 μm. Figure 4.15 gives the potential profile across the buried channel in one of the simulations at the depth corresponding to the potential minimum (Fig. 4.14). This simulation was for a 15 μm wide buried channel.The 80 mV boundary indicates that across the channel the active charge confinement width is narrower than the defined channel width. Figures 4.16 and 4.17 indicate the potential profiles across a pixel with a 4 μm supplementary buried channel (SBC). In this case, the charge confinement is slightly broader than the defined SBC width. It is believed, that in the case of a simple buried channel, the fringing fields in the silicon between the BC and non-BC silicon act to reduce the effective width of the confinement channel. However, in the case where an additional SBC has been added, the presence of BC around the SBC supports the field and acts to broaden the confinement channel beyond the definition of the SBC. A summary of the results follows:

Defined Width (mm)	Storage Width (mm)	Impact
15 (BC)	9.3	Narrower
4 (SBC)	4.5	Broader
2 (SBC)	2.6	Broader

The table indicates that, irrespective of the current tolerance of the CCDs to particle damage, an improvement of a factor of 1.7 may be achieved through the use of a narrower (2 μm) supplementary channel. For applications involving small signals (<5000 electrons) as is the case in XMM, computer simulations may be used to provide a simple analytical estimate of the hardness of a particular CCD. The depth of charge confinement can be assumed to be fixed as 0.5 μm. Thus the difference in hardness between CCDs may be simplified to the difference between storage surface area in the pixels. Figures 4.18 (a-d) give schematics of the pixel storage areas in relation to the clock phases and the buried channels. The charge storage regions are indicated by the shaded areas. The charge is always constrained to less than the electrode dimension due to inter-electrode fringing fields. Thus if a gate width of 7 μm is used, the storage width is typically 1 μm less on each side, or 5 μm wide. Since charge transfer

occurs at the 50% crossover point, the charge spends very little time in the region between electrodes and trapping in this period can be neglected. Storage widths across the buried channel are similar to those detailed in the table above. We reiterate that charge confinement in a buried channel is less than the defined width, whilst in the SBC it is slightly more than the defined width. In the case of the CCD12 (OE) - open-electrode devices- an area on either side of the long supplementary buried channel (SBC) has been implanted in order to "pin" or confine the charge within the as-drawn SBC boundary. The relative tolerance of these devices to irradiation induced bulk defects may be estimated from these storage surface areas . They are given in the table below together with averaged CTI results at -90 °C from this work, normalised to a fluence of $1E9/cm^2$ (10MeV equiv.) protons. To minimise the scale errors , only data taken from devices irradiated to >2E8/cm2 (10 MeV equiv.) were used.

Table 4.2 Hardness factors for various SBC designs

Type	Phase 1	Phase 2	Phase 3	Confinement Area (μm^2)	Predicted Tolerance	Parallel CTI $1E9/cm^2$	Measured Hardness
CCD02	5x9	5x9	5x9	135	N/A	313 (67)	N/A
CCD15	3x5.5	3x5.5	15x5.5	115	0.83	266 (26)	0.85
CCD12(JX)	3x5.5	3x5.5	15x5.5	115	0.83	251 (33)	0.81
CCD12(OE)	3x5.5	3x5.5	15x3	78	0.56	48 (15)	0.47

Notes:

a) CTI values in brackets are initial values.
b) JX means the JETX version of the CCD12
c) OE means "open electrode"

In early work using supplementary channels the CTI improvement was expected to scale as the defined channel width. This work now indicates a much more subtle hardening factor, which also takes account of device pixel size (which affects transfer length through the pixel). The predicted results based on the simple analytical approach outlined above are in good agreement with the averaged, measured hardness factors (defined as CTI(CCD##)/CTI(CCD02)) derived from the measurements of the devices in this work. The relative lack of improvement in the CCD12(JET-X) and CCD15 devices compared to the CCD02 was initially a surprise. It arose from an early lack of understanding of the charge transport in the CCD02, which was in fact more radiation tolerant than anticipated. The result of the CCD12(OE) indicates that a more effective charge confinement approach might be to provide a shallow surface-pinning implant along either side of the SBC implant, giving rise to an effective channel width of around 2μm. This latter option must be balanced against the reduction in depletion depth when using a pinning implant, and the possible risk of potential pockets in the charge flow path. As mentioned earlier, additional hardening might be possible through the use of a 2 μm SBC which would produce, for example, a hardness factor of 0.4 in the CCD15. It should be pointed out, however, that errors in the potential profile modelling will become more significant at these dimensions, and that implant errors can lead to potential pockets.

In conclusion, it has been shown that a detailed 3-D simulation of the pixel can be used to estimate the CTI tolerance of the CCD. This approach is not available to all CCD users however, and an alternative approach to estimating the device tolerance has been demonstrated which uses the results of the more detailed simulation to derive rules of thumb based on simple surface area calculations. The results of this appraoch are in good agreement with measured CTI values.
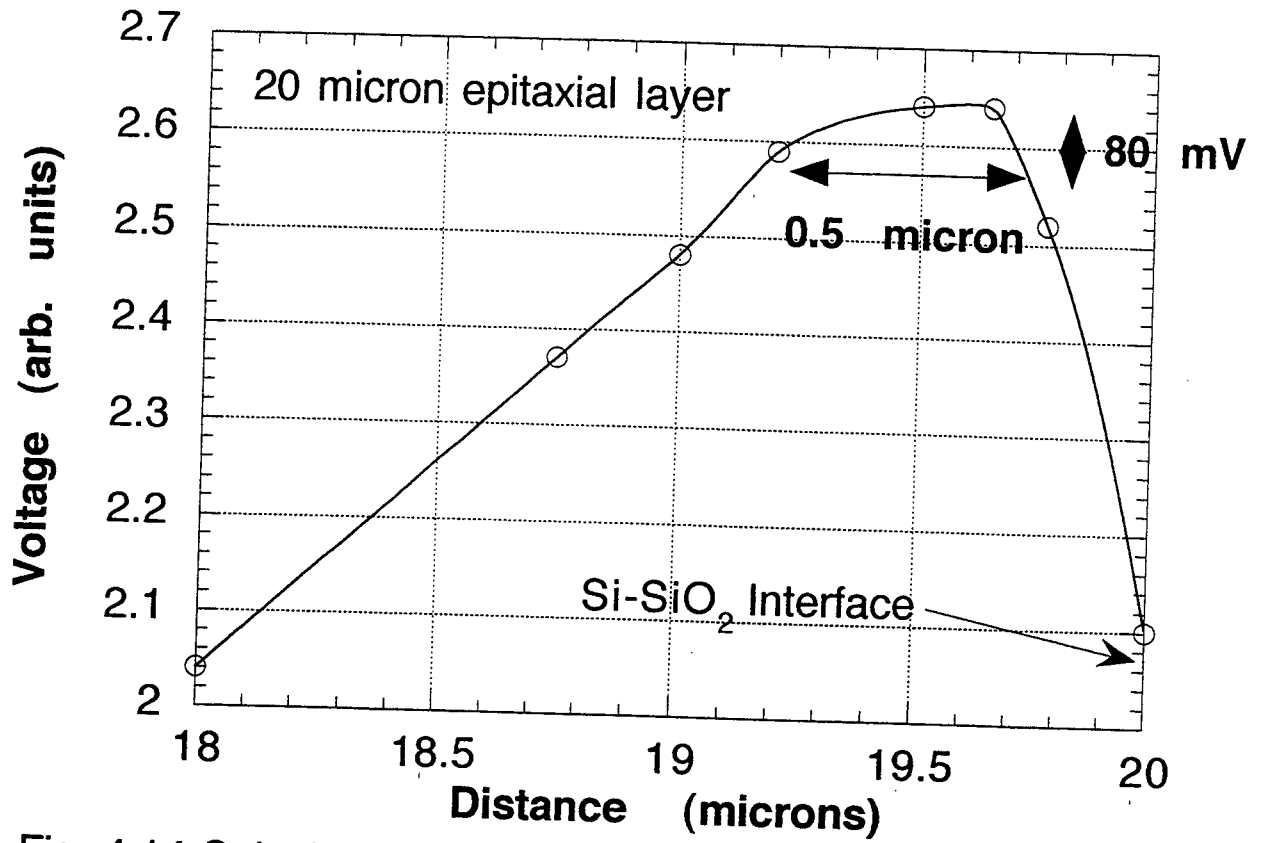
Fig. 4.14 Calculation using the Everest programme of the potential profile in the buried channel region of an EEV device
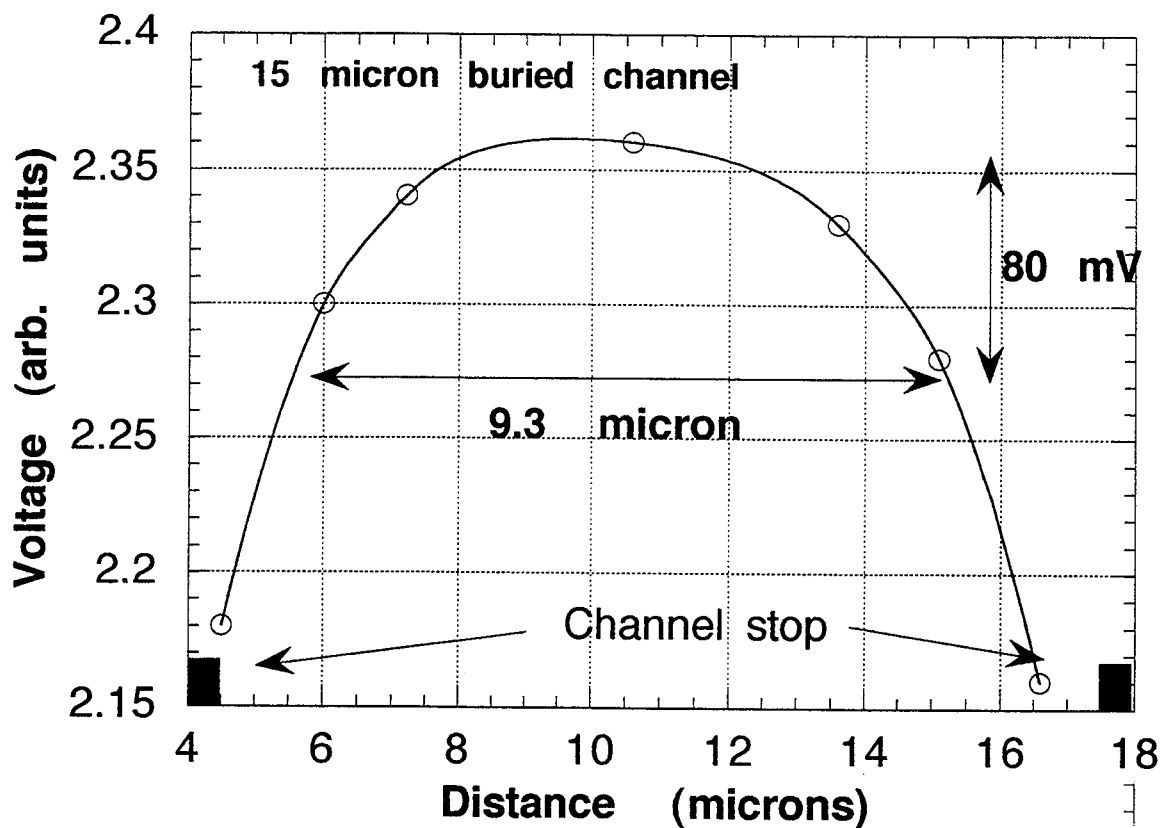
Fig. 4.15 Calculation using the Everest programme of the potential profile in a buried channel; section across the channel stops, parallel to the surface.
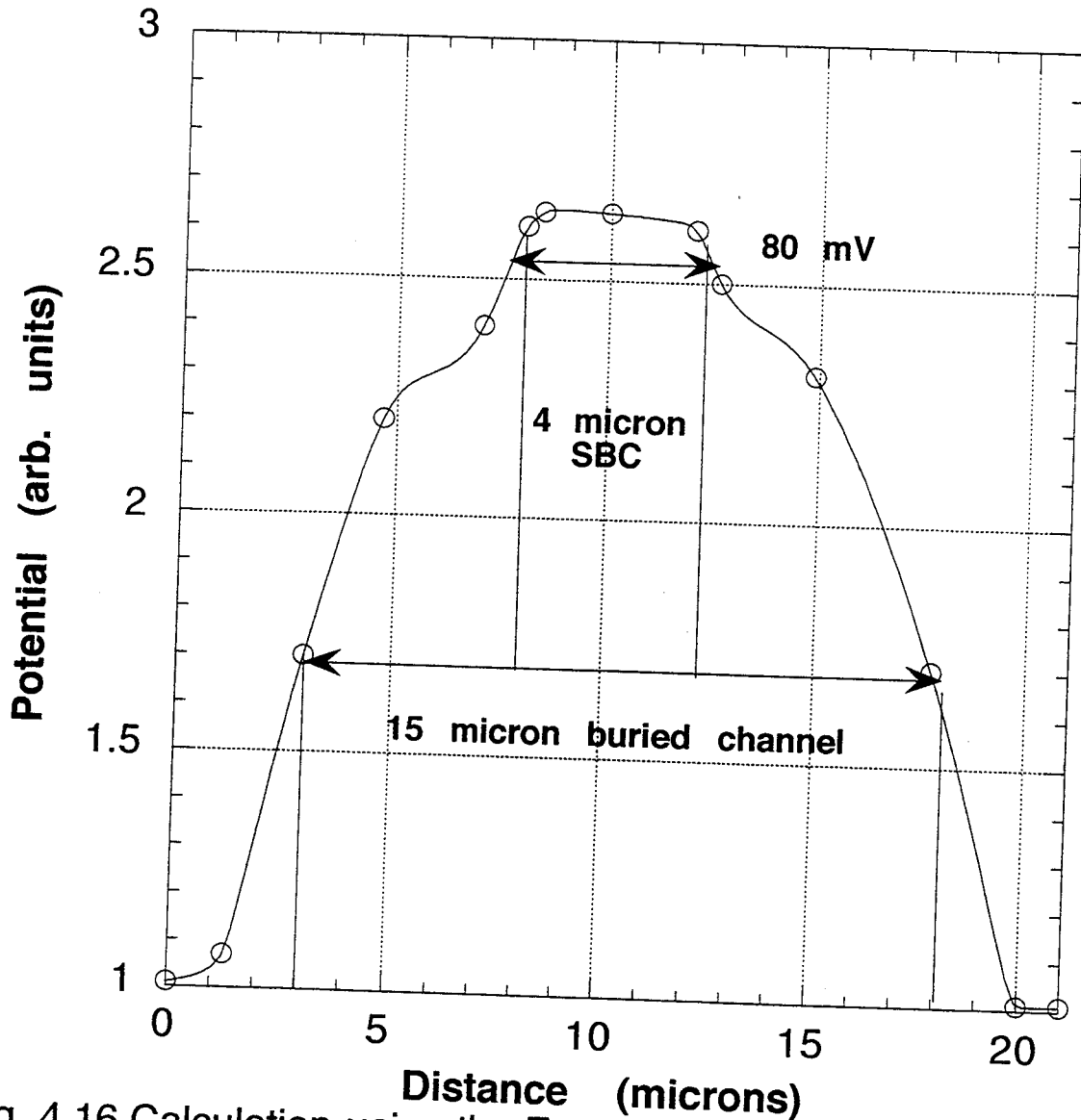
Fig. 4.16 Calculation using the Everest programme of the potential profile for the buried channel region; section parallel to the surface
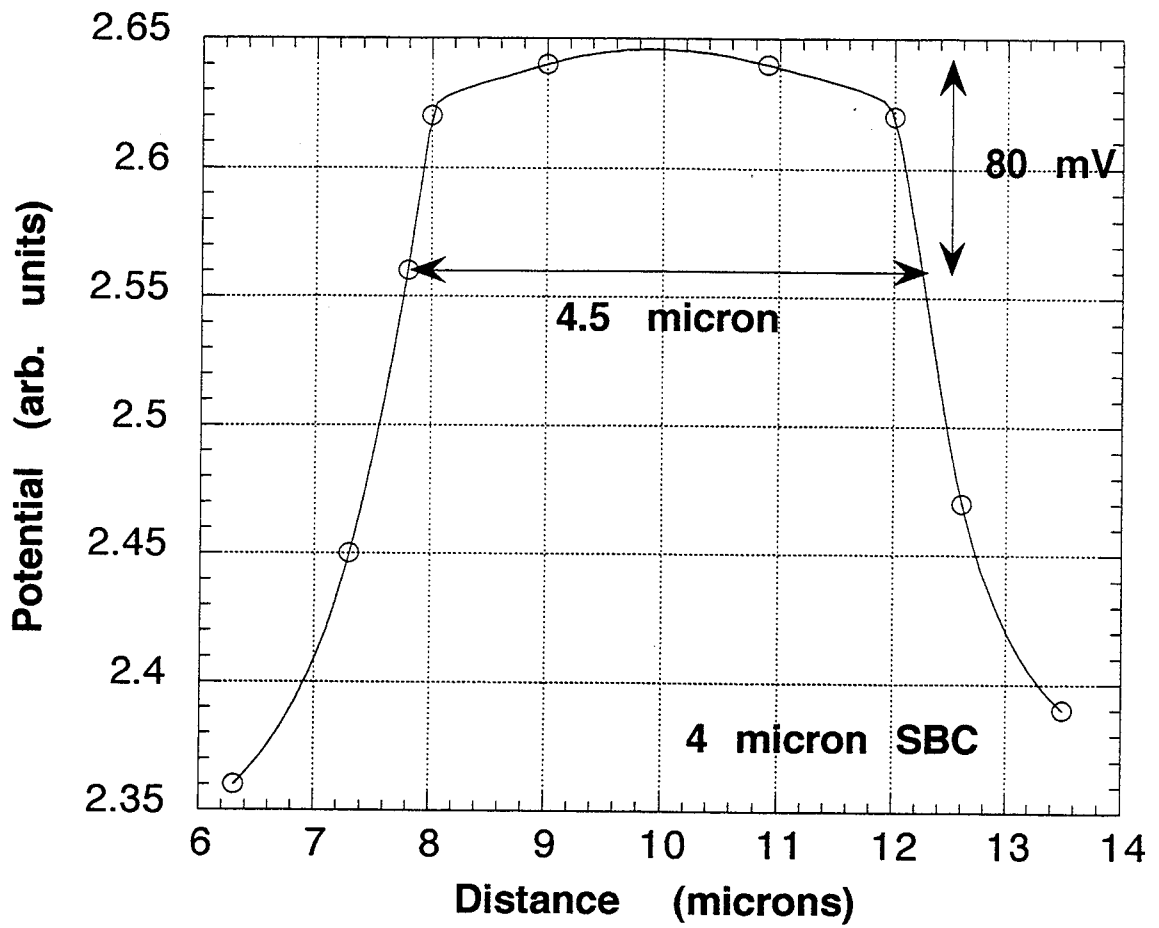
Fig. 4.17 As for Fig. 4.16, expanded view of SBC

(a)

CCD02

|←————————————→|

22 MICRONS

(b)

CCD15

←→

SBC

(c)

CCD12(JET-X)

←————————————→

Buried Channel

(d)

CCD12(OE)
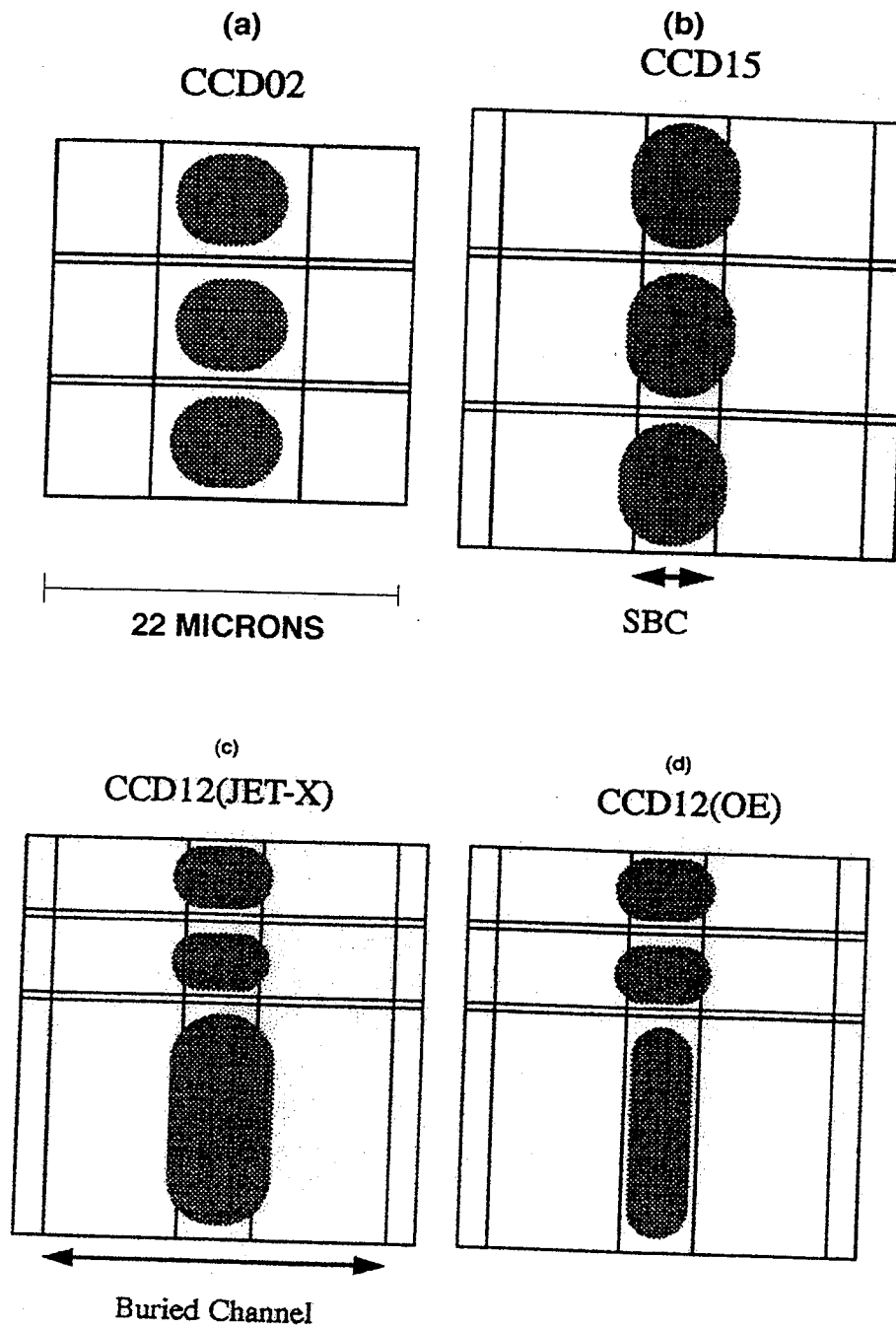
Fig 4.18 Scale drawing indicating spatial extent of charge packet in various CCDs. Gate, channel and supplementary channel dimensions are shown.

4.6 CTI damage constants - experimental

This section gives an overview of all the CTI results. Figs 4.19 to 4.21 give the parallel CTI as a function of fluence at three temperatures. Figs 4.22 to 4.24 show the corresponding serial register data.

In figures 4.19 to 4.21, linear fits are drawn for the CCD15 and CCD12(OE). The dependence of CTI on fluence fits reasonably, with a moderate spread. The results for the one CCD on bulk Float-Zone material (CCD12-07) are interesting since they tend to lie below the other results for CCDs on epitaxial silicon. For the CCD02s, only a single, high fluence was used, and there is a very large spread of results. Thus, it is not justified to draw a similar fitting curve for this type. It is still clear that, except for T = -110 $^{\circ}$C, the CTI damage is much higher on average (see also Table 4.2) than the other devices. From the lines drawn through the data, we now extract a damage constant, DC. We define this as

$$DC = \Delta CTI/ \text{(10 MeV equiv. fluence)} \hspace{3cm} ...4.13$$

The constants are listed in Tables 4.3 and 4.4 with the reservations (a) that the CCD02 results have a large variance, as discussed and (b) that the serial damage factors are similarly widely spread.

Table 4.3: Parallel CTI Damage Constant. The readout conditions are given in Table 1.1

Device Type	-70 $^{\circ}$C (10^{-13} cm^{-2})	-90 $^{\circ}$C (10^{-13}cm^{-2})	-110 $^{\circ}$C (10^{-13} cm^{-2})
CCD15	2.7	2.5	1.1
CCD02	3.7	2.7	1.1
CCD12 (OE)	1.7	1.3	0.53
CCD12(OE Bulk)	1.7	0.27	0.13
CCD12(JETX)	2.7	2.5	1.1

Table 4.4: Serial CTI Damage Constant. The readout conditions are given in Table 1.1

Device Type	-70 $^{\circ}$C (10^{-13} cm^{-2})	-90 $^{\circ}$C (10^{-13} cm^{-2})	-110 $^{\circ}$C (10^{-13} cm^{-2})
CCD15	< 0.06	0.2	0.3
CCD02	1.0	0.8	0.7
CCD12 (OE)	1.0	<0.2	0.3
CCD12(OE Bulk)	0.7	0.4	<0.06
CCD12(JETX)	1.0	0.8	0.3

Some comments concerning these results:-

a) The reason why the CCD12(JETX) and CCD15 devices are not as tolerant as the CCD12(OE) is explained in section 4.5.

b) From the single test on a bulk Float Zone CCD, we surmise that this material exhibits reduced damage . We believe this may be a real effect and be related to low introduction rates for the E2 defect.(see Section 4.2) The identity of this defect is not known. Some speculation on the nature of the E2 defect is given in Section 5.2.

c) The statistical spread on the data is generally small except for the CCD02 devices. Since the ten CCD02 chips were taken from the same wafer, the spread was expected to be small. The large spread was a surprise and figures in our discussions and recommendations.

The relationship between the CTI and FWHM is shown in Figs 4.25a and 4.25b. There is a clear correlation between the parallel CTI and FWHM. There is no evidence of a correlation with the serial CTI. Remember that the CCD02 devices received a similar dose. The clear correlation between parallel CTI and FWHM shows that the data is self-consistent, even if the reason for the wide spread in CTI values of the CCD02 devices is not understood.

It is possible to estimate the the damage constant using the defect kinetics model discussed later. In high resistivity diodes, the VO centre is created by neutron irradiation at a rate of about 4 cm^{-1}. In such material the phosphorus concentration is much lower than the oxygen content and vacancies are "gettered" by the oxygen. In the CCD buried channel the opposite is true because the phosphorus concentration is high. It is thus reasonable to assume that the introduction rate for the VP centre in a CCD under 1 MeV neutron irradiation is about 4 cm^{-1}. Using NIEL, one can then estimate that 1E9 10 MeV protons will create about 1.5E10 cm^{-3} VP centres. Thus the worst case CTI for a 1000 electron signal in a CCD02 device would be:-

$$CTI_{max} = 3 \text{ times } (1.5E10/7E13) = 2E-4$$

This is a damage factor of 2.0E-13 . This is in good agreement with data in Table 4.3.

4.7 CTI Correction

CTI correction has been applied to a section of the most damaged CCD12 chip, no.6. The section having received 6.18E8 cm^{-2} equiv. 10 MeV protons was studied. This level of damage is approximately twice the value to be expected by the EPIC CCDs on XMM. Software was written in Fortran on a Sparc station to convert the files recorded on the Archimedes front-end computer into a photon list file. This file lists Ti-K photon events. Pixel associations were performed and the photon list file contained ;

an array of X-positions on the CCD
an array of Y-positions on the CCD
an array of event energy - derived from the charge generated
an array of number of pixels in the event.

X-ray event analysis packages at Leicester were then used to manipulate the data and to display the results. Three kinds of plots were used to visualise the data. Firstly the stacked line trace (SLT) which is a position/energy dispersion of the events. This is particularly useful at depicting gross CTI effects and also non-well-behaved CTI behaviour (e.g. when the temperature/flux rate leads to trapping/de-trapping anomalies in the data). An example of such an SLT is shown in Fig. 4.26.

To effect a test of CTI correction, subroutines in the analysis language were written to step through a range of serial and parallel CTI values. For each of the 10 parallel and 4 serial CTI values, the photon energy was corrected, in this case assuming a linear dependence upon position. From the SLTs (cf. Fig. 4.26), the line produced follows the centre of the array of points. That is, to a first approximation, the assumption of a linear dependence of pulse height on position is correct. The CTI was then corrected according to the equation:

Correction =   ((1- xposition * CTIs) * (1- yposition * CTIp))$^{-1}$

For each CTI combination, the full width at half maximum (FWHM) was then evaluated for the X-ray line by choosing an pulse height region of interest which spanned the line, and evaluating the variance of the spectrum (assuming a Gaussian profile) using the equation;

FWHM = 2.35 * Calibration (eV/DN) * SQRT (mean squared - mean of squares)

where DN is the digital number reprenting pulse height. A graph was then formed of the FWHM vs. parallel CTI for the different serial CTI values (see fig. 4.27). For each of the minimum FWHM values after correction, the pulse height spectrum was plotted before and after correction. Figs. 4.28 and 4.29 show the spectra for temperatures of -90 and -120 °C. The best fit serial and parallel CTI values giving minimum FWHM values were:-

Temp	CTIs	CTIp
-70	8E-5	1.7E-4
-90	8E-5	1.5E-4
-110	5E-5	7E-5
-120	3E-5	2E-5

Returning to fig. 4.27 which shows the FWHM versus the parallel CTI, one sees a broad minimum corresponding to the optimium correction factor. Anomalies in the curves do arise however, due to the fixed nature of the pulse height regions of interest (ROI). This can lead to errors when the corrected energy value of the line falls outside the pulse height ROI. The values of FWHM should not be taken as being strictly correct, again due to the use of a fixed pulse height ROI and the fitting procedure. This technique is adequate as intended, i.e. as a figure of merit of the goodness of the CTI correction.

The figure of pulse height spectrum taken at -120 °C shows that the energy resolution can be improved even after CTI reduction brought about by cooling. In this case the strict FWHM is 150eV. Again it should be remembered that this dose level is a factor 2 higher than the mission fluence. Note that the FWHM does not recover to the pre-irradiation value. This means that there are other statistical fluctuations in the CTI which this algorithm cannot eliminate.

This correction algorithm has been applied to data with a known, fixed X-ray energy -Ti 4.5 KeV. More work is required to see if this technique can be applied to CCD data containing several x-ray lines. One should also note the comments on the signal size dependence of the CTI in Section 4.4.

4.8 Improvement of the CTI using charge injection

One of the most important methods for reducing electrical effects arising from deep traps in CCDs is the use of a low temperature to freeze carriers into the traps, thereby reducing the density of empty traps or lowering the "G-factor". In addition, by supplying background charge, the traps can be kept filled and reduce charge loss from the signal. This could be achieved using background photons or electrical injection. The EPIC flight design possesses a charge input structure at the top of the image array. This allows a controlled quantity of charge to be input to the first row of the image at each frame transfer period. It is intended that a charge input "pulse" will occur at the beginning of every frame readout. This "bright row" of charge will then be swept through the image and storage array. The charge level in each pixel of the "bright" row will be 1000 to 3000 electrons. Furthermore, the hit rate will be exactly timed to 1 hit/column/integration time (or 2.4s in the case of EPIC). This hit rate by far exceeds the majority of X-ray signals arising from astronomical objects. The charge loss during the trap filling will therefore be from the electrical charge injected signal rather than the scientific X-ray signal. The pinning of the G-factor to a given operating temperature/frame time will also lead to less statistical fluctuation on the CTI which will aid CTI correction.

To test out this concept and confirm the approach, an irradiated CCD02 from WO1 was operated in frame transfer mode, similar to the EPIC operating mode. The CCD02 possesses an anti-blooming (AB) gate and anti-blooming diode at the top of the image array. In conventional imagers with the anti-blooming option, these connect to implants in the image section which drain excess charge away. However, in the scientific imagers under test, the column implants were not present. By applying the appropriate bias to the AB Drain (in this case around 16V) and by linking the AB Gate to the frame synchronisation pulse, a row of charge could be flooded

into the top row of the image, in a similar manner to that described above. The AB gate gave a signal input of between 2-5k electrons for a 0-5V transition. The input charge was not sensitive to pulse duration but a 10 microsecond pulse was applied.

Fe X-rays were used to evaluate both FWHM and parallel CTI, and the operating temperature was varied between -60°C and -120°C to evaluate this method. FWHM and CTI recordings were made with and without the charge injection in operation. An AB gate transition between 0-2V prevented injection. Figures 4.30 and 4.31 give the results for the Fe FWHM and CTI as a function of temperature with and without charge injection. The dashed line in each case represents the performance in the shielded side of the device which had not received an irradiation.

As can be seen from Figures 4.30 and 4.31, the temperature dependence profiles are similar in form with and without charge injection. However there is a temperature shift in the curves. This may be explained by considering the curve without charge filling operation as being the worst case, where the low-flux X-ray signal provides the signal to fill the traps. With charge filling in operation, the regular wave of charge in every column, every 2 seconds, is equivalent to operating with a higher X-ray flux which we have shown earlier to be beneficial. In this case however, an electrical stimulation is providing the signal for trap filling. The overall effect is to shift the carrier freezeout 10°C higher in temperature.

Clearly the method is successful. However, this test represents only a trial. The full effect will have to be studied on the EPIC CCD22 device when available, where the exact improvement will have to be tested for this device at the correct operating frequency. Effects such as uniformity of charge input across the array will have to be addressed, and the possibility of "dark" pixels in the bright row. In addition, in trial studies, at key temperatures where the emission time of some trap species was of the order of the row transistion time, a bright decay band could be seen after the bright row - similar to an extended pixel edge response. This effect was most apparent at -90°C where the 0.3eV traps were releasing charge on the timescale of tens of microseconds. This problem will have to be studied in more detail together with baseline correction code which will be required in the flight electronics.

The above experiment was a preliminary but useful demonstration of the technique which not only acts as a "charge saver" for the X-ray signal, but also acts to alleviate the cooling requirements on the CCD cameras by about 10°C.

Comparison of different devices at -70°C
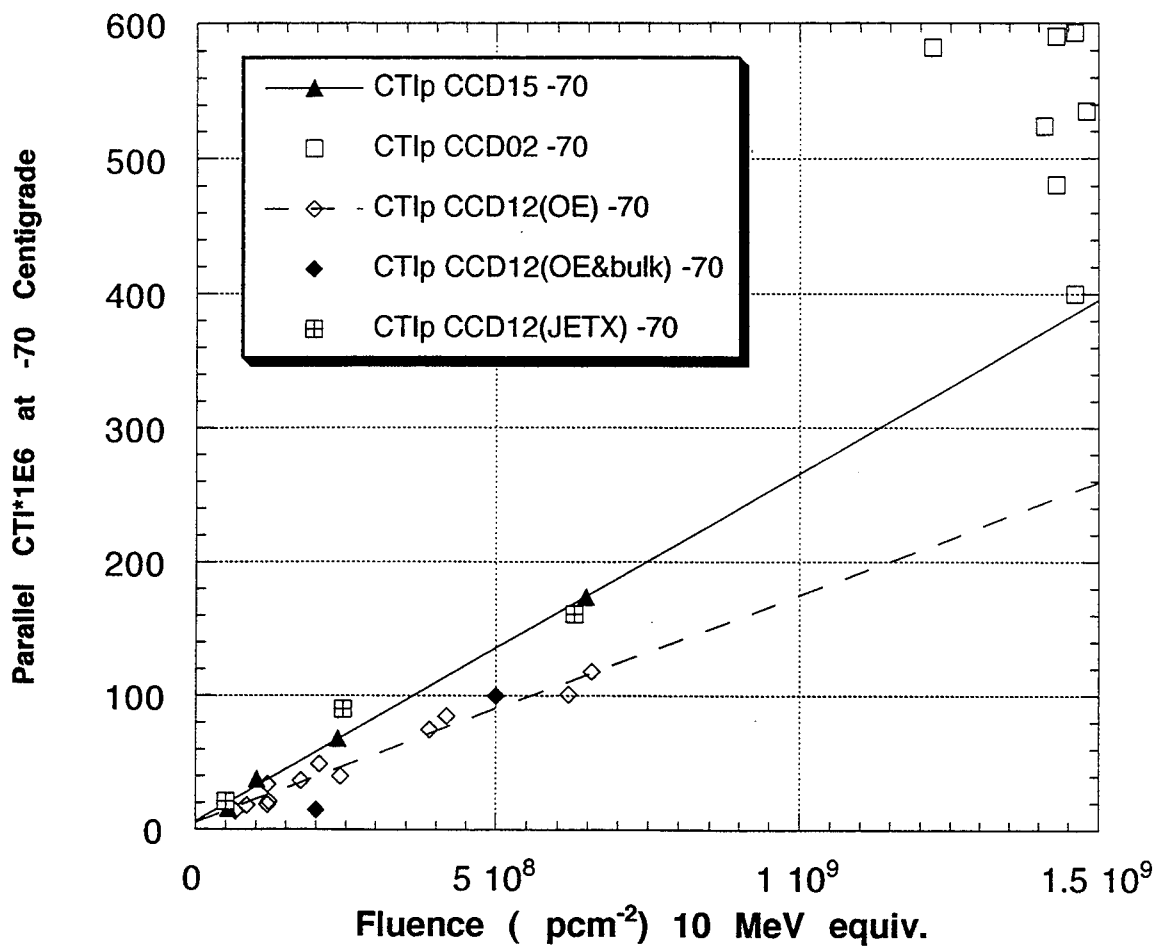
Fig. 4.19 Growth of parallel CTI at -70 °C with proton fluence in WO2 experiments. 6.25 MeV used, converted to equiv. 10 Mev fluence.

Comparison of devices at -90 °C
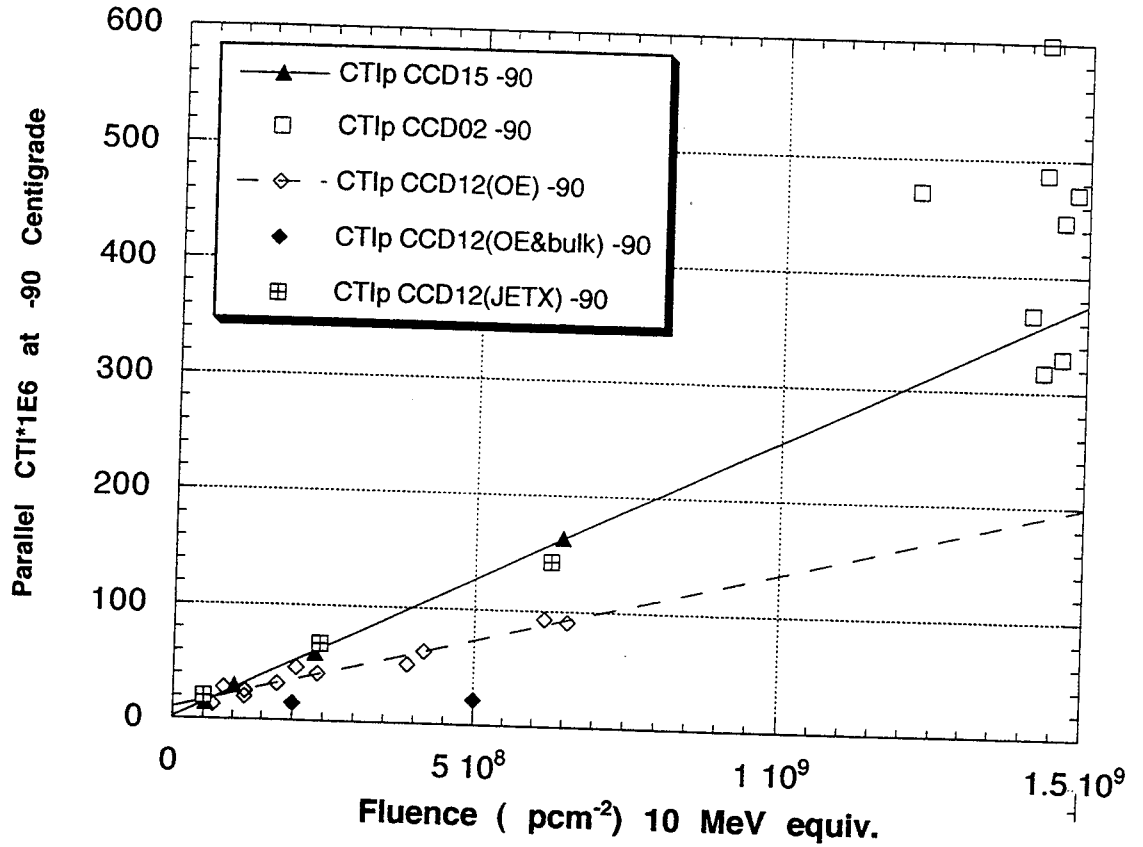
Fig. 4.20 as for fig. 4.19, except at -90 °C
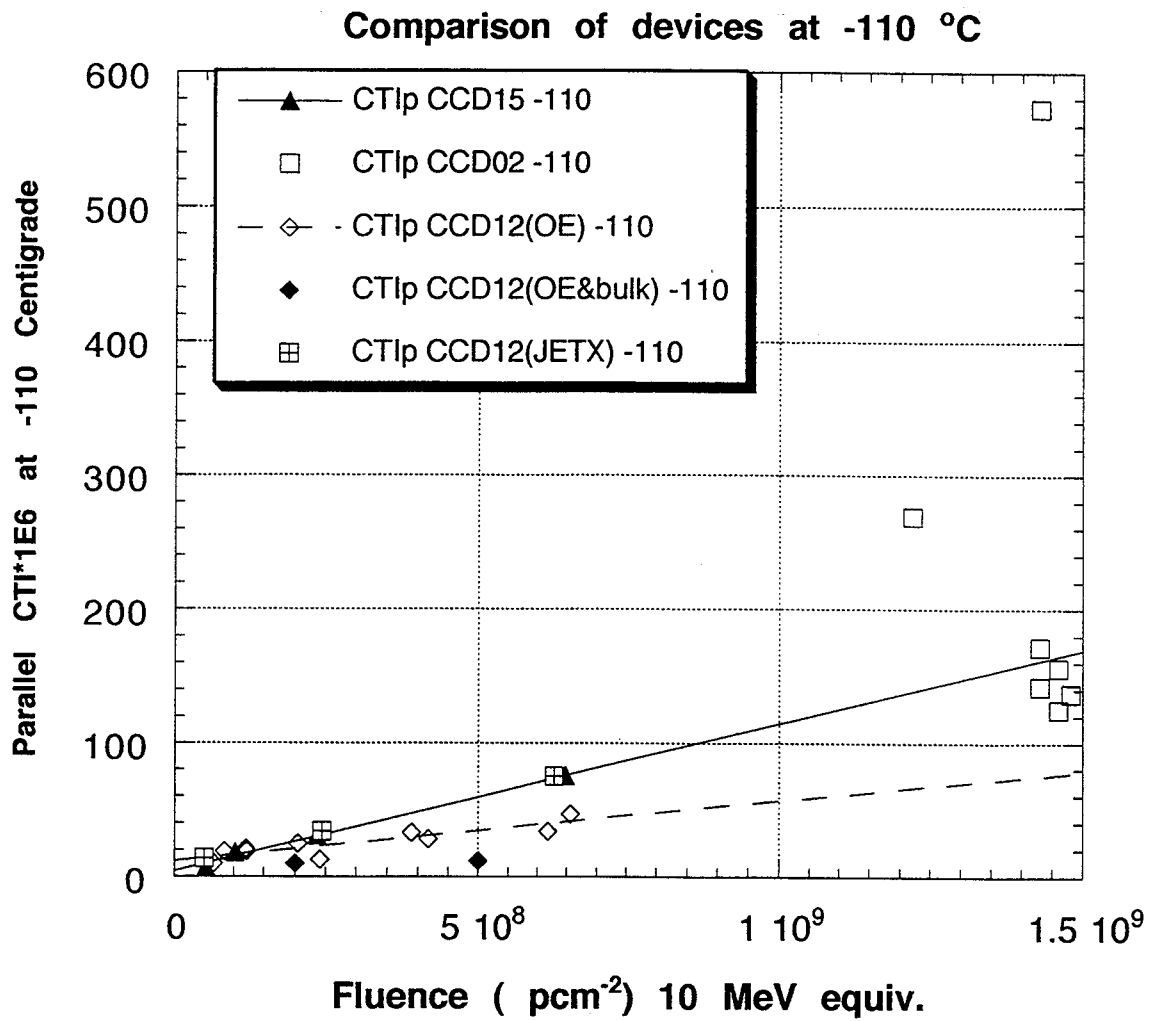
Fig. 4.21 As for fig. 4.19, except at -110 °C.

Comparison of various devices at -70 °C
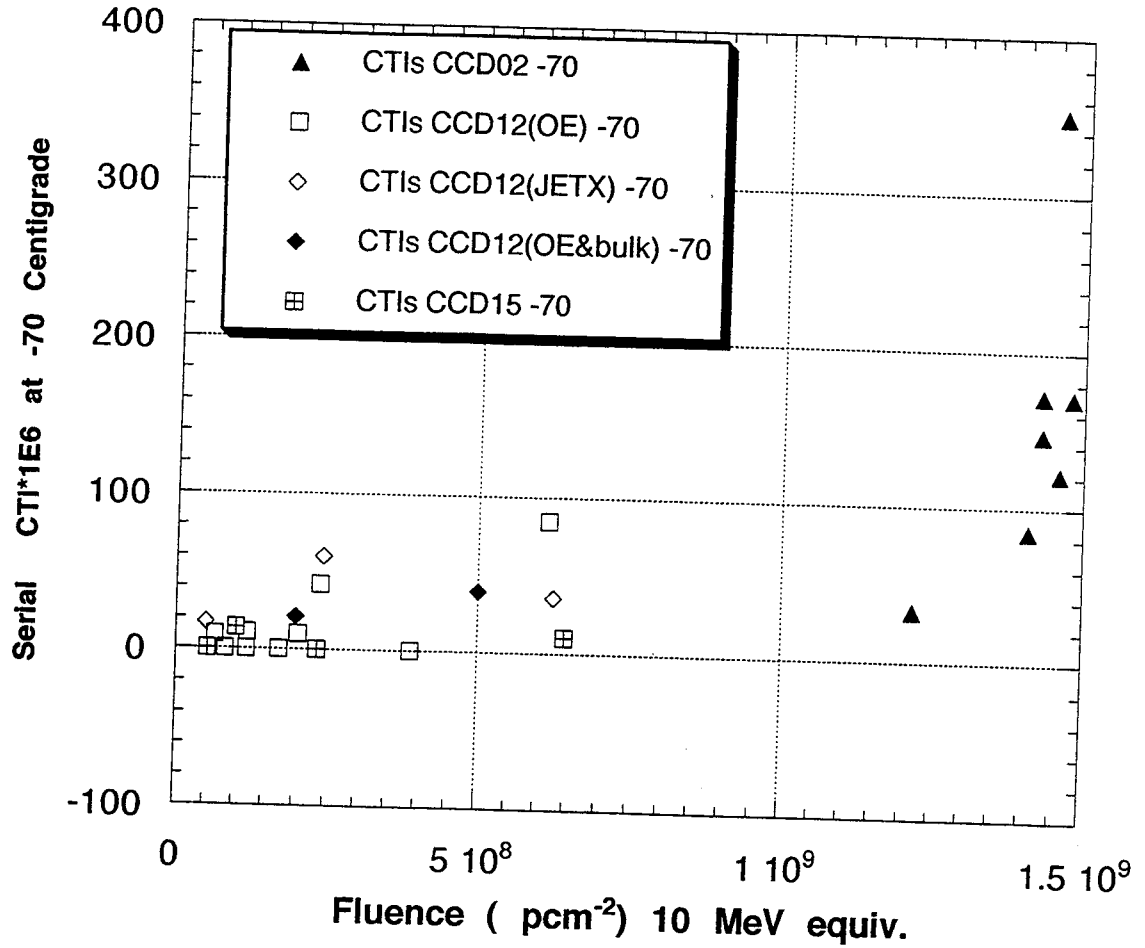
Fig. 4.22 Growth of serial CTI at -70 °C with proton fluence in WO2 experiments. 6.25 MeV used, converted to equiv. 10 MeV fluence.

Comparison of devices at -90 °C

Legend:
- ▲ CTIs CCD02 -90
- □ CTIs CCD12(OE) -90
- ◇ CTIs CCD12(JETX) -90
- ◆ CTIs CCD12(OE&bulk) -90
- ⊞ CTIs CCD15 -90

Y-axis: Serial CTI*1E6 at -90 Centigrade (0 to 200)

X-axis: Fluence (pcm^{-2}) 10 MeV equiv. (0 to 1.5 10^9)
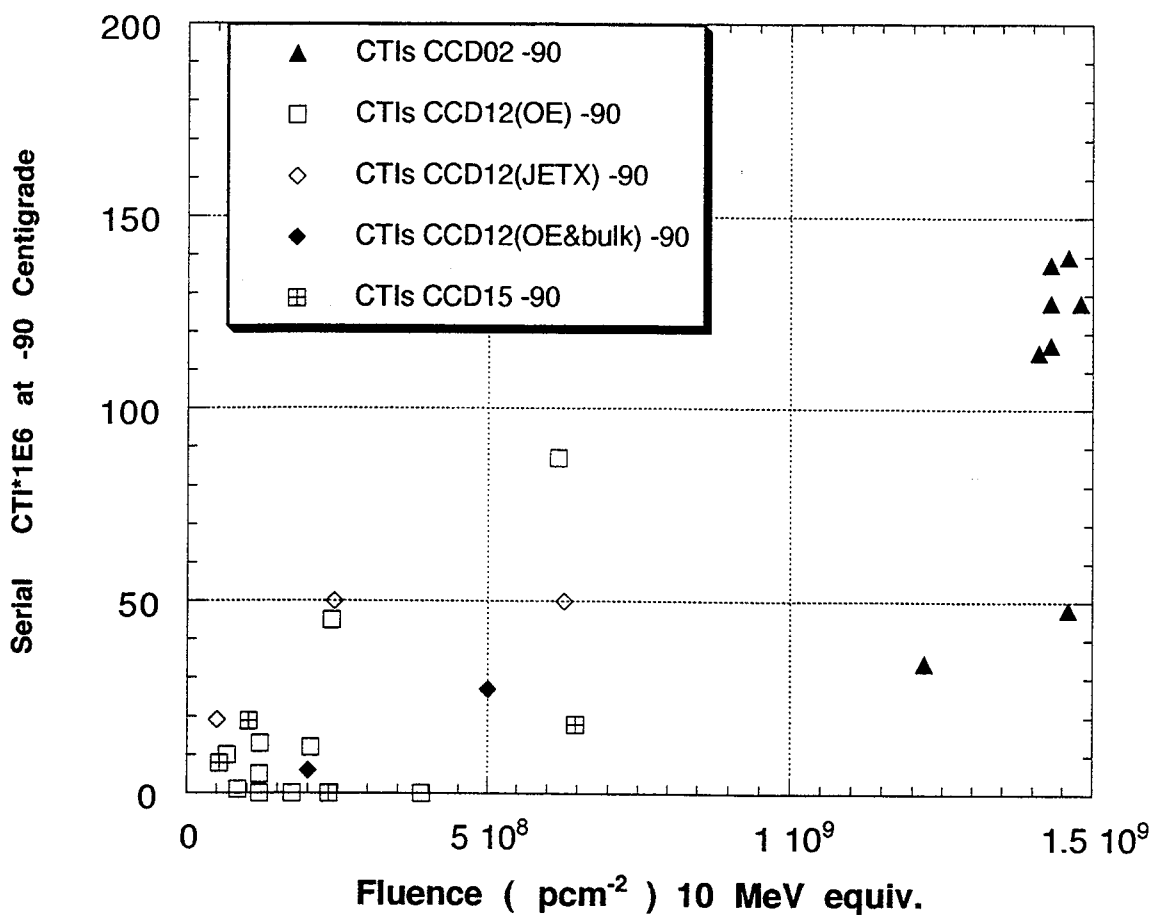
Fig. 4.23 As for fig. 4.22, except at -90 °C.
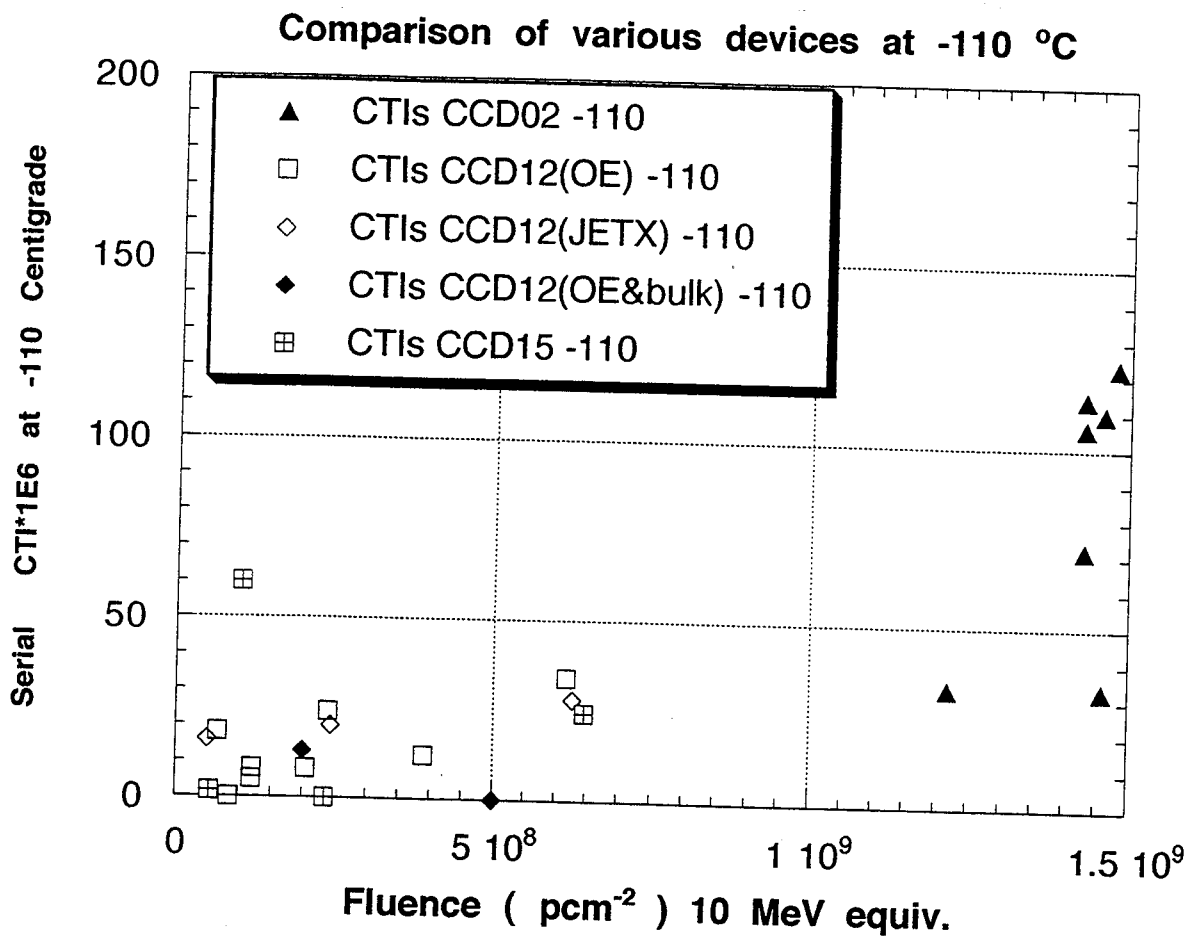
Fig. 4.24 As for fig. 4.22, except at -110 °C.
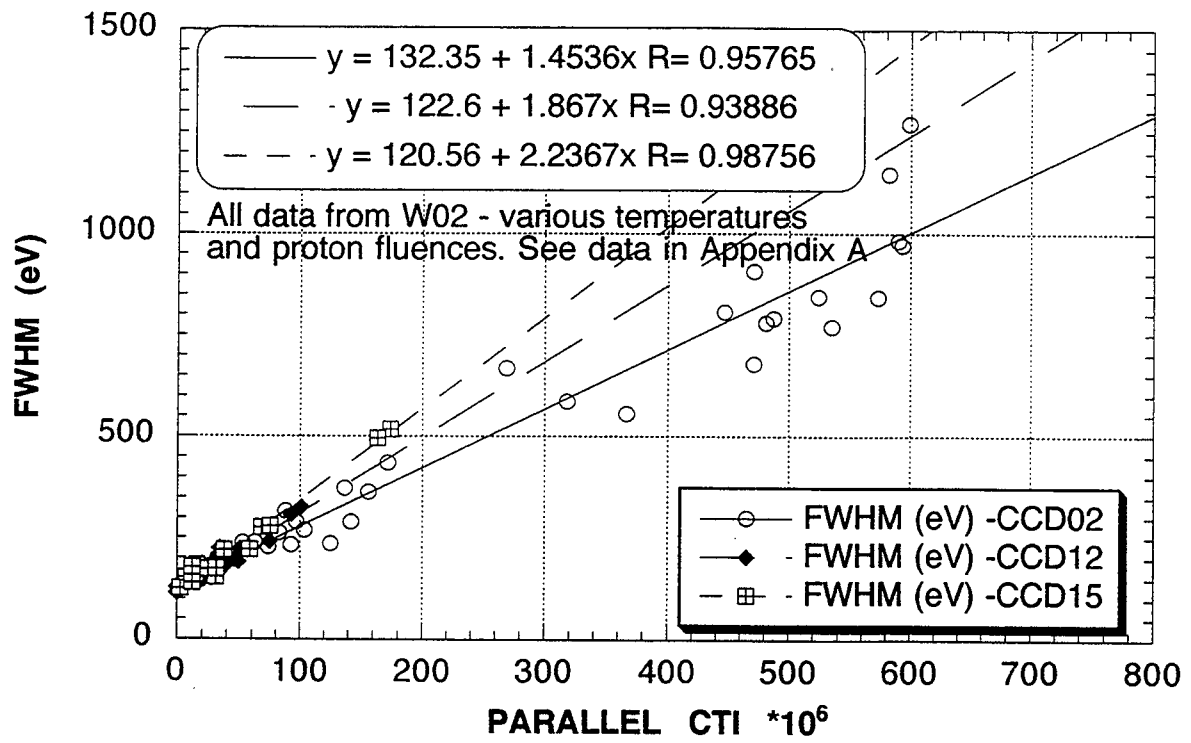
Fig. 4.25a Correlation between parallel CTI and Fe55 X-ray energy resolution
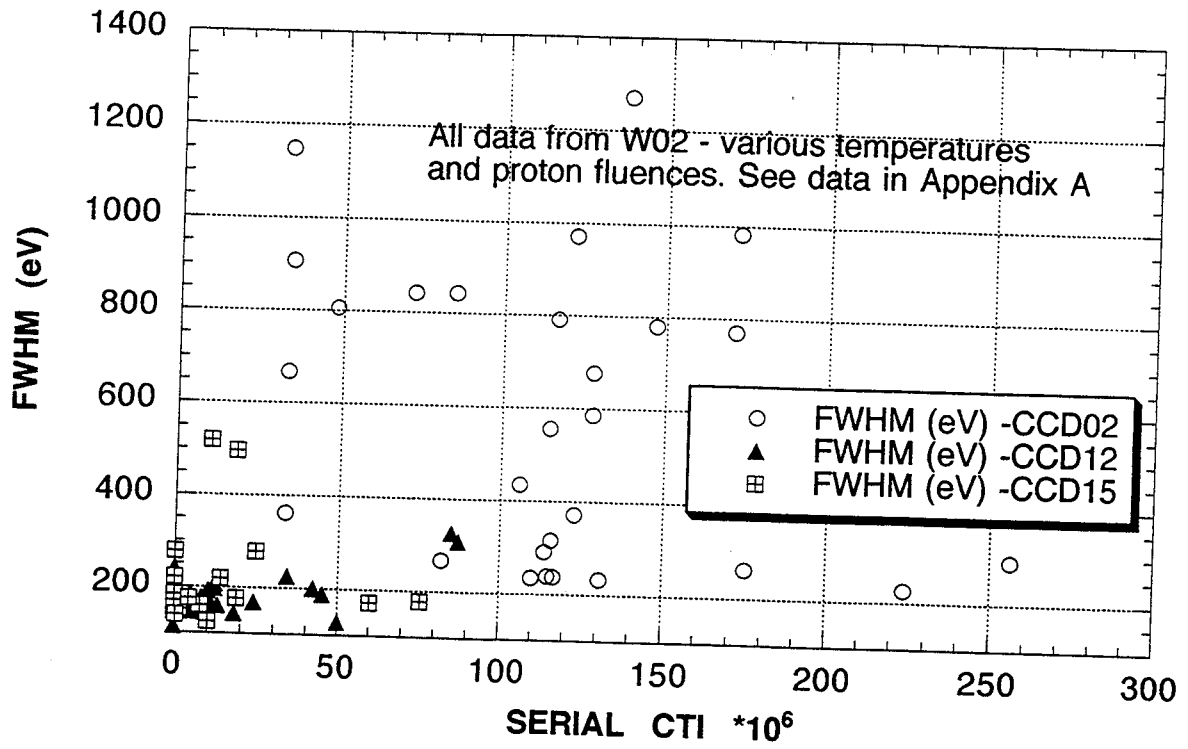
Fig. 4.25b SERIAL CTI versus Fe55 X-ray energy resolution
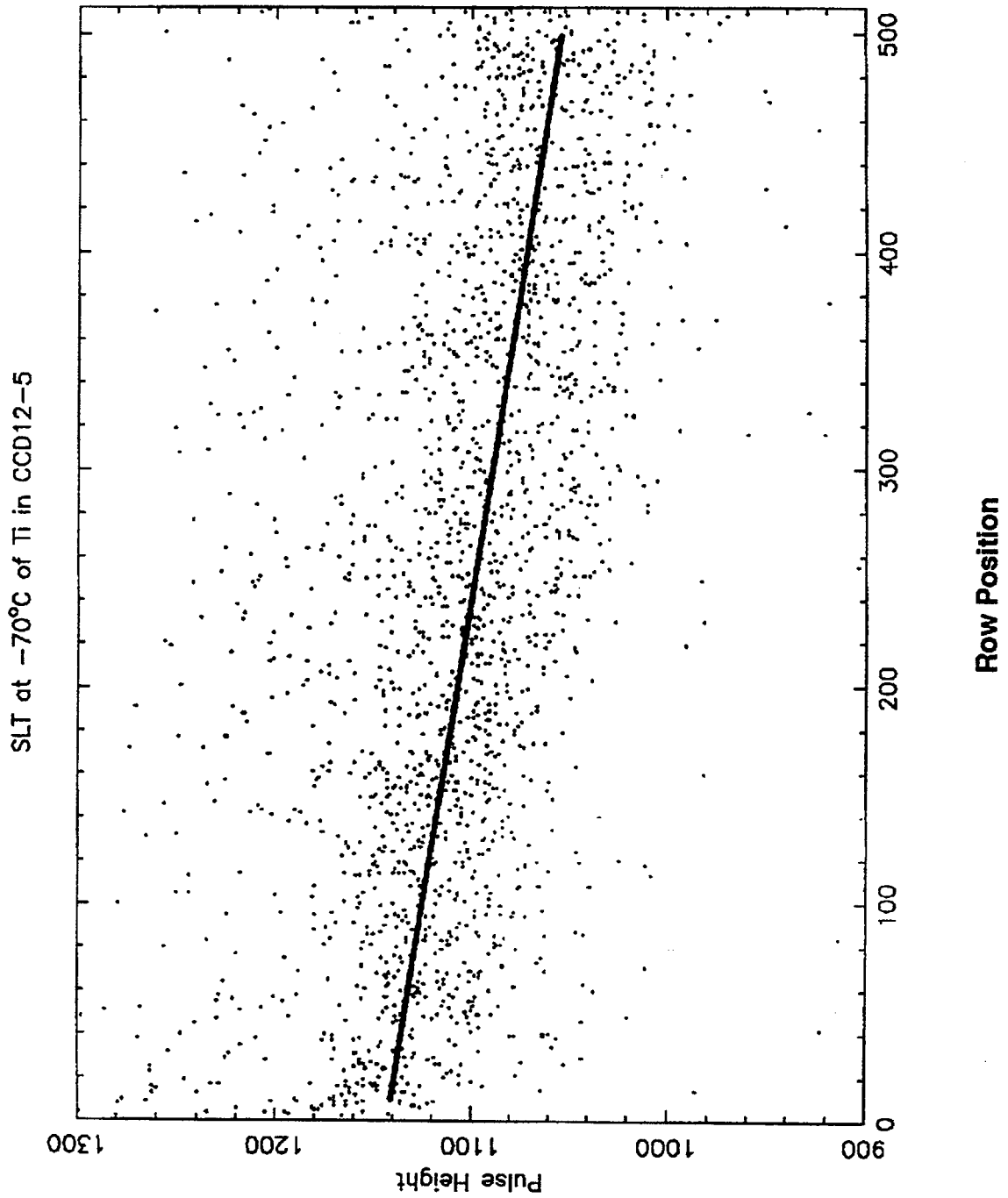
Fig 4.26 Stacked line trace of Ti X-ray photon response
at -70 Centigrade
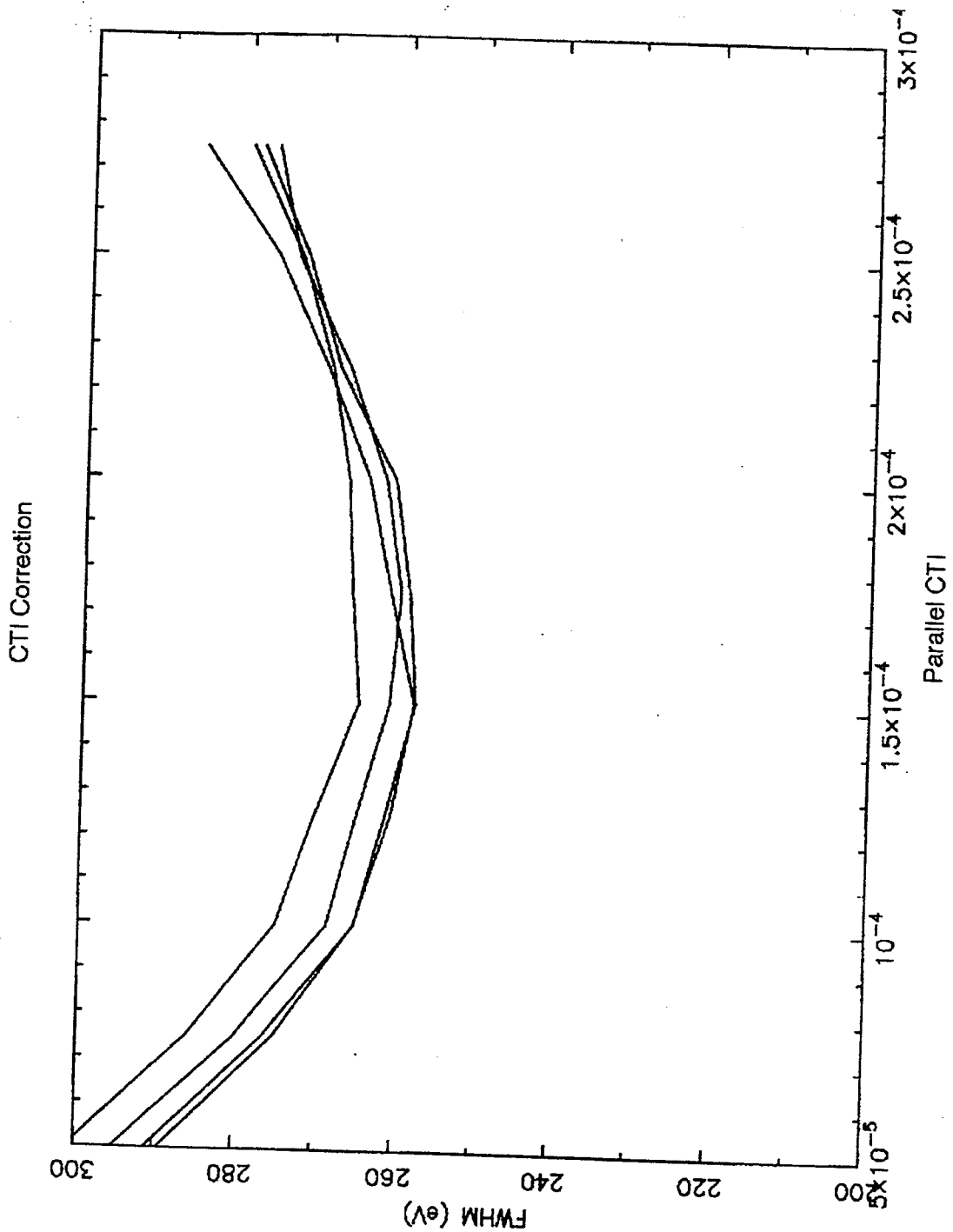
Fig. 4.27 CTI Correction at -70 Centigrade; parallel CTI vs
FWHM of x-ray response for 4 different serial CTI values
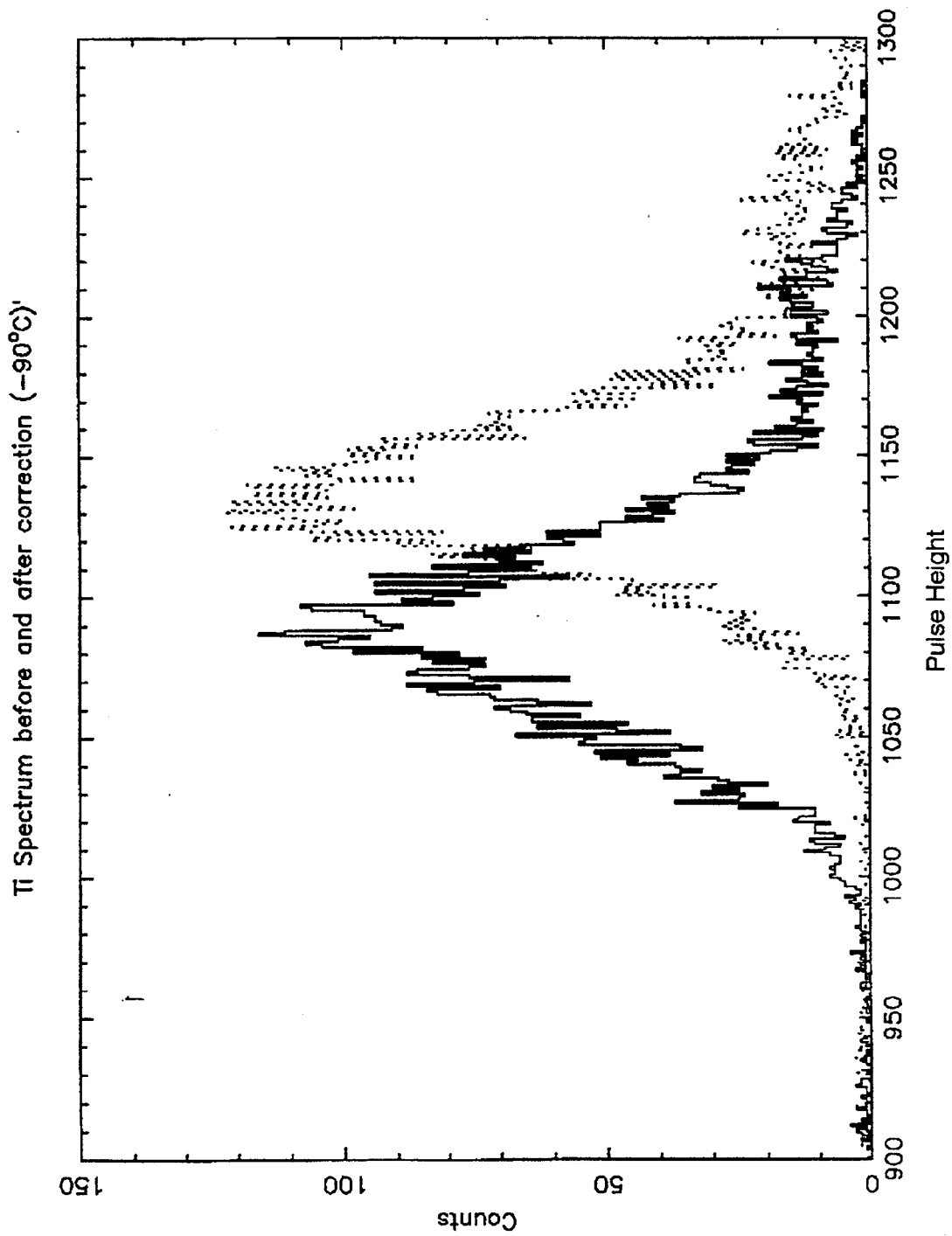
Fig. 4.28 Ti x-ray photon spectrum before and after
CTI correction. Temperature is -90 Centigrade.
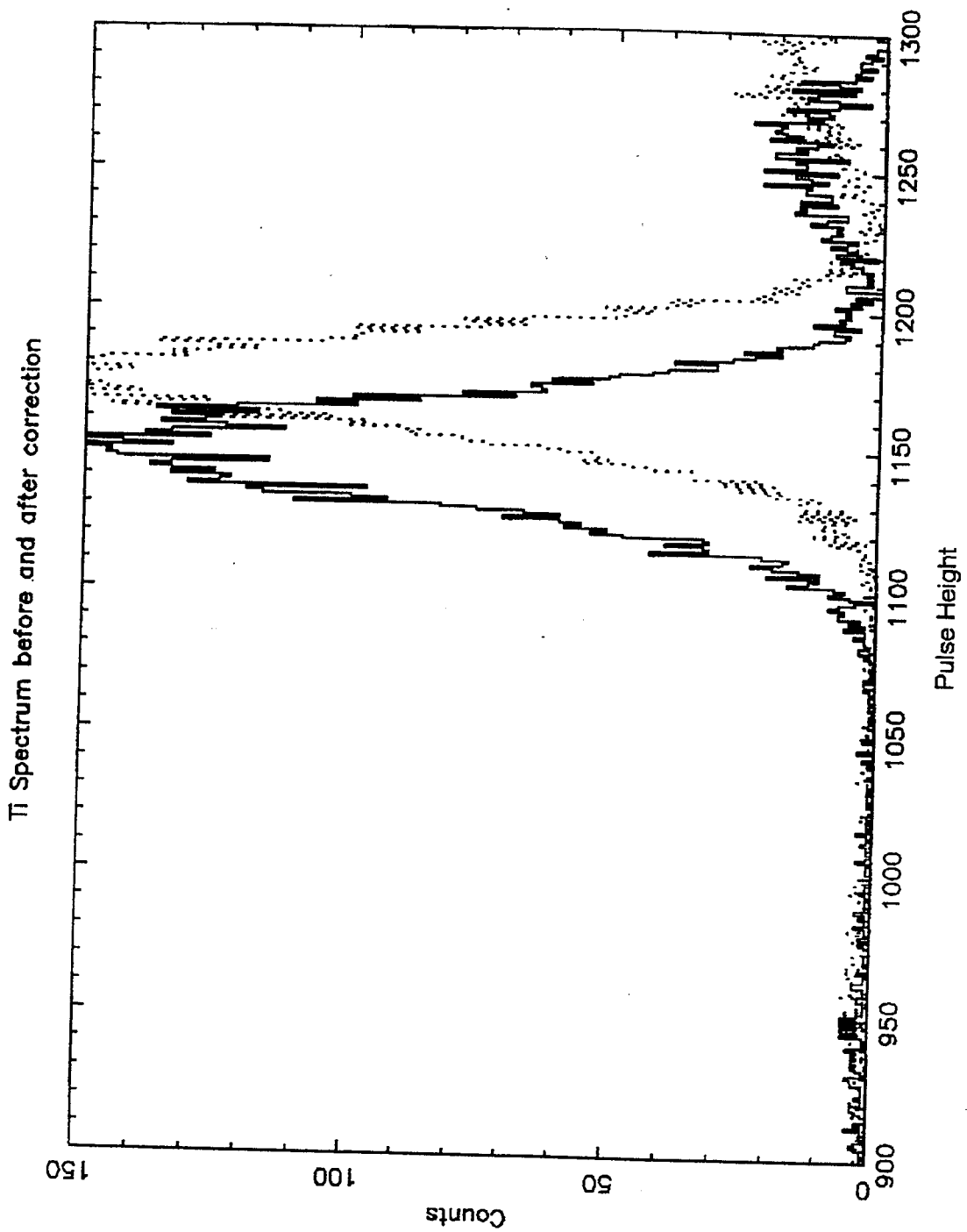
Fig. 4.29 Ti x-ray spectrum before and after CTI correction at -120 Centigrade
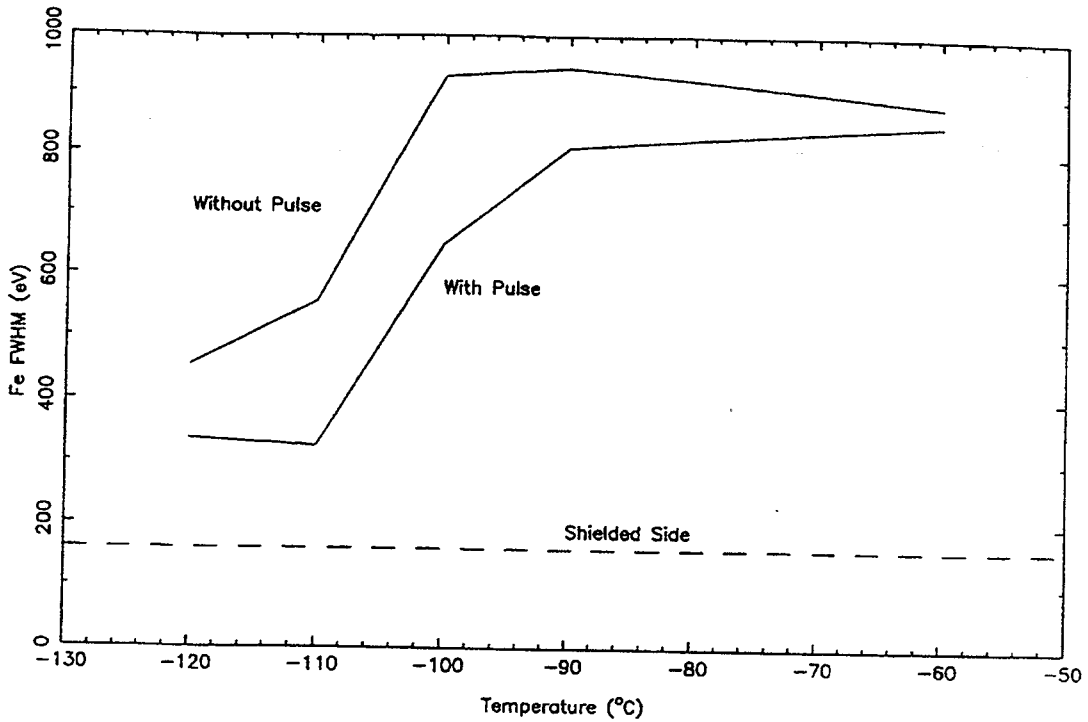
Fig. 4.30 Beneficial effect of charge injection pulses
on the energy resolution (FWHM) versus temperature
curve of a CCD02 device irradiated to about 3E9 10 MeV
protons per square cm.
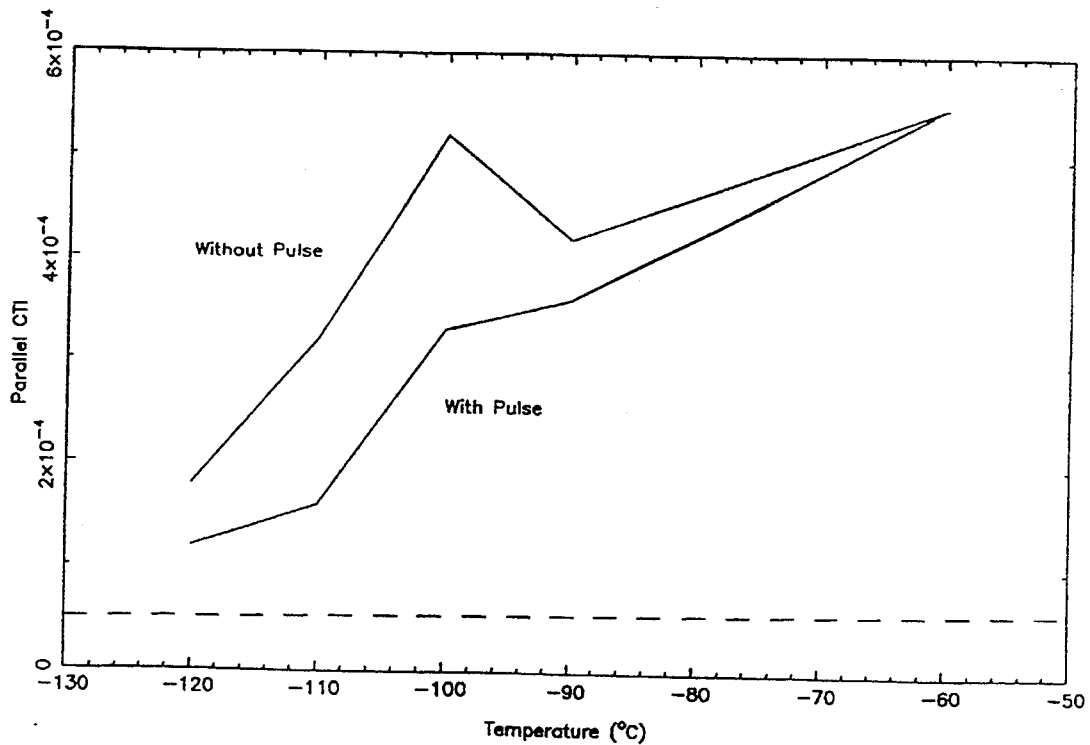
Fig. 4.31 Beneficial effect of charge injection pulses
on the parallel CTI versus temperature
curve of a CCD02 device irradiated to about 3E9 10 MeV
protons per square cm.

78

4.9 Dark Current Generation

Dark currents were measured as part of the post-irradiation characterisation, including routine measurement at -30, -50 and -70 °C. Dark current spectra, which are histograms of "frequency" (occurrences of a certain bin of values) versus current in e/pixel/sec, give the statistical distribution of dark-current in irradiated chips. The spectrum consists of a Gaussian peak and a "tail" containing dark current "spikes" (high rate of electron release from a few traps). The data is similar to that recorded in WO1. The dark current increases by about a factor 2 after 1.4E9 p cm^{-2} (10 MeV equivalent). For the XMM operating conditions this does not represent a significant problem. As will be shown later, this dark current is generated almost entirely at the surface. It should be noted that none of the devices tested operated in inversion mode.

4.9.1 Bulk Dark current - experience from neutron experiments

In this section, we note how models of minority-carrier degradation under neutrons can be useful in making predictions of dark current arising from protons. This section is based on recent work on high resistivity dodes performed by Brunel for the RD20 CERN programme (see e.g. Watts and Matheson, 1995) applied here to the average bulk current from the CCD depletion region. The damage constant for the minority carrier lifetime, τ, is related to the fluence of a particle, Φ_p, by Messenger's expression,

$$1/\tau = 1/\tau_0 + \Phi_p/K_\tau \approx \Phi_p/K_\tau \text{ for large fluences.}$$

Strictly, this expression represents the minority carrier lifetime in the silicon at large fluences under equilibrium conditions. During operation, CCDs are not in equilibrium. However, we make the assumption that the effective lifetime in the CCD depletion region can also be described by such a relation. We will show later that experimental data supports this assumption. The increase in the leakage current in a depletion region, I, per unit volume, V, due to irradiation can be written as:

$$I/V = \alpha\Phi_p$$

where α is given by,

$$\alpha = en_i/2K_\tau$$

where K_t is the damage constant for the carrier lifetime, n_i is the intrinsic carrier concentration and e is the charge on the electron. Messenger's 2-level model, (Messenger 1967), gives a K_τ value for 1 MeV neutrons of about 10^7 neutron s cm^{-2} for high resistivity silicon. The model uses Shockley-Read-Hall recombination theory. Carrier concentrations in the depletion region are low, hence one would expect that the value of K_τ for high-resistivity silicon can be used for the damage constant for the effective carrier lifetime. This gives an a value for 1-MeV neutrons of about 7. 10^{-17} A cm^{-1} at 20 °C, in agreement with measured values in high-resistivity float zone material diodes. This argument means that the same value can be used for determining the dark current from a depletion region from any type of silicon , irrespective of its resistivity. To confirm this we have irradiated two CCDs (EEV type CCD01) with 1 MeV equivalent neutrons from a Cf252 source. One CCD was made on standard low-resistivity material. The other was manufactured on 1500 ohm cm 50 µm thick epitaxial material. These devices are similar to the CCD02 device. The devices were irradiated to 3E10 ncm^{-2} at a rate of 5.6E7 n cm^{-2} hour^{-1}. The static dark current was measured as a function of VSS. This involves measurement of the device current from the drains with the gates grounded. All the drains are held at 20V. Fig 4.32 and 4.33 shows the measurements for both devices. Note that the inversion point is at 10V and 8.5V in the high resistivity and low resistivity devices respectively. This does not alter with irradiation because there is little ionising dose. Fig. 4.34 shows the increase in dark current versus VSS

after two fluences for the high resistivity CCD. Note that the curve is flat for VSS greater than the inversion point, 10V. The linear slope for lower VSS values is caused by the depletion region growing. Over this voltage range, the depletion width changes approximately linearily with VSS. To confirm this, a device model was used to calculate the depletion thickness versus VSS. Fig. 4.35 shows the calculation for the high resistivity CCD. The figure also indicates the surface potential so that the inversion point can be estimated. This occurs at an equivalent VSS of 6 volts. The difference between this value and the real CCD is because the model cannot estimate the flat-band condition. At the inversion point the depletion thickness is 24.2 μm - in agreement with the modelling. It grows by 1.43 μm/volt below the inversion point. This gives one a powerful cross-check on the data. From Fig. 4.34 the low VSS data implies 0.32 nA/μm using the device model number for μm/volt. In inversion, the value is 7.8 nA. This implies that the depletion thickness in inversion is 24.2 μm - in agreement with the modelling. Fig. 4.36 shows the dark current per unit volume versus neutron fluence. From this we infer that at 20 °C, $\alpha = 3.5 \ 10^{-17}$ Acm^{-1} for both the low and high resistivity CCDs. Because of annealing corrections (see later) we believe that this is consistent with measurements made with high resistivity float zone diodes. For silicon microstrip detectors made for high energy physics, α has been measured for many types of particles at many energies and found to scale with the Non Ionising Energy Loss (NIEL). As a result, we now have a simple way to predict proton-induced increases in the bulk depletion dark current. The two other sources of dark current are from the surface and undepleted bulk. The latter source has an n_i^2 dependence and is only important at temperatures above room temperature. Estimated increases in dark current at 300K for a fluence of 3.6E9 10 MeV protons cm^{-2} (2Krad) are given in the following table:

Table 4.5 Estimated increase in dark current 300K for 3.6E9 10 MeV p cm^{-2} (2 krad)

CCD Type	Surface (nA/cm^2)	Depleted bulk (nA/cm^2)	Total (nA/cm^2)
20 ohm-cm 20μm epi (5 μm depletion)	0.5	0.5	1.0
1500 ohm-cm 50μm epi (25 μm depletion)	0.5	2.5	3.0

In table 4.5, the calculation for the surface contribution assumes that 2Krad of protons give the same number of surface states as 2 krad of beta particles. This is not strictly so, as explained later. Bulk contribution calculations assume that 10 MeV protons are about 4.4 times more effective than 1 MeV neutrons. Hopkinson (1992) estimates a rate of 0.1 nA/cm^{-2}/krad in a standard device for 10 MeV protons based upon a different theoretical model.

4.9.2 Analysis of WO2 dark current data - protons

4.9.2.1 Dark current data at -30 °C to -70 °C

The data is given in Table 4.6. It shows similar increases as were found for the Work Order 1 data.

The data for the irradiated section on integration is plotted in Fig 4.37. The temperature dependence of the dark current -dominated by the surface contribution- is 0.7eV as found by Roy et al. 1989.
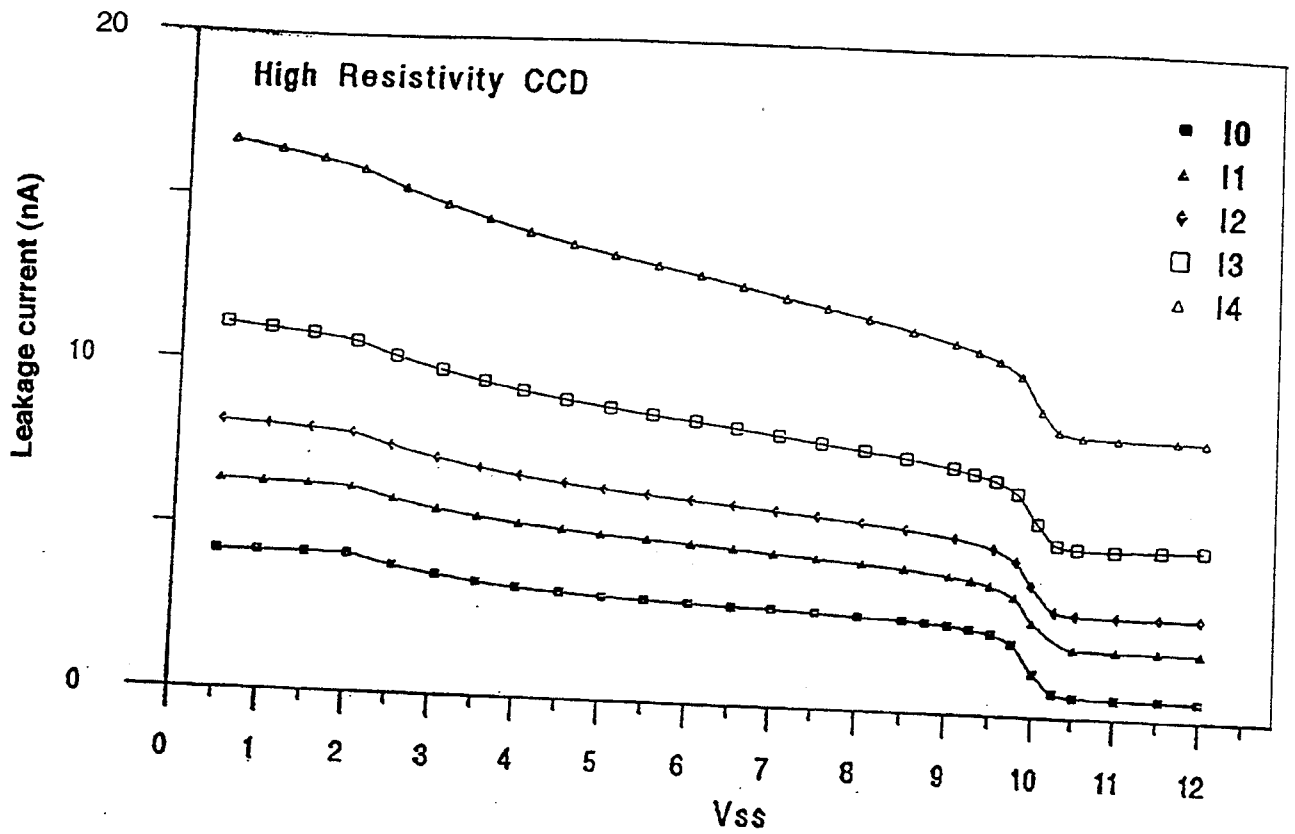
Fig. 4.32 Dark current versus Vss curves at 305K after
Cf252 neutron irradiation. EEV CCD01 device on
high resistivity silicon.
1 MeV equiv. neutron fluences are:-
I0 - pre-irradiation
I1 - 3.8E9 n/cm2
I2 - 6.4E9 n/cm2
I3 - 1.5E10 n/cm2
I4 - 3.0E10 n/cm2
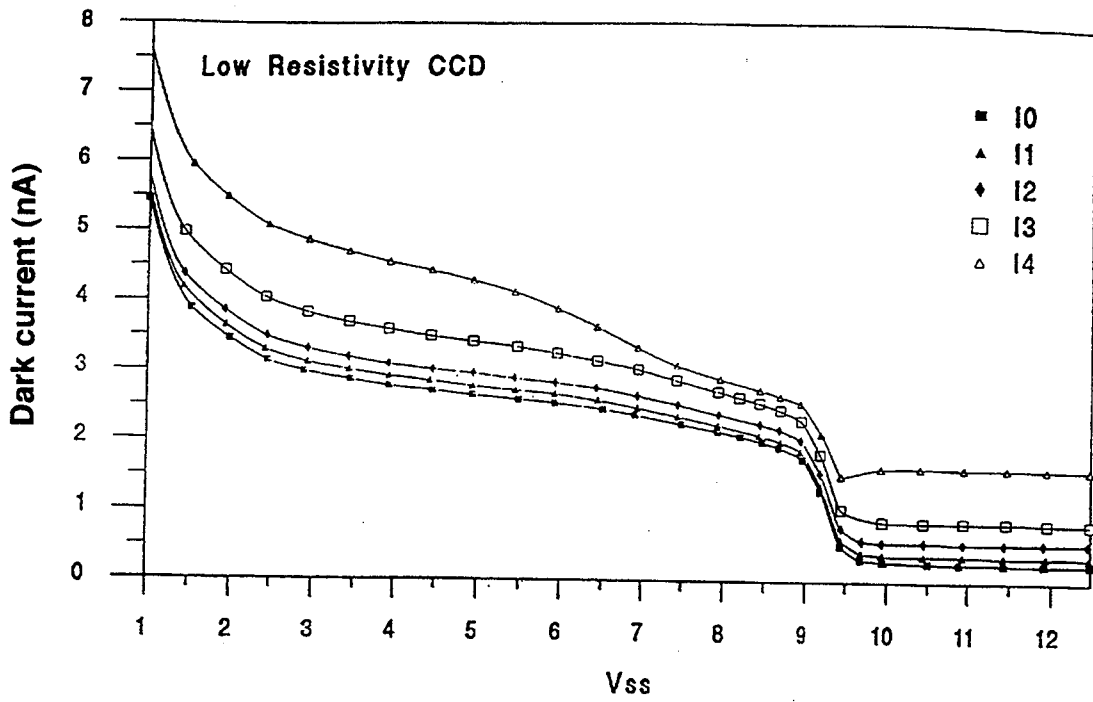
Fig. 4.33 Dark current versus Vss at 305K after Cf252
neutron irradiation; CCD01 with low-resistivity
epitaxial layer. See Fig. 4.32 for fluence information.
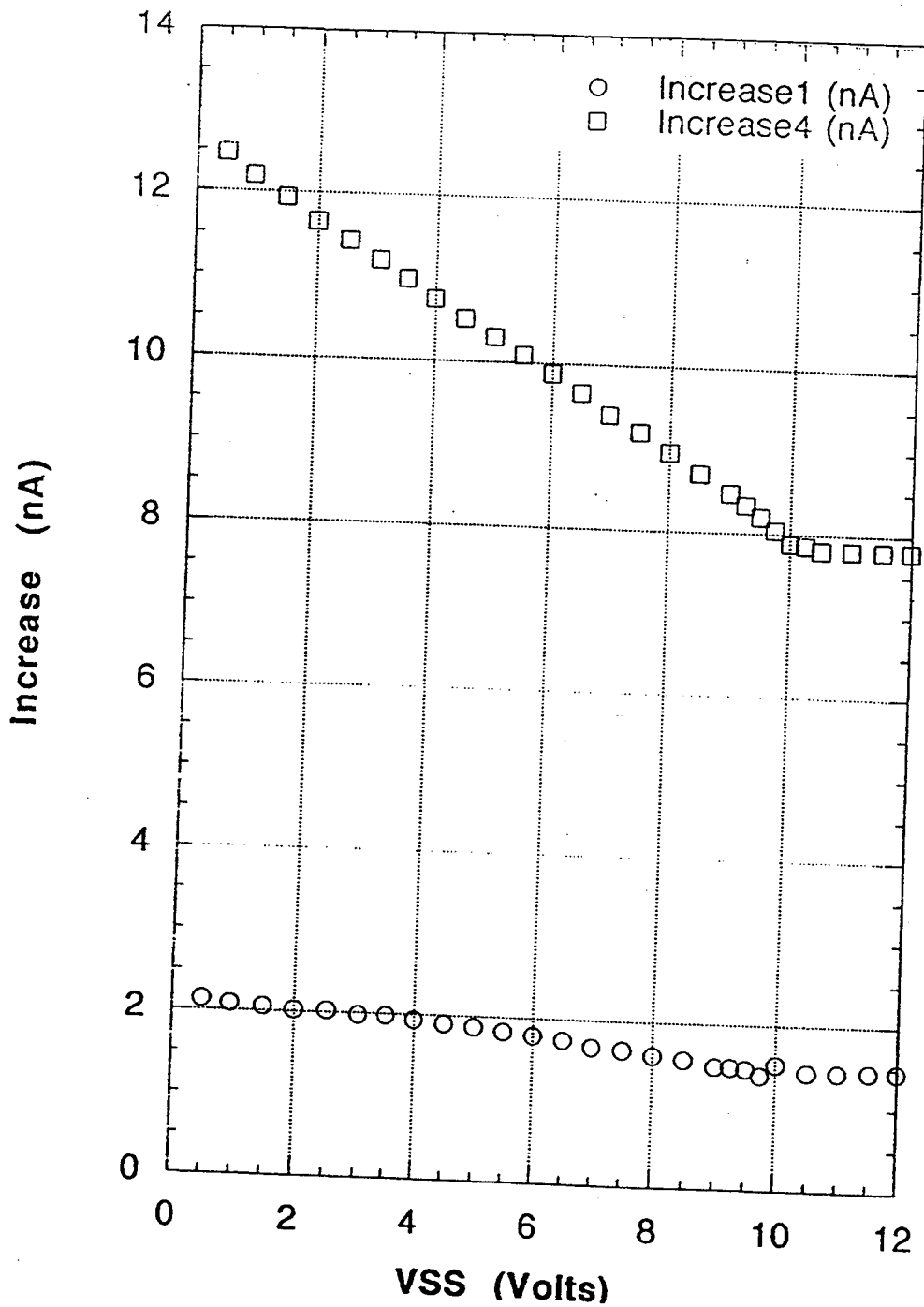
Fig. 4.34 Increase in leakage current - relative to pre-irradiation value - as function of substrate voltage after 3.8E9 (labelled 1) and 3E10 (labelled 4) 1 MeV equiv. neutrons per square cm.
High resistivity EEV CCD01. Neutrons produced by Cf252.
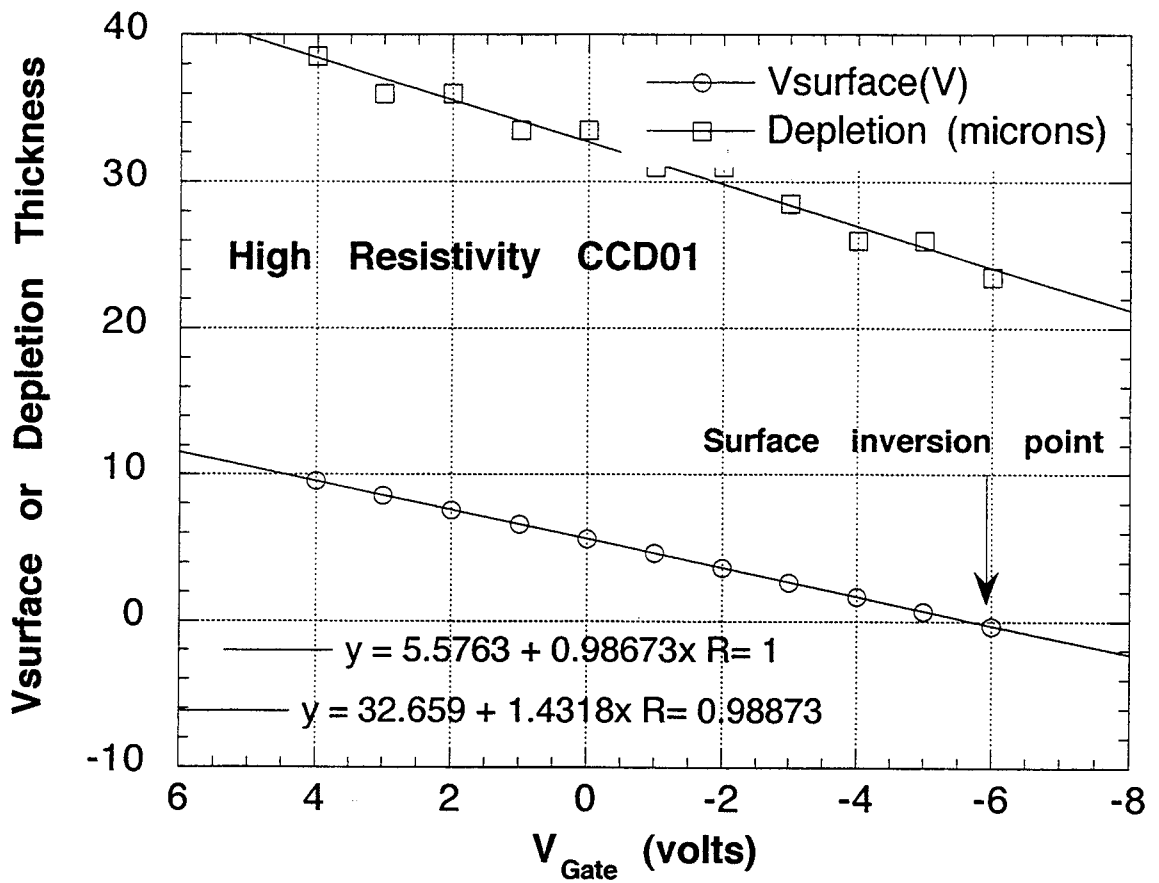
Fig. 4.35 Calculated depletion thickness in an EEV CCD01 device made on high resistivity silicon as a function of gate voltage. The substrate voltage is zero volts. The figure also shows the surface potential.
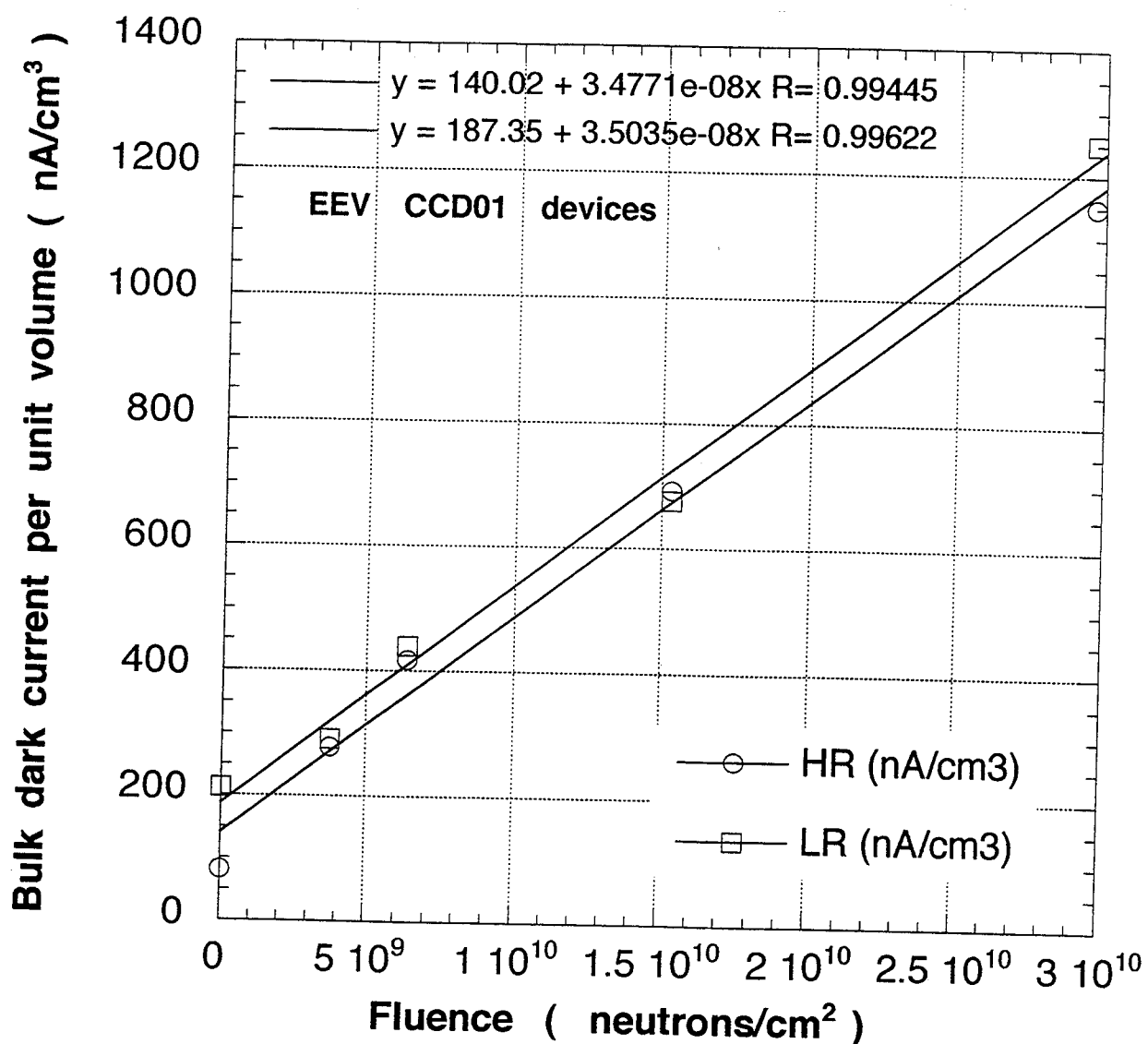
Fig. 4.36 Increase in bulk dark current per unit volume for low and high resistivity EEV CCD01 devices as a function of 1 MeV equivalent neutron fluence. The source was Cf252. Fits to data show linear dependence.

Table 4. 6 Dark current measurements at three temperature values on 6.25 MeV proton-irradiated CCD02 devices

Device/Temp °C	SHIELDED		IRRADIATED	
	Dark current on integration $I_d(int)/e\ s^{-1}$	Dark current on readout $I_d(read)e\ s^{-1}$	Dark current on integration $I_d(int)/e\ s^{-1}$	Darkcurrent on readout $I_d(read)e\ s^{-1}$
02-1-30	142	77.9	169	94.3
	144	74.9	170	93.0
-50	10.5	7.05	12.7	9.22
	10.3	7.77	12.8	9.40
-70	0.305	0.816	0.114	0.490
	0.190	0.326	0.190	0.653
02-2-30	187	94.2	277	132
	188	95.3	280	135
-50	14.3	11.0	21.5	14.7
	14.4	9.74	22.1	14.0
-70	0.543	0	0.466	1.33
	0.504	0.499	0.582	1.33
-80	0.310	0.166	0.543	0
	0.466	0.499	0.427	1.16
-90	0.349	0.499	0.039	0.499
	0.310	0.333	0.310	0.499
02-3-30	194	102	300	149
	195	101	304	149
-50	13.4	10.5	20.8	13.6
	13.4	9.48	21.3	14.2
-70	0.312	0.669	0.312	0.836
	0.273	0.334	0.390	1.00
02-5-30	187	97.1	322	156
	188	97.7	332	157
-50	17.2	9.27	30.1	15.7
	17.4	8.94	30.7	14.9
-70	0.512	1.35	0.630	1.69
	0.551	0.506	0.670	1.5

Notes:

1.WO2 batch - see Table 3.4 for fluences
2. Readout conditions :   30 sec integration time except for CCD02-1 (15s)
                            7 sec readout time
                            signals collected from dark frame with cutoff at 3s
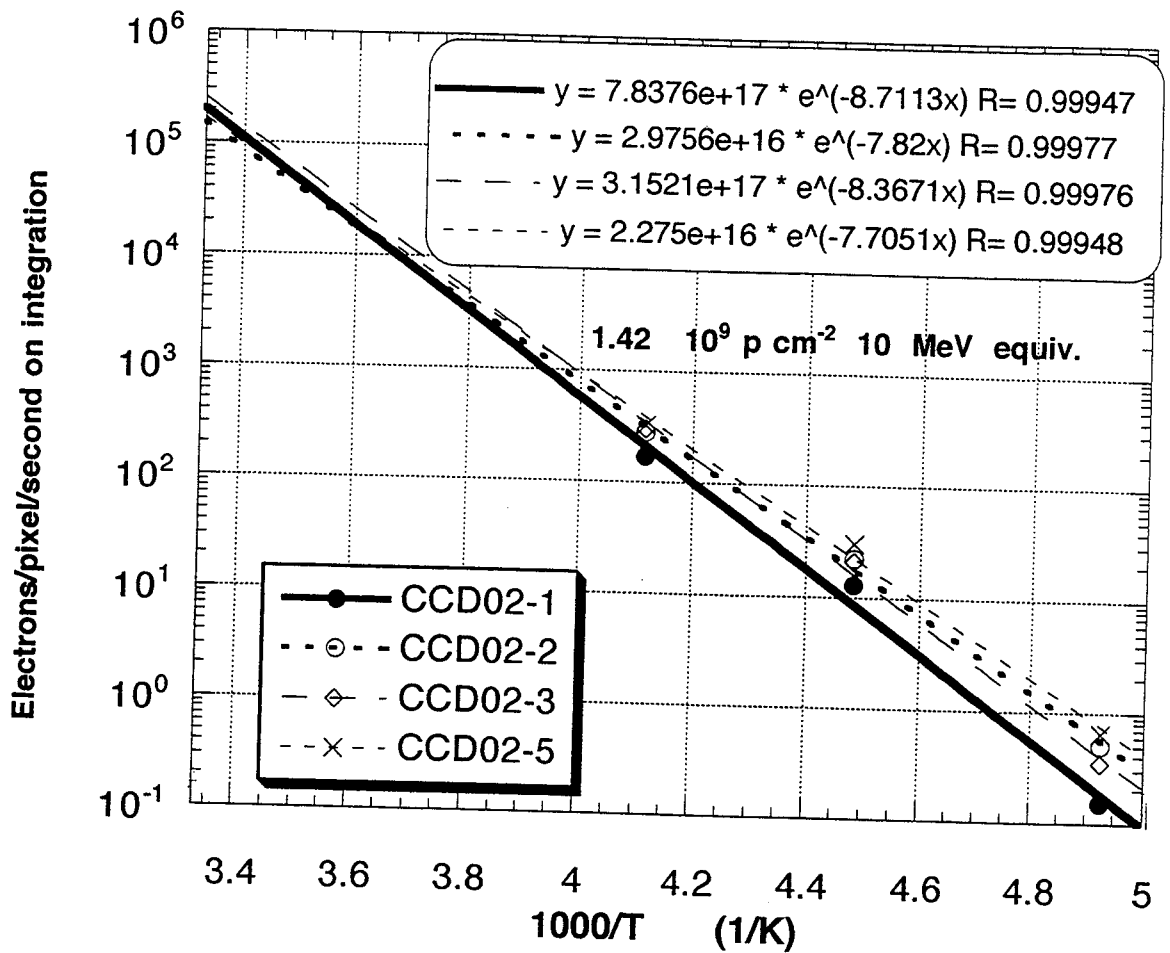
Fig 4.37 Variation of dark current with temperature. Data is from Table 4.6.
Fits to the data give a 0.7 eV temperature dependence.

4.9.2.2 Dark current data at room temperature

As a check on the beam dosimetry and to understand in detail where the dark current was being generated, it was measured as a function of VSS after irradiation for all CCD02 devices . Both the current and CCD output voltage were monitored. Fig. 4.38 shows the clocked dark current as a function of VSS for CCD02-5. It clearly shows that the irradiated region of the device has roughly doubled its dark current relative to the unirradiated region. The current in the inversion region - VSS greater than 9V includes some surface contribution due to the clocking. Fig. 4.39 compares the static dark current -see section 4.9.1 for an explanation of this- with the clocked dark current. As expected, the static dark current is lower because the condition of the SiO_2/Si interface is better defined than for the clocked condition. This figure cannot differentiate between the irradiated and non-irradiated half of the CCD02. For comparison, Fig. 4.40 shows the static dark current for an unirradiated CCD02. Fig. 4.41 shows all the data from the CCD02 devices for VSS=5V (operating conditions) and VSS=10V. At 10V, the device will not image and most of the dark current is still generated at the surface. There is reasonable agreement between the devices. The statistical spread is not improved when the data are normalised to a fluence of 1E9 pcm^{-2} (10 MeV equivalent). If the surface leakage is taken as a dosimetric quantity, this data suggests that the proton fluence for sample CCD02-1 was overestimated by a factor 2.0

From this data, of the CCD02 set, correcting for the fact that only 60% of the device was irradiated, we estimate that at VSS=5V, the responsivity of the surface leakage current to radiation is 3.5 nA/cm^2/krad at 300K. Care must be taken with this calculation because 1E9 cm^{-2} 10 MeV protons give a factor 0.7 times less ionising dose than the 6.25 MeV protons that we actually used. This responsivity value is a factor **14 times** higher than estimated. The estimate was based on 1 MeV electron irradiation. We believe that this discrepancy may be due to the fact that 1 MeV electrons have a LET of 0.4 keV/μm compared to 11.7 keV/μm for the 6.25 MeV protons. The effect of low energy electrons in the beam has been considered. We do not have enough information from the dosimetry to make an estimate of the effect of such a background. Hopkinson 1992 has measured CCD02 devices after irradiation by 4 krad of 10 MeV protons. His data implies a surface leakage current responsivity value at 300K of 1.56nA/cm^2/krad which is in broad agreement with our figure.

For the CCD02 devices it is difficult to measure the small increase in the bulk current. From the static current measurement at VSS=10V (inversion) and comparing with an un-irradiated CCD we estimate that 3.6E9 10 MeV protons give a bulk current of 0.25nA/cm^2. This is in reasonable agreement with the estimate.

From these measurements we can now revise the above table estimating the dark currents produced by 3.6E9 10 MeV protons (2 krad) at 300K.

Table 4.7 Measured increase in dark current 300K for 3.6E9 10 MeV p cm^{-2} (2 krad)

CCD Type	Surface (nA/cm^2)	Depleted bulk (nA/cm^2)	Total (nA/cm^2)
20 ohm-cm 20 μm epi (5 μm depletion)	7.0	0.25	7.25
1500 ohm-cm 50μm epi (25 μm depletion)	7.0	1.25	8.25

It is important to note that the depletion bulk current can anneal and that the surface current may reverse anneal.
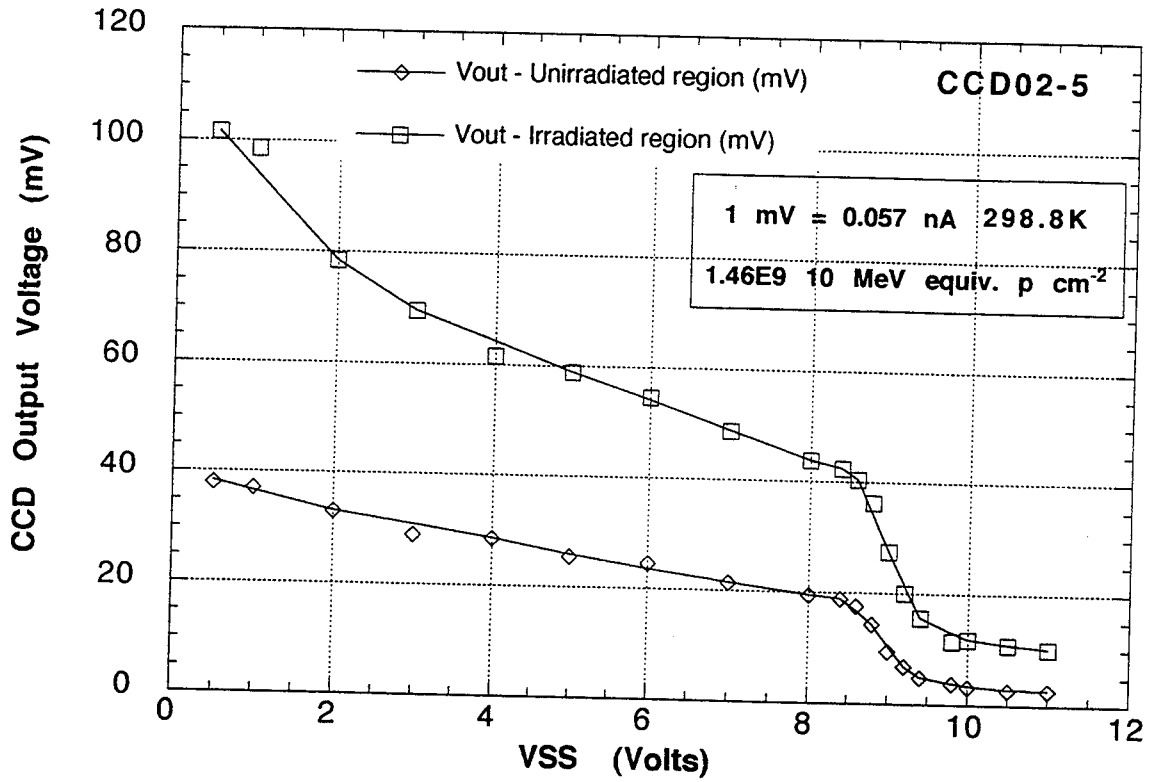
Fig 4.38 dark current versus Vss curves at 298.8K after 6.25 MeV proton irradiation; CCD02 sample 5 with low-resistivity epitaxial layer. Comparison of irradiated and unirradiated areas.
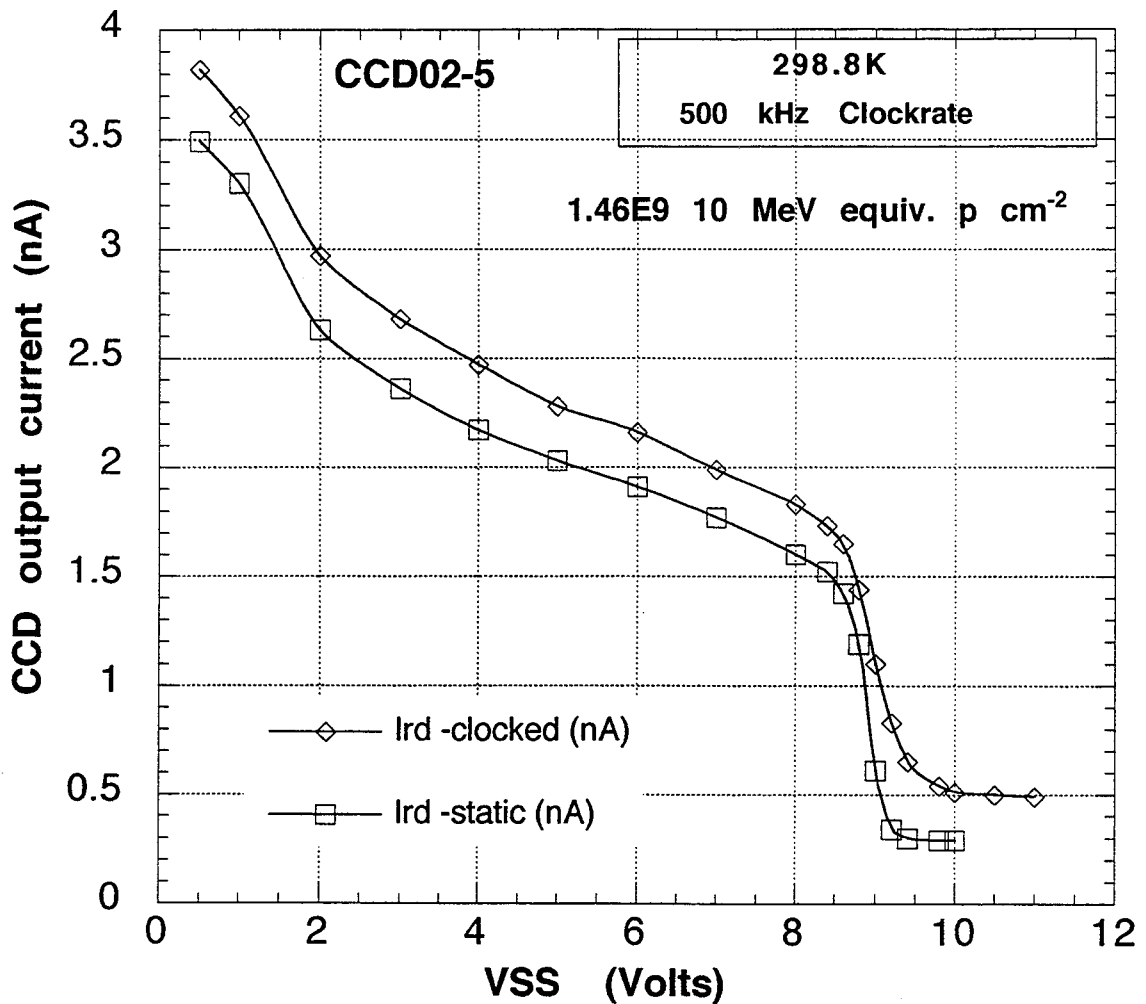
Fig 4.39 Dark current curves versus Vss at 298.8K after 6.25 MeV
proton irradiation; CCD02 sample 5 with low resistivity epitaxial layer.
Comparison of clocked and static currents in the irradiated area.
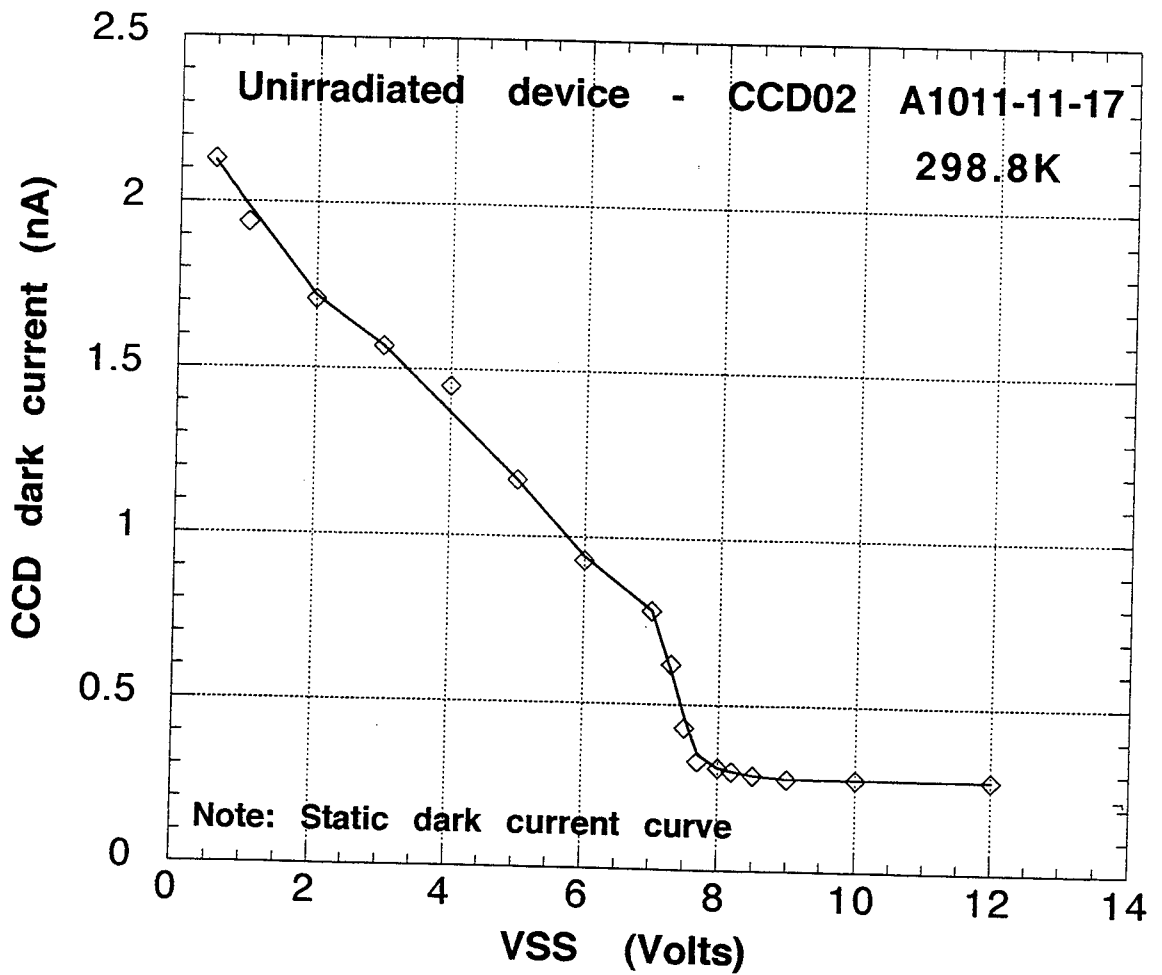
Fig 4.40 Dark current versus Vss curve at 298.8K in an
unirradiated CCD02 sample (A1011-11-17) with low-resistivity
epitaxial layer
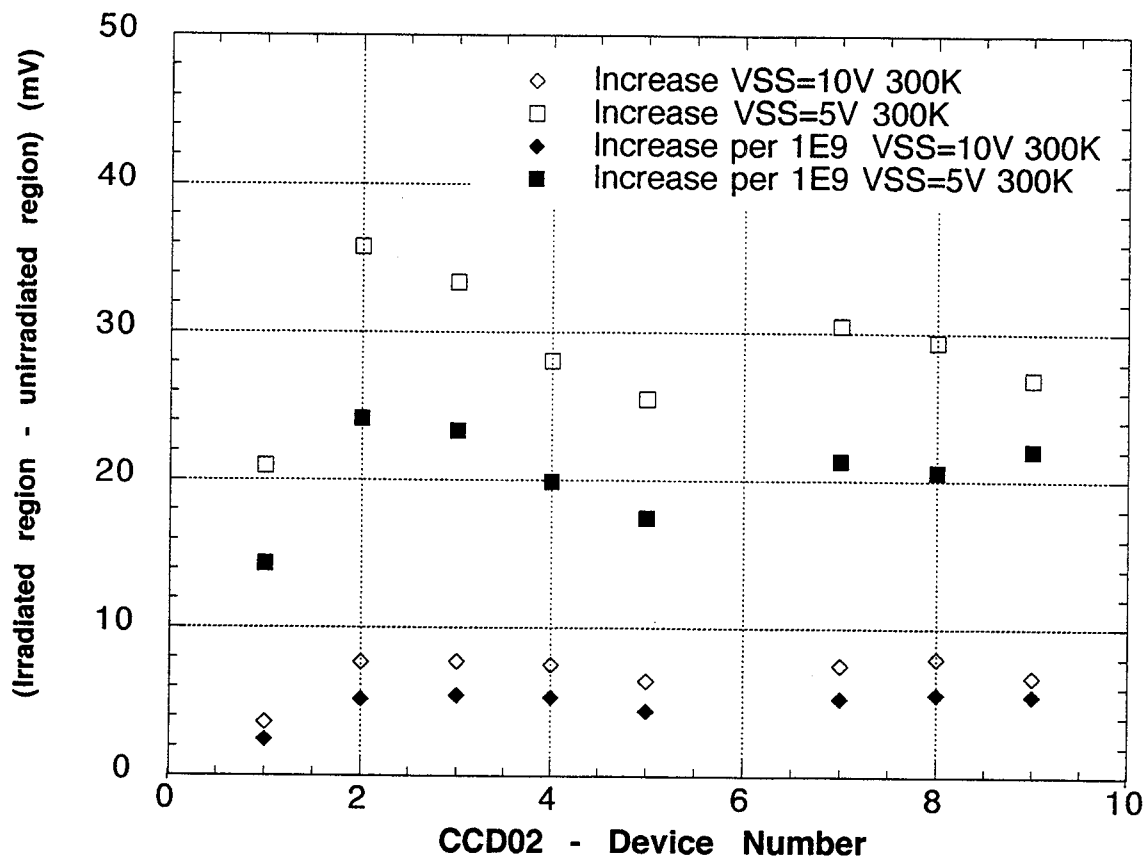
Fig. 4.41 Compilation of dark current values curves at 300K after
6.25 MeV proton irradiation; CCD02 set from the same wafer - low resistivity.
Dark current value taken at VSS=5 and 10 Volts.

4.10 Annealing of bulk damage at room temperature

The defect kinetics model described in Section 5 suggests that defect clusters are unlikely to form in the buried channel. Since stable VP centres predominate, one would not expect to see any room temperature annealing of the CTI. This is consistent with the WO1 data. In Section 5 we argue that cluster damage is more likely in the p-type layer. Because the clusters are unstable, room temperature annealing of the bulk dark current is possible. This has indeed been seen by Hopkinson (1992), who reports annealing of dark current spikes - tail of the dark current histogram - over three months at room temperature.

To investigate the bulk damage to silicon caused by MeV protons, we investigated two high resistivity n-type diodes, irradiated during the second proton run and made DLTS measurements. Each diode received 2.5E9 6.25 MeV p cm^{-2}. On the basis of NIEL calculations and earlier neutron irradiations it was thought that this would be a suitable dose. The peak at 227K in Fig 4.42 shows that the production of defects around Ec-0.4 eV is about 20 times higher than expected and their concentration is at the high limit for the DLTS technique. A similar peak is seen with neutron irradiation. After neutron irradiation this peak is seen to anneal over a period of weeks at room temperature.

A 15 minute isochronal anneal shown in Fig. 4.43 shows that one of the defects in this peak anneals at just 70 ^{o}C. The remaining contribution is due to the divacancy, V_2. A similar result has been obtained with high resistivity diodes exposed to MeV neutron irradiation (Matheson et al. 1995). This is referred to as EX in some parts of this report. This leads us to speculate that the EX defect may be responsible for some of the hot pixels in CCDs. It certainly shows that terminal clusters are created by MeV protons and that these are unstable at room temperature.

4.11 Annealing of CCDs at elevated temperatures

The VP centre anneals in a straightforward manner at 150 ^{o}C. The large proportion of CTI recovery at this temperature is evidence of a low divacancy concentration in the channel region.

Samples which have been annealed at elevated temperature show evidence of dissociation of the VP centre causing more E1 -probably VO - traps to form. Also, it is possible to "over-anneal" the devices, i.e. to go through a minimum and to once again degrade the CCD CTI -section 4.11.1.2. The provision of heaters in CCD cameras to perform recovery anneals in flight is now well accepted.

4.11.1 Recent CTI annealing experiments

4.11.1.1 Annealing of VP & EX Centres

As the anneal was made several months after irradiation, and the devices were stored at room temperature, any EX centres would have annealed. Such centres are thought to contribute only a few percent to the parallel CTI. Substantial annealing of the VP centres is found to occur at 130 ^{o}C . After only 10 hours one typically achieves a factor 3 reduction in the parallel CTI. The serial CTI is unaffected by traps at E_C- 0.4 eV. Further beneficial annealing of the defects occurs for up to 40 hours anneal time A very slight degradation is seen to occur in parallel CTI after 100 hours anneal. Since in the CCD12 there are more parallel transfers than serial, the resulting X-ray FWHM is closely linked to the parallel CTI and therefore the energy resolution continues to improve for anneal times up to 40 hours. After this time, the serial register degrades sufficiently to dominate the spectral resolution.
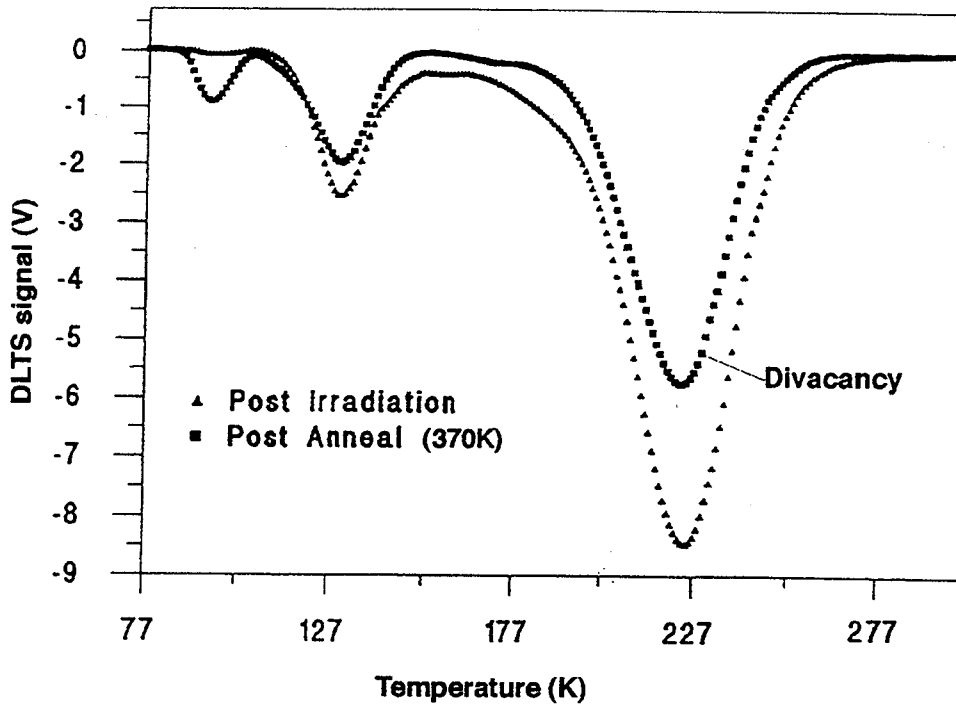
Fig. 4.42 Annealing of DLTS electron traps created by
6.25 MeV irradiation of a high resistivity n-type
silicon diode.
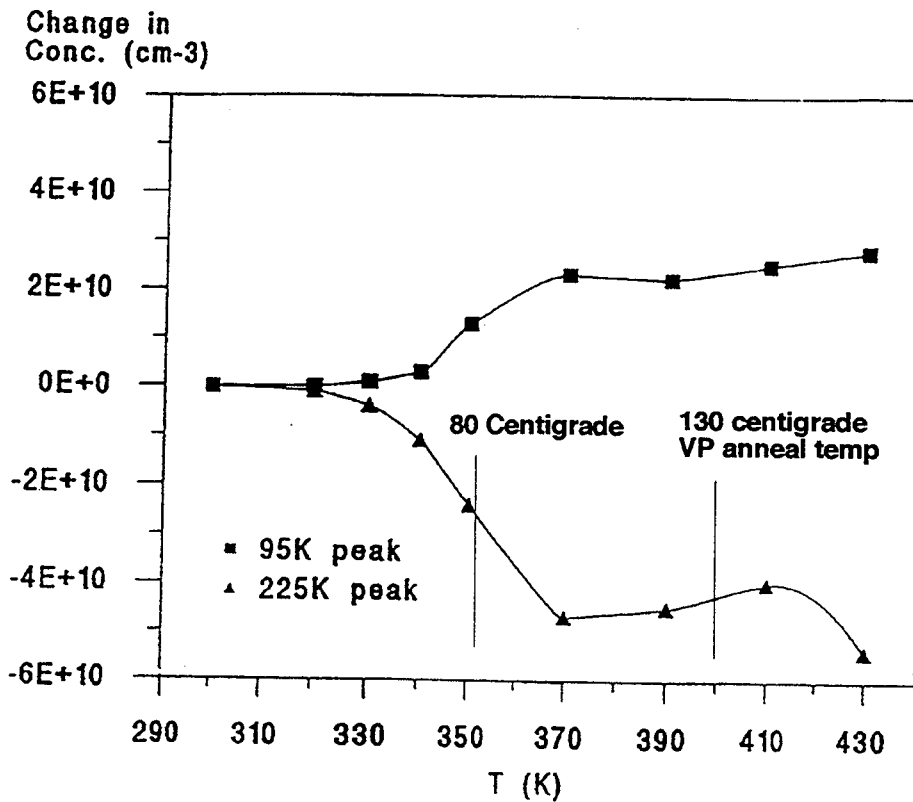
Fig. 4.43 Isochronal anneal of electron traps in high
resistivity n-type diode - cf fig. 4.42.

4.11.1.2 Generation of Defects

The effect of the E1 centre -probably VO - in the CCD is evident in the serial CTI performance below -120 °C, where the CTI and energy resolution rapidly degrade with decreasing temperature. This defect is present in all of the CCDs tested . In WO1, the devices from batch number 9012 contained a particularly high density of this defect resulting in abnormally high serial CTI at low temperatures. At the higher temperatures between -70 and -120 °C, the CTI is high in un-irradiated CCD02s at a level of (2-3)E-5 per pixel. This increases after irradiation and is due to one (or more) electron traps at around 0.3 eV below the conduction band. These are particularly effective at -90 °C and their presence is demonstrated by charge trailing (deferred charge) from X-ray events at this temperature.

Figs. 4.44, 4.45 and 4.46 show an isochronal annealing experiment in 1995 on a CCD12-6 (OE) device irradiated to 6.2E8 and 3.89E8 10 MeV equivalent protons cm^{-2} using 6.25 MeV protons in 1994. Annealing of the serial CTI (by around 40%) is seen to occur in the devices for times up to between 10-20 hours. Since the CTI is measured at -90 °C this must be due to the annealing of a trap species at around 0.3 eV below the conduction band. This annealing occurs with a time constant of typically 8 hours. Beyond 10 hours annealing the serial CTI increases. It increases typically with a time constant of 60 hours. Clearly, this result indicates the presence of two defect types with an energy level of around 0.3 eV, since the degradation would not occur for one defect given the shorter anneal time constant than reverse-anneal time constant. We designate these EM1 for the defect with 8 hour aneal time constant and EM2 for the defect with 60 hour reverse anneal behaviour. See section 5.2.3 for speculation as to the nature of these defects.

The reverse annealing behaviour is not understood. It is clear that a temperature of 130 °C is sufficient to anneal some defect types. This annealing occurs through the dissociation of traps. Thus, if VP, CP and BO centres are breaking up then one gets the release of vacancies, carbon interstitials and boron interstitials. Terminal clusters could also be breaking up. These are known to release vacancies and possibly interstitials. Release of silicon interstitials from centres like CCI and CCII is also thought to be possible (G. Davies, private communication). The vacancies and interstitial atoms released by annealing will then be captured forming new defects. Which defects form during annealing is also dependent upon the impurity concentrations in the device.

The annealing of the parallel CTI can be explained largely in terms of the break-up of the VP centre. The anneal and reverse anneal of the serial CTI requires much more work if it is to be understood.

4.11.1.3 Comparison of CCD02 and CCD12 results

The CCD02 devices received a higher radiation dose than the CCD12s and in addition have different serial and parallel channel widths. If the production of defects - type and density- by irradiation is similar in both devices then the CTI results can be correlated on the basis of fluence and the charge storage volume. This was not found to be the case when analysing the annealing results.

Considering the serial register first. The pre-anneal CTI was in keeping with the channel confinement and irradiation fluence -section 4.5. However, the anneal rate of the serial CTI was lower than measured in the CCD12s. The generation rate of the EM2 centre was in keeping with that for the CCD12 devices, but it's density was not consistent.

Considering the parallel CTI, whilst the pre-irradiation defect concentration was similar, the anneal time constant of the defects was much longer in the CCD02 devices- being <10 hours for the CCD12s and >20 hours for the CCD02s. The parallel CTI continued to improve in the CCD02s for times of up to 100 hours.
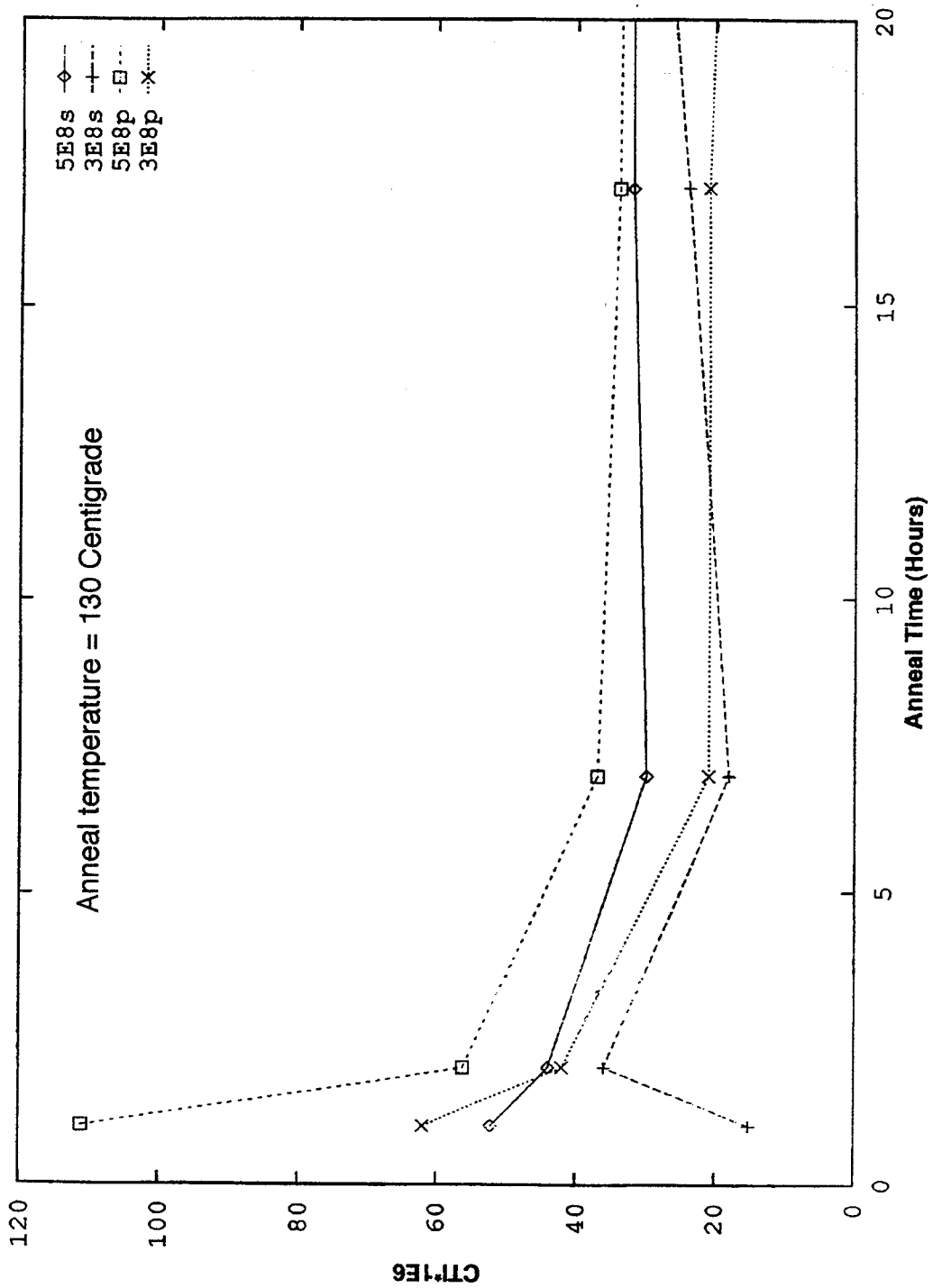
Fig 4.44 Isothermal anneal of serial and parallel CTI of CCD12-06 for 20 hours. CCD irradiated to two nominal fluences as indicated. See Table 3.4 for values. "s" means serial, and "p" means parallel.
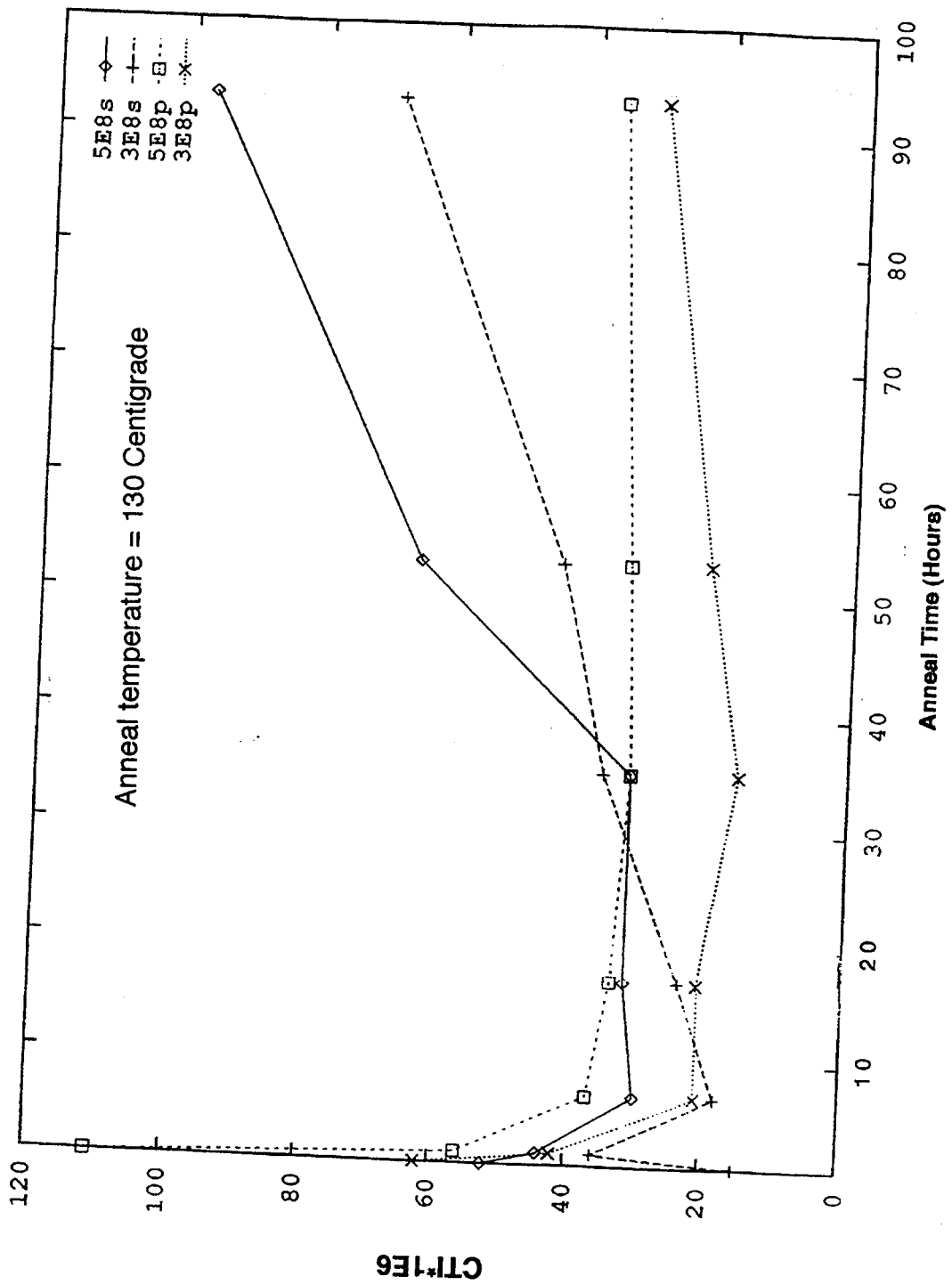
Fig 4.45 Isothermal anneal of serial and parallel CTI of CCD12-06 for 100 hours. CCD irradiated to two nominal fluences as indicated. See Table 3.4 for values. "s" means serial, and "p" means parallel.
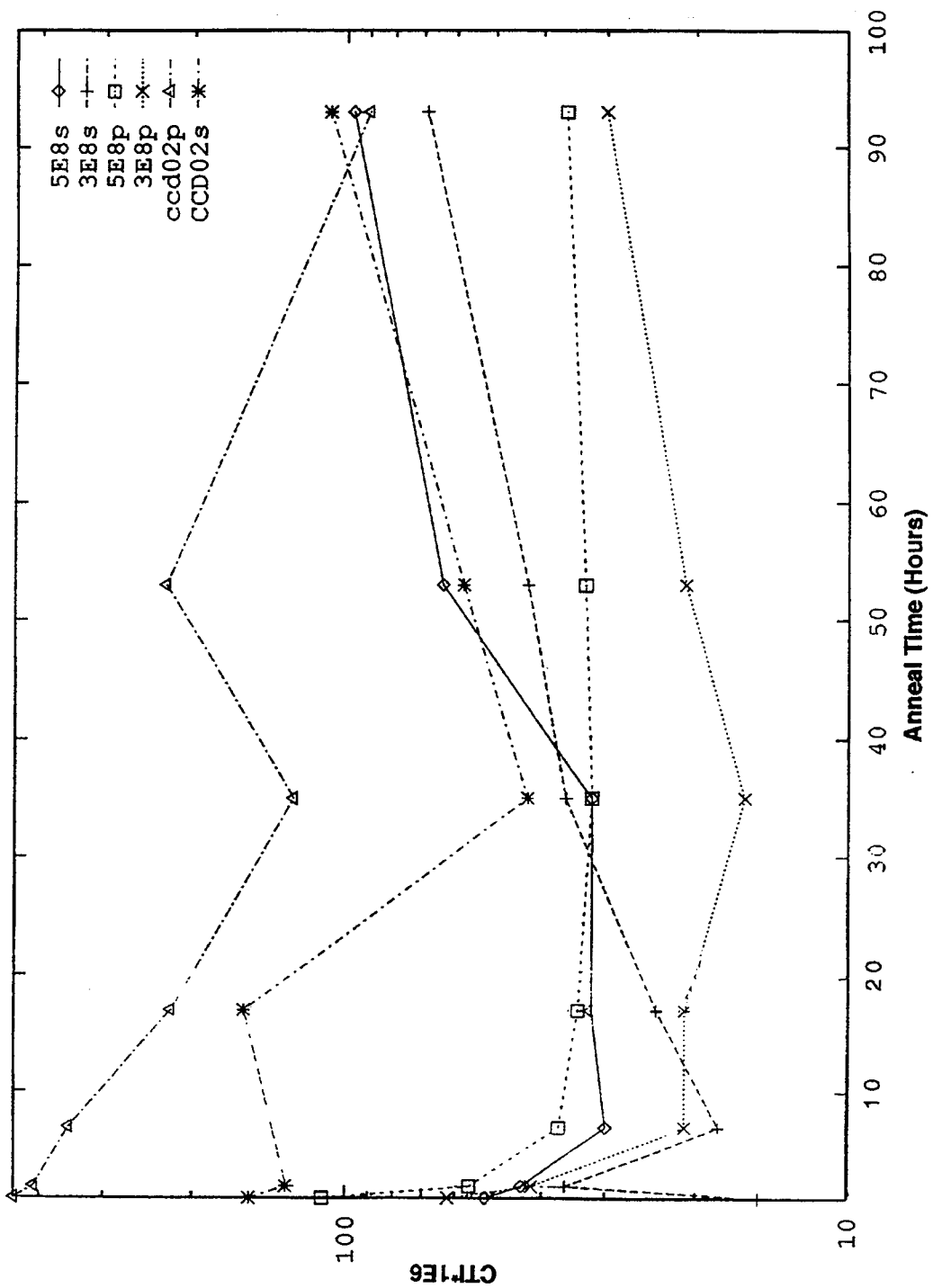
Fig. 4.46 Data as for fig. 4.45 with curves added for a
CCD02 device irradiated to about 1E9 equiv. 10 MeV
protons per square cm. See Table 3.4

The CCD02s were constructed on nominally 20 Ohm cm 20 micron thick epitaxial material, whilst the CCD12s were constructed on 100 micron thick silicon with resistivity of around 8-10 kOhm cm. This comparison of devices clearly indicates the effect of substrate material upon the defects within the CCD. Whilst the effects are comparable to a first approximation, detailed investigation indicates subtle differences in defect generation rates (with proton irradiation) leading to different admixtures of defect concentrations. These differences (the mixture between different species) combine to produce subtly different anneal rate behaviour. This conclusion necessitates a thorough verification of the optimum anneal time for any given device/silicon combination.

4.11.1.4 Recommendation for Annealing in Flight

The following recommendations may be made for the use of elevated temperature (130 $^{\circ}$C) annealing of proton damaged CCDs in space with the caveat that these are the overall conditions and that the exact condition for a given application will depend upon the exact device geometry (serial to parallel transfers) and silicon type or batch (TBD) used in the construction of devices;

a) Annealing must be considered in conjunction with the type of device under test. Annealing both reduces the density of some defects affecting parallel CTI, and increases the density of at least one trap affecting serial CTI. The number of transfers in both the serial and parallel directions must therefore be taken into account when considering the optimum anneal duration.

b) The anneal temperature of 130 $^{\circ}$C is sufficient to anneal two of the defect centres known to exist in the irradiated CCDs; the PV and EX centres.

c) In the case of the CCD12s (and the EPIC flight CCD22 devices) annealing should be maintained for a time **LESS THAN** 40 hours. An anneal time of 35 hours is recommended for use on EPIC. Prolonged annealing (>30 hours) leads to the generation of a defect around E_C-0.3 eV which degrades the serial CTI.

Further tests are required, but one would expect that this time restriction should apply to the **integrated period** for all in-flight annealing.

d) In the case of the CCD15 which possesses a larger serial register, a slightly shorter anneal time would be recommended.

e) If in-flight annealing is planned, then ground-based tests should be repeated for all new device designs to determine the optimum anneal time.

f) If devices are manufactured on new silicon stock, then it is advisable to assess the optimal anneal time for the new material.

4.11.2 Dark Current Annealing experiments

We have performed an isochronal anneal of two CCD02's irradiated in October1994. There is no annealing of the dark current spikes below 150 $^{\circ}$C. This is after 8 months of room temperature storage. Thus annealing of spikes low stability is already well advanced.

This is supported by measurements made on CCD01 devices exposed to MeV neutrons already referred to in Section 4.9.1. Both the high resistivity and low resistivity CCD were annealed at 20 $^{\circ}$C in an environmental chamber and observed over a period of one month. If the bulk dark current annealing in CCDs is similar to that seen in high resistivity diodes - see for example results from CERN's RD20 and RD2 collaborations - there are known to be four characteristic annealing time constants; 0.3 hour, 2.7 hour, 340 hour and 13055 hours. Due to the low irradiation rate of these CCD01 devices, we cannot see the first two of these time

constants. Fig. 4.47 shows the annealing of the high resistivity CCD at room temperature. Fig 4.48 shows both the high and low resistivity CCD bulk dark current annealing with a time constant of around 200 to 400 hours. A high resistivity diode is also shown for reference. This data suggests that the annealing of MeV neutron and proton bulk dark current in **depletion regions** is similar in both high resistivity float zone silicon diodes and in the epitaxial material used in CCDs.

To confirm these ideas, a CCD02 device was irradiated with 4.5 MeV alphas. After an irradiation of 10.3 hours, hot spots appeared when dark frames were acquired at room temperature. The density was several hundred per cm^2. A 15 minute isochronal anneal up to 100 ^{o}C removed all these hot spots. This is shown in fig. 4.49. The algorithm for counting spots was to treat a pixel as hot if it was greater than a specified threshold. The temperature for the onset of anneal (70 ^{o}C) is exactly the same as in the diodes described earlier. It has been calculated that 0.75% of the incident alphas create a hot spot. This is not surprising. The NIEL of alphas is about 40 times that of a 10 MeV proton. If one uses the formula due to Hopkinson 1995 relating the probability for creating an RTS pixel to the elastic NIEL , one finds that for alphas the chance for such a pixel 0.12% per particle. We believe this simple α-particle experiment gives an important insight into CCD hot spots and the nature of RTS defects and should be investigated further.

Figs 4.50 and 4.51 show dark current histograms for CCD02-5 irradiated with 6.25 MeV protons, before anneal, and at the 100 ^{o}C and 160 ^{o}C steps. These were taken during an isochronal anneal measurement. The anneals were for 15 minutes with 10 ^{o}C steps. A small amount of reverse annealing of the surface dark current has been noted. This interferes with the analysis of hot spot annealing. However, most of the hot-spots anneal at around 130 ^{o}C. Such an anneal temperature gives many potential candidates for the source of the hot-spot, although none are very deep in the band-gap. The most likely source of the current is a VP centre in the high-field region at the edges of the potential well - also see Hopkins and Hopkinson 1995.

4.12 Other radiation-induced changes in CCDs.

4.12.1 Probing for impurity effects

Given a considerable amount of unique data from ESA WO1 and related programmes, we have studied the data in an attempt to reveal impurity effects. One example is a statistical comparison between CTI degradation, under protons, of high- and low- resistivity epitaxial silicon CCDs in otherwise similar structures (usually CCD-02 or 12). From WO1 data, no statistical difference in CTI value was seen between low-resistivity and high-resistivity epitaxial CCDs. In each case, the ratios of the average CTIs at -90 ^{o}C and -130 ^{o}C were 5.5 +/-1.2.

It is clear from the results with CCD12-7 on bulk Float-Zone material that its CTI is better than similar devices on an epitaxial substrate. From this we infer that the E2 centre is produced at a much lower rate in high resistivity float zone material.

4.12.2 Random Telegraph Signals

At a proton fluence of 1E9 equivalent 10 MeV protons cm^{-2} we expect to see a number of pixels which are "flippers" - Hopkins and Hopkinson 1993. Such pixels have a dark current that jumps up and down by discrete amounts, 0.1-0.4 nA/cm^2 at 21 ^{o}C, at random intervals several times per hour. Hopkins et al. found that in a CCD-05 device, which contains about 900 Kpixels, several hundred pixels exhibited this behaviour. RTS dark current is a potentially dangerous background source, capable of interfering with CCD operation. Such pixels are known to anneal at around 100 ^{o}C and are not produced by Cobalt 60 irradiation. Calculations shown that field-emission plays some part in this behaviour because thermal emission from a single defect could not produce such large signals. Hopkins and Hopkinson (NSREC 1995) have suggested that the VP centre could be responsible for this behaviour.

From DLTS measurements on high resistivity diodes irradiated by 1 MeV neutrons (Matheson et al. 1995) and 6.25 MeV protons, a defect (EX) at around $(E_C-0.4)$ eV is found which is not produced by gammas and which anneals at about 80 °C. This leads us to speculate that this defect is responsible for the RTS behaviour and we recommend future work in this area. See also the comments in Section 4.11.2.

4.12.3 Flatband voltage

Methods for measuring flat-band voltage shifts under the clocking gates and output transistor are described by Roy (1994) and Robbins (1992). The dark current versus VSS curves showed negligible voltage shifts when comparing the unirradiated and irradiated regions of the CCD02 devices. This is as expected because they were irradiated grounded and only received an ionizing dose of about 750 rad.

4.12.4 Annealing of surface effects

Reverse annealing of surface dark current after long periods at elevated temperatures have been seen in EEV CCDs (Tudge, 1995). Such effects are small in these devices compared to Thomson CCDs (Hopkinson 1992), neverthless, reverse annealing can have a serious effect on dark current in the non-inverted mode. When operating near room temperature, the extra dark currents can swamp low-level signals and hence destroy scientific operation. Our present estimate is that, for XMM operating conditions (-90 to -130 °C) the levels of dark current are so low -see Tables 2.1 and 4.2 - that these reverse annealing effects will not be important.
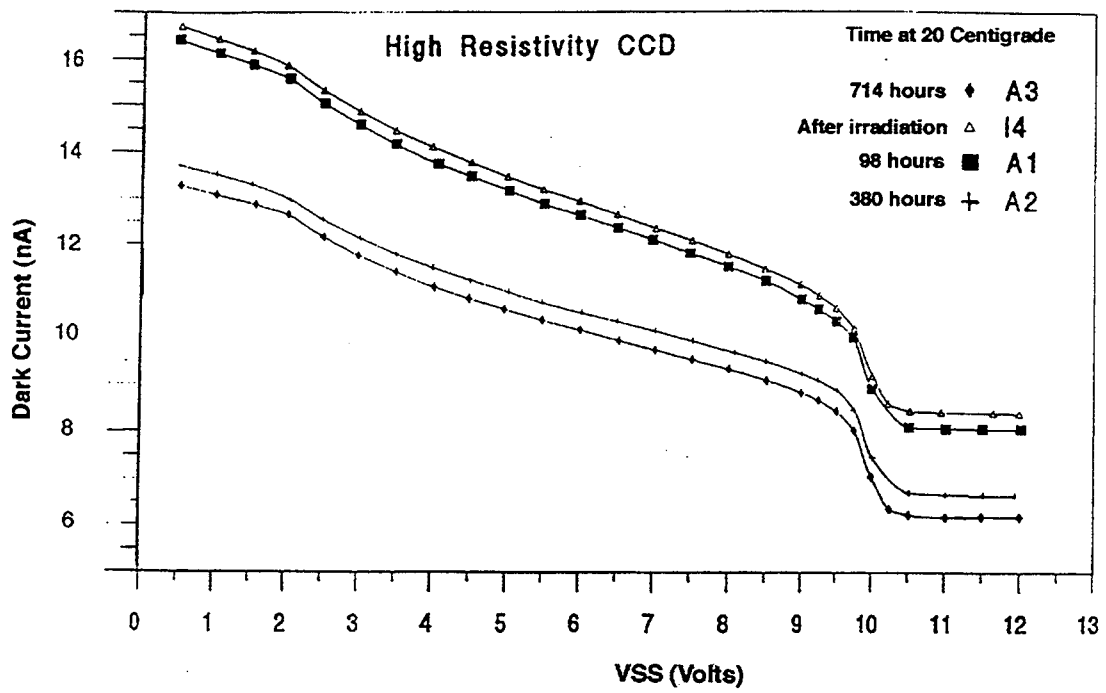
Fig. 4.47 Isothermal room temperature anneal of EEV
high resistivity CCD01 after Cf252 neutron irradiation.
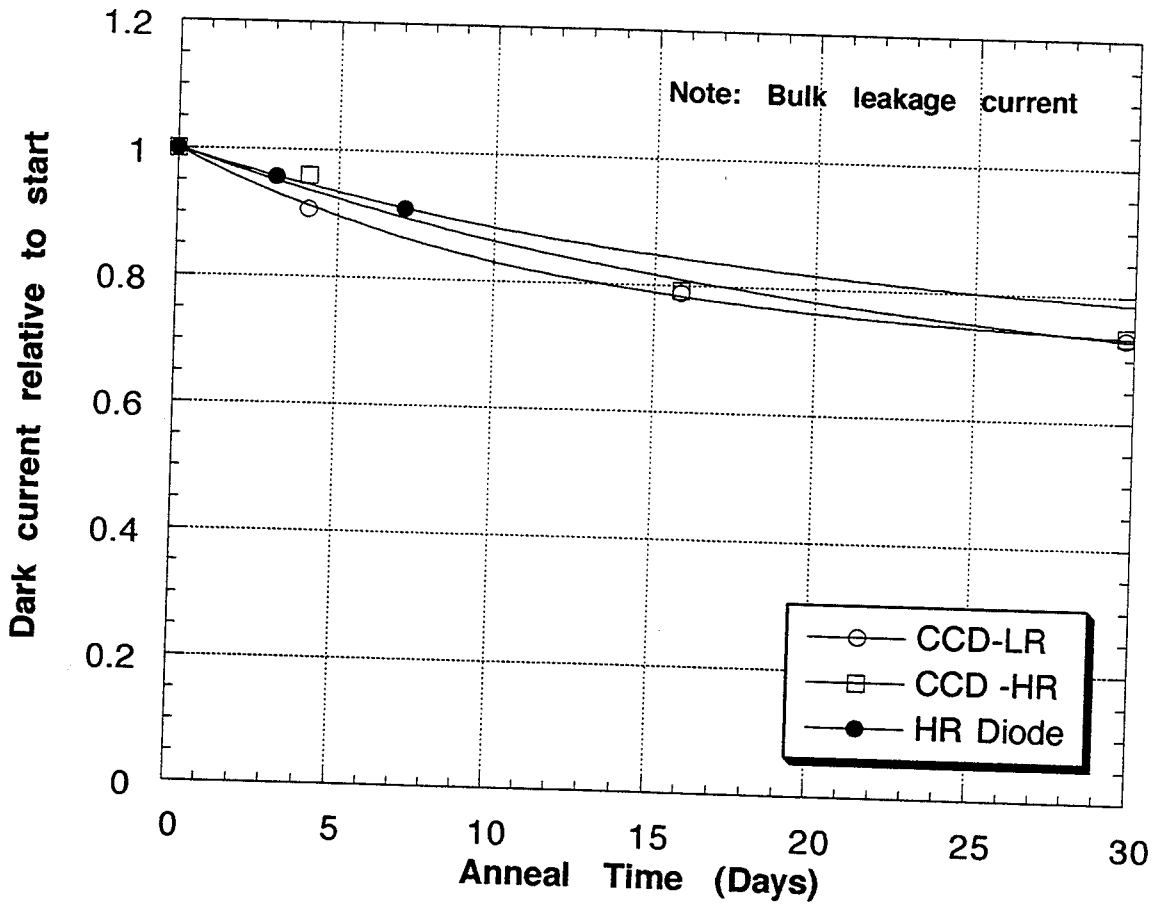
Fig. 4.48 Comparison of isothermal room temperature anneals of bulk leakage currents in EEV high resistivity (HR) and low resistivity (LR) CCD01 devices. Data for an n-type FZ high resistivity diode is also shown.

All devices irradiated with Cf252 neutrons.
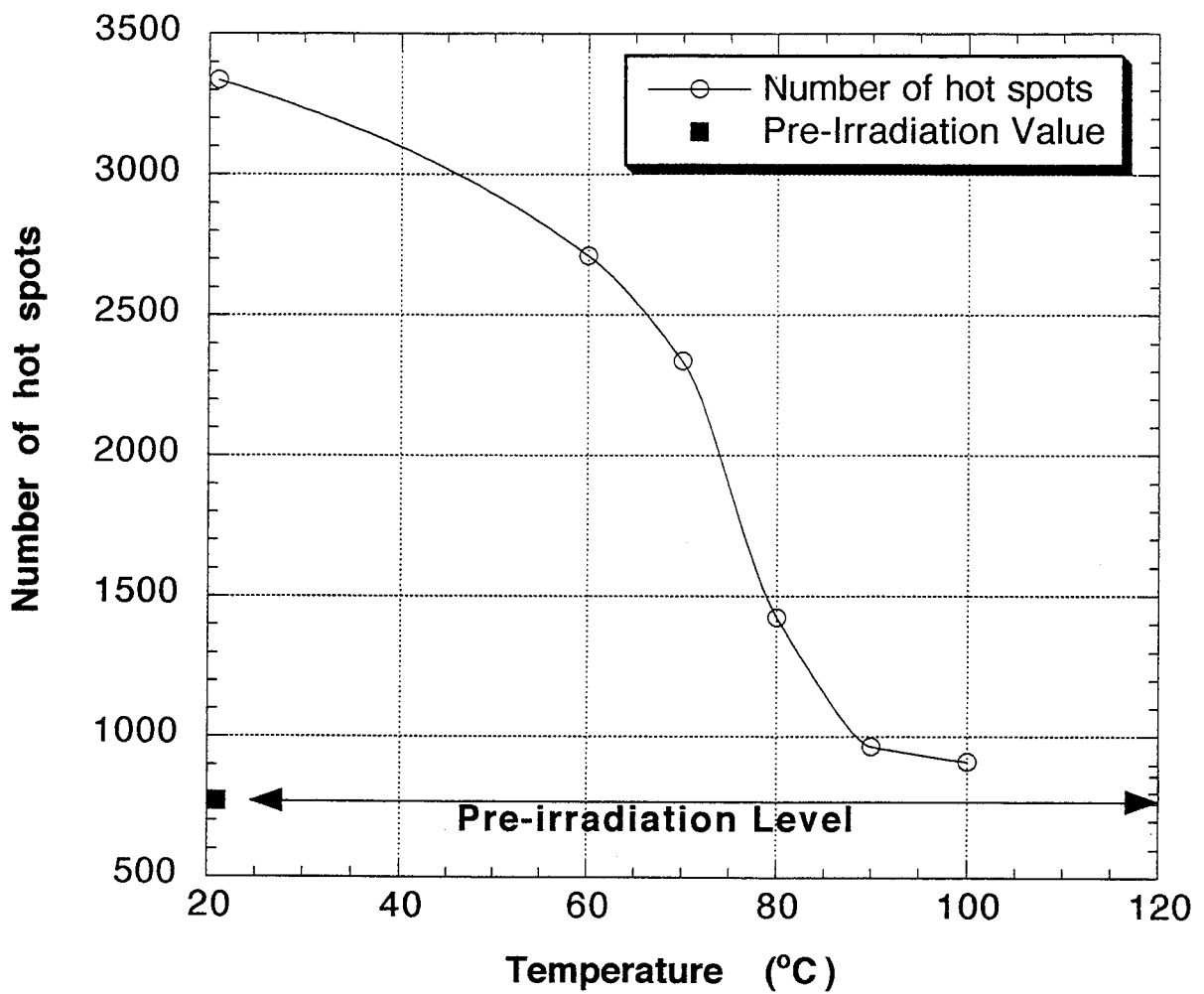
Fig. 4.49 15 minute elevated temperature isochronal anneal of CCD02 sample one day after 4.5 MeV alpha particle irradiation; "hot spot" section of the dark current histogram.
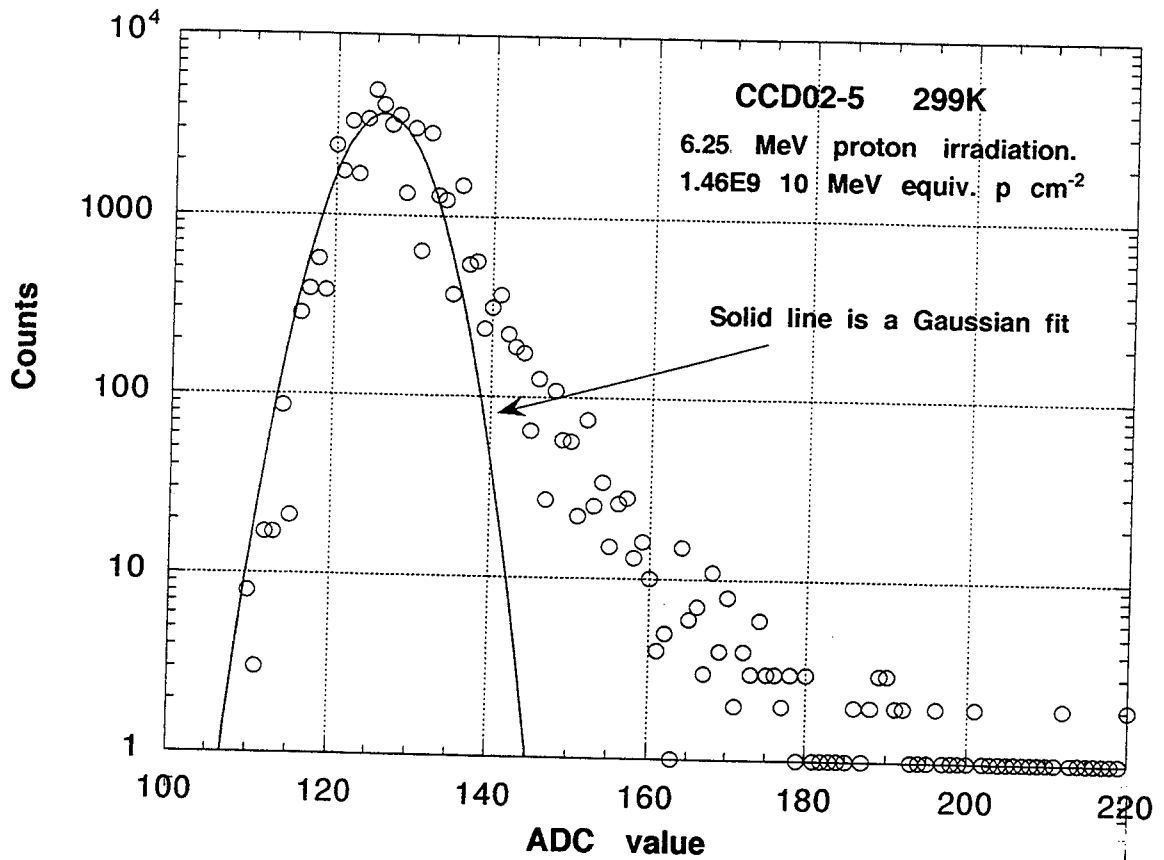
Fig. 4.50 15 minute elevated temperature isochronal anneal of CCD02 sample 5, 7 months after proton irradiation; dark current histogram before anneal.
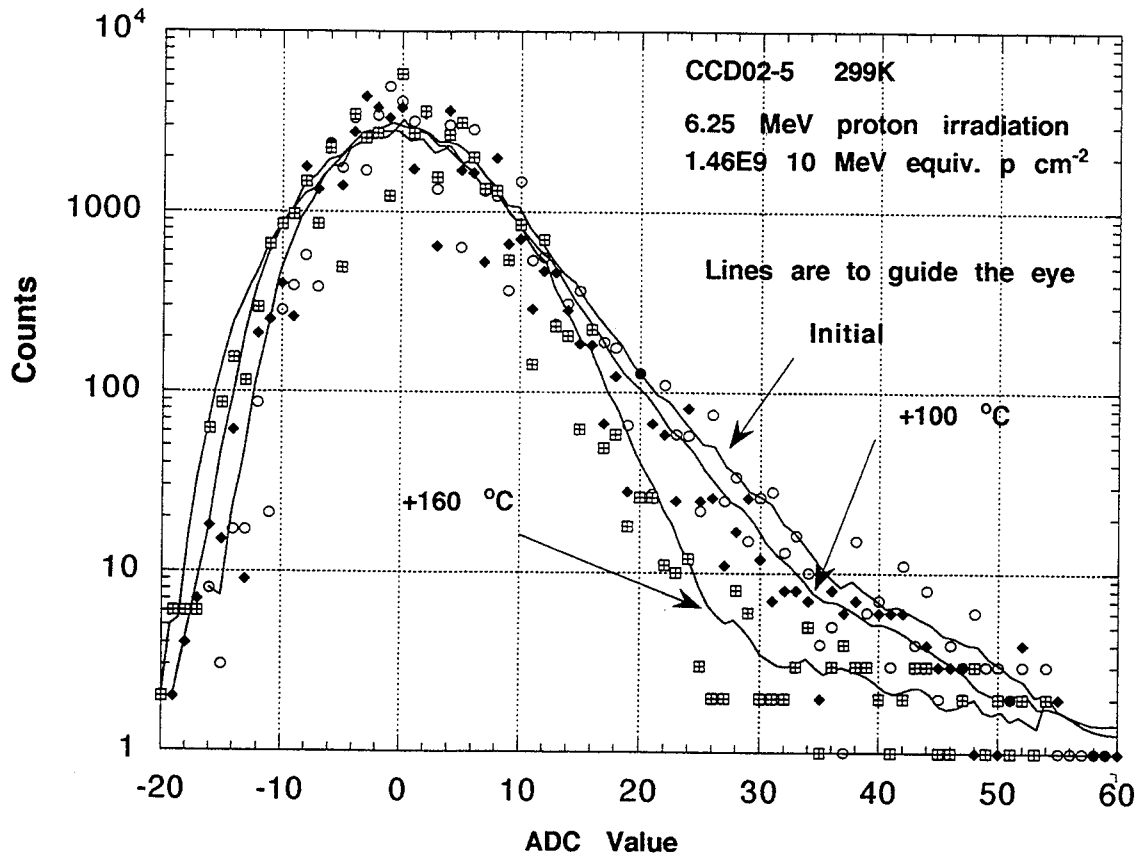
Fig. 4.51 15 minute elevated temperature isochronal anneal of CCD02 sample 5, 7 months after proton irradiation; three dark current histograms superimposed showing significant removal of hot spots between +100 and +160

5. Discussion

5.1 CCD technology, processing and defect structure

Major technical aims of the contract were the evaluation of developing technology and, in order to control those developments, the understanding of how radiation tolerance of scientific CCDs is affected by the processing techniques used. This latter aim is a broad one but is strictly necessary when we see how profound the impact of bulk defects is in the CCD buried channel at low light level. It is thus necessary to adapt the existing knowledge of defect formation and action in silicon to the special conditions existing in the CCD depletion region. Our discussion thus ranges from processing technology to defect kinetics which are relevant to CCDs.

The active region of an EEV CCD is formed in silicon grown epitaxially from silane. A medium p-type doping level of boron gives resistivity in the 20 to 8000 ohm-cm region. The surface layer is implanted with a pre-planned concentration of phosphorus to form a buried n-type channel. The active regions which concern us are "microvolumes" within this layer, formed as depletion regions (potential wells) by fields from the relevant gate electrodes.

Some hypotheses will be drawn in the next section as to the defect picture but (as indicated in Section 5.3.2) it should certainly be assumed that the high-temperature processing of CCDs may make the actual state of affairs more complex than that given in our hypothetical cases - see for example Claeys et al. 1994.

5.2 Defect Kinetic Modelling

We first refer to the body of work done on simple diodes made from FZ silicon, which are test structures from wafers containing microstrip particle detectors, the work being done as part of CERN's RD20 programme. Brunel carried out DLTS measurements on diodes made from high-resistivity (4000 ohm-cm n-type FZ silicon Matheson et al.1995) The diodes were irradiated with gamma rays and Californium neutrons and some experiments have also been performed with 6.25 MeV protons. DLTS revealed the concentrations and energy level of trapping centres. Such measurements together with defect kinetics modelling and device modelling have helped to provide a better understanding of the unique effects which occur in this special material, including carrier removal, type inversion and room-temperature annealing. These effects are not important in low-resistivity bulk n-type silicon or in the buried channels of CCDs which have channels heavily implanted with phosphorus. However, the defect kinetics model can be applied to CCDs to provide an insight into the defect(s) responsible for bulk effects and to understand our failure to observe any significant room temperature annealing of proton damage to CTI. The situation in the diodes is similar to that occurring in the depletion region of an operating CCD and hence is applicable to bulk dark current models for CCDs. Our results (section 4.9) agree with such an idea.

5.2.1 Parameters of the material before irradiation

In order to model the behaviour of the CCD active regions after irradiation, we require reasonable estimates of the impurity levels in the material. The concentration of an impurity X will be written as [X] following the convention in Davies et.al.1987a, 1987b. In the buried channel, the phosphorus concentration is typically $[P] = 10^{16}$ cm^{-3} . Our current knowledge of the carbon and oxygen concentrations needs to be significantly improved. At present they are no more than an educated guess. The buried channel and bulk have very different impurity concentrations and will behave differently under irradiation. Carbon is likely to be at different levels in epitaxial and FZ material. This might produce differences between CCDs fabricated on bulk or epitaxial high-resistivity wafers. However, because the phosphorus doping in the buried channel is similar in each type, radiation effects in the channel region (mainly degradation of the the charge transfer efficiency) are likely to be similar.

Our best estimate of the parameters of the materials is given in Table 5.1. This is based upon private discussions, DLTS measurements and a single SIMS measurement of an EEV processed wafer.

Table 5.1 Estimated concentrations of impurities in the CCD   (Units are cm^{-3})

Impurity	Low Res Epitaxial	High Res Epitaxial	High Res FZ
Phosphorus See note1	10^{16}	10^{16}	10^{16}
Boron	10^{15}	10^{13}	10^{12}
Carbon	10^{16} Note 3	10^{16} Note 2	Few 10^{15}
Oxygen	10^{17} Note 3	10^{17} Note 2	Few 10^{15}

Note1: In the buried channel only.

Note2:   High resistivity epitaxial material is normally   thicker (100 μm). We would expect these numbers to be upper limits. Actual values in the buried channel could be much lower. We believe the epitaxial layer is autodoped from the substrate. On thicker material, one would expect lower autodoping. See Note3 regarding the carbon level.

Note3: Warning, from a single SIMS analysis. The carbon level is very close to the measurement limit of the SIMS equipment and as such its value should be treated with caution.

It is also useful to list some potential electron traps. See Kimmerling 1989. For simplicity, metastability is not dicussed here. These are given in Table 5.2.

Table 5.1 Likely electron traps in n-channel CCDs

Defect	E_c-E_t (eV)	Anneal Temp ($^{\circ}$C)
V P	0.4	130
VO	0.17	
CC	0.17	225
C P	0.21-0.30	125
BO	0.26	150-200
V V -divacancy	0.4	
EX	0.4	RT-80

5.2.2 Defect Kinetics

In order to understand the data it is important to have a model for the production of defects formed by radiation damage. The model utilised in this report is due to Davies et al. (1987a, 1987b), and has been used successfully to explain photoluminescence data on samples irradiated by electrons. Work for CERN's RD20 collaboration (Watts 1995; McEvoy 1995) has extended the model to MeV neutron and proton irradiation .

There are three phases to the formation of defects at room temperature :-

Phase 1 :

Generation by radiation of vacancies (V), silicon interstitials (I) and divacancies (V_2) due to atomic displacements. The vacancies and interstitial silicon atoms are mobile for temperatures above 100K and 4K respectively. The divacancy is immobile and does not anneal out until 560K. For electron irradiation, the V and V_2 generation rates depend upon the energy.

For electron energies above 1 MeV, these rates are about $0.1 cm^{-1}$ and 0.02 cm^{-1} respectively. Thus the interstitial (I) generation rate can be equated to the vacancy rate plus

twice the V_2 rate, which is about 0.14 cm^{-1}. There is strong evidence that divacancies are produced by pairing of two single vacancies produced within the same collision cascade - not by the pairing of two vacancies from two separate electrons. The first vacancy is produced by an electron-atom collision, the second by a recoiling atom. Before combining, the two vacancies migrate less than 50 nm.

Fast neutrons and megavolt protons have a much greater damage creation power, or NIEL, than electrons and hence produce vacancies and interstitials with a higher introduction rate (several cm^{-1}). In addition, a large number of terminal clusters are formed which contain significant numbers of divacancies and more complicated intrinsic silicon defects. The terminal clusters created by the faster knock-on silicon atoms consist of a region containing much lattice damage. The cluster is localised to a region of about 10nm long and area 5 by 5 nm^2. There will be few impurity atoms in this region and th defects are thus V_2, more complicated multi-vacancy configurations and interstitial atoms. Vacancies may then evaporate away from the cluster as it anneals, creating a long-lived localised source for vacancies as well as the general diffusion of radiation induced vacancies and interstitials. Many more divacancies are formed than with MeV electron irradiation. Continuing the reasoning used above, divacancies are formed directly within a single displacement cascade. Typical dimensions of terminal clusters and primary knock-on atom (PKA) tracks are 10 nm and 100 nm repectively. Thus one expects a significant number of vacancies to pair together once the spacing between impurity atoms becomes greater than 100 nm.

Phase 2 :

The radiation induced vacancies and interstitials "diffuse" through the crystal. Various reactions occur until the vacancies and interstitials disappear. Reaction rates are controlled by the concentration of impurities/defects and their capture radii. Some typical reactions are:-

$I + C_s \rightarrow C_i$	(Transient)
$I + B_s \rightarrow B_i$	(Transient)
$C_i + C_s \rightarrow CC$	
$C_i + O_i \rightarrow CO$	
$B_i + C_s \rightarrow BC$	
$B_i + O_i \rightarrow BO$	
$V + O \rightarrow VO$	(Si-A centre)
$V + P \rightarrow VP$	(Si-E Centre)
$V + VO \rightarrow V_2O$	
$I + V \rightarrow \Phi$	(Φ is a self-repaired site)
$I + V_2 \rightarrow V$	
$V + V \rightarrow V_2$	
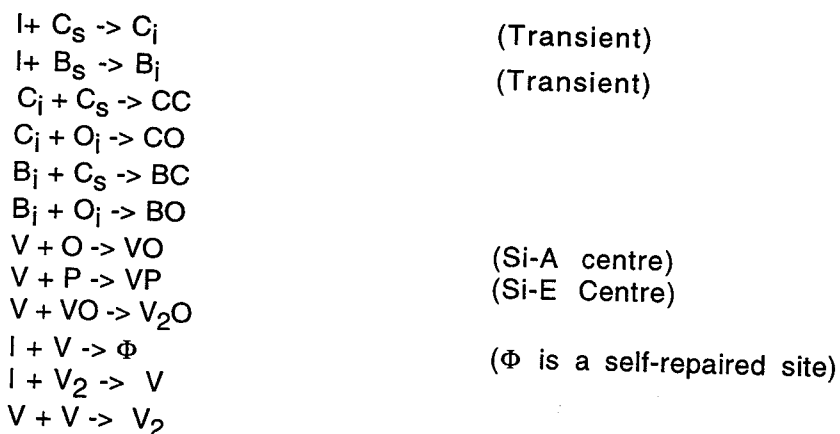
Divacancies (V_2) are also produced directly, as described earlier.

The probability for a reaction in the above list, is determined by the concentrations of all relevant reactants weighted by their capture radii, R. It is not necessary to know the actual values of the capture radii, only ratios are required. These are reasonably well known, based on photoluminescence and optical absorption measurements. For example,

$R(V,P)/R(V,O) = 14.3$, $R(C_i,C_s)/R(C_i,O)$

$= 3.1$, $R(C_i,P)/R(C_i,C_s) = 10$.

For example, taking $[O] = 5E16$ cm^{-3}, one can calculate the probability for forming Si-A and Si-E centres in the buried channel of the CCD . The oxygen concentration has been chosen as the minimum level that the SIMS technique can detect. Section 2.3.2 discusses what the oxygen concentration is likely to be in the channel.

Thus $P(V,O) \approx [O]/([O] + 14.3^*[P]) = 0.26$ and
$P(V,P) \approx [P]/([P] + 0.07^*[O]) = 0.74 = 1 - P(V,O)$

To convert these to introduction rates, one needs to multiply these probabilities by the introduction rate for the vacancy. This depends upon the incident particle and its energy. In the absence of data, scaling using NIEL can be used, but such calculations should be treated with caution.

Phase 3:

Room temperature annealing of the damage after irradiation. This is important for neutron and low energy proton damage where clusters of defects tend to break up but may do so quite slowly. In addition, interstitial carbon and boron atoms are mobile at room temperature and need to be considered. Silicon interstitials react with substitutional carbon and boron to produce these species. The latter react with oxygen and carbon to form C C, C O, BO and BC defects. The time constant for these reactions depends mainly on the concentrations of carbon and oxygen. In high-resistivity FZ material carbon reactions have been seen to occur over a two-week period at room temperature. Finally, interfaces (eg. Si/SiO$_2$, epitaxial/substrate boundaries) act as sinks for mobile radiation induced defects but their exact roles are not evaluated here, although they could be significant in close-spaced CCD structures.

5.2.3 Conclusions

Defect kinetics is very different in the n-type buried channel and p-type bulk. In the buried channel, the high phosphorus concentration will suppress the formation of divacancies and more complicated cluster regions. The main defect formed will be the VP centre. Thus the charge transfer efficiency will be degraded mainly by the VP centre which anneals at 135 °C. If this is so, one would not expect to see any room temperature annealing of the CTI. Cluster damage is more likely to occur in the p-type region, which is not so highly doped. This would manifest itself in the radiation-induced dark current. It is possible that FZ material might behave differently to the epitaxial material due to a different carbon concentration. Cluster damage is known to anneal at room temperature. Thus, unlike the case of CTI annealing, changes in dark current are likely if a device were to be left at room temperature over a long period of time and this effect has indeed been observed. Such an effect, of course, is of minor importance if the CCD is kept permanently below room temperature, However, most operational schemes allow some warmup periods. For defects in the CCD channel region, field-enhanced emission also needs to be considered, because of the high fields at the edge of potential wells.

The CTI data given in the WOI report indicates that the ratio of VP to VV defect is about 6 to 1. This data also shows no room temperature annealing of the CTI. Room temperature annealing of dark current over several months was not measured in WO1 but has been seen by Hopkinson. The model of defect production given above fits in well with current data and can be used to guide further data analysis. CP and BO are potential candidates for the 0.3 eV defect. Differing boron and carbon levels in FZ material could explain why degradation of the CTI is less in this material.

5.3 Impurities in epitaxial silicon

5.3.1 As-grown

The resistivity of the epitaxial layer as a function of depth is obtained by etchback of the as-grown wafers and four-point probe measurement. The epitaxial layers in wafers used for EPIC are boron doped and have a resistivity of about 8000 ohm-cm at the surface, decreasing gradually to about 1000 ohm-cm when 20 μm from the epi/substrate interface. The region within 5 μm of the substrate is heavily autodoped with boron and other impurities from the

crucible-grown substrate. The epitaxial layers of the CCD02 wafer investigated in WO2 was 20 μm thick, was boron doped and had a resistivity of 20 ohm-cm.

5.3.2 Fully-processed CCD

a. Stages of process

Before the patterning of CCD wafers, an important proprietary processing step taken by most manufacturers is intrinsic gettering. The object of this step is to remove deep-level , mainly metallic impurities from the active surface region resulting in a "denuded zone". In the present study, the active microvolumes in which we are interested are very near to the silicon upper surface and therefore very sensitive to the multiple surface processing steps used in the formation of the CCD structure. Although the question of uncontrolled impurities in this region has not been widely studied, we can state that the silicon surface is in contact with gaseous oxygen or oxide layers for a total of several hours at temperatures near to a value of half the melting point of silicon.

(i) Junction and channel formation involves the growth of oxide masks followed by implantation or diffusion of n-type layers.
(ii) The surface of the wafer is oxidized using commercially confidential schedules but always at temperatures between 900 and 1100 $^{\circ}$C to give the gate oxide.
(iii) A nitride layer is deposited over the thermal oxide by chemical vapour deposition (CVD), using the pyrolysis of a mixture of ammonia and silane, both rich in hydrogen
(iv) The silicon gate electrodes are grown in three stages by CVD, followed by activation bakes for the polysilicon and oxidation for interlayer isolation.
(v) Final protection includes the deposition of antiscratch layers and opaque shield layers. The baking on of polyimide in the store areas may supply a reservoir of hydrogen.

b. Oxygen

There is conflicting evidence as to whether extensive exposure to an oxidizing ambient leads to a rise in the as-grown oxygen concentration away from the surface. Li and co-workers (1992) used SIMS etchback to reveal a deep (3 mm) oxygen diffused layer, produced by a specific, intensive thermal oxidation step. Other workers (Struder, Poole, private communication) maintain that any oxygen profile produced in CCDs is no more than 10 nm deep. Despite this uncertainty, the question of oxygen concentration is important to our kinetic picture. We can compute the order of magnitude of concentration from the known transport constants for oxygen in silicon. The solid solubility of oxygen in silicon at the surface is 3E18 cm^{-3} at 1100 $^{\circ}$C. As an interstitial impurity, oxygen will diffuse rapidly. The diffusion constant of oxygen in silicon at 1100 $^{\circ}$C is 1 mm/hr, which is an order of magnitude above that for phosphorus. After the intensive history of contact with oxygen described above, the oxygen diffusion front is thus probably deeper than that which would be expected for a phosphorus diffusion. The oxygen diffusion concentration profile, is likely to be an error function (erfc), starting at about 3E18 cm^{-3} at the surface, and may fall to 1E15 cm^{-3} within 2 to 5 mm. It will be advisable for ESA and CCD manufacturers to obtain the actual values using commercially available SIMS analysis services. We have had an EEV wafer analysed by SIMS to get a first indication of oxygen and carbon levels in the material. Fig 5.1 shows the SIMS analysis. We had expected a low carbon concentration in the expitaxial material. This appears not to be so, although the carbon concentration is close to the SIMS measurement limit and as such should be treated with caution. We believe that carbon levels in the epitaxial layer are affected by autodoping from the CZ substrate. Fig 5.1 shows that the oxygen and carbon concentrations in the buried channel are about 2 10^{17} and 4 10^{16} cm^{-3} respectively. One can also see a zone denuded of oxygen at the surface. Oxygen precipitates are evident in the substrate.

EVANS EUROPA
SPECIALISTS IN MATERIALS CHARACTERIZATION
CASCADE SCIENTIFIC LTD.

10^{20}

10^{19}

10^{18}

Concentration (atoms/cc)

Oxygen

Oxygen precipitates

Denuded zone

Substrate starts about here

10^{17} O (FZ) - Detection limit

Carbon

C (FZ) - Detection limit

10^{16}

0   10   20   30   40   50

Depth (microns)
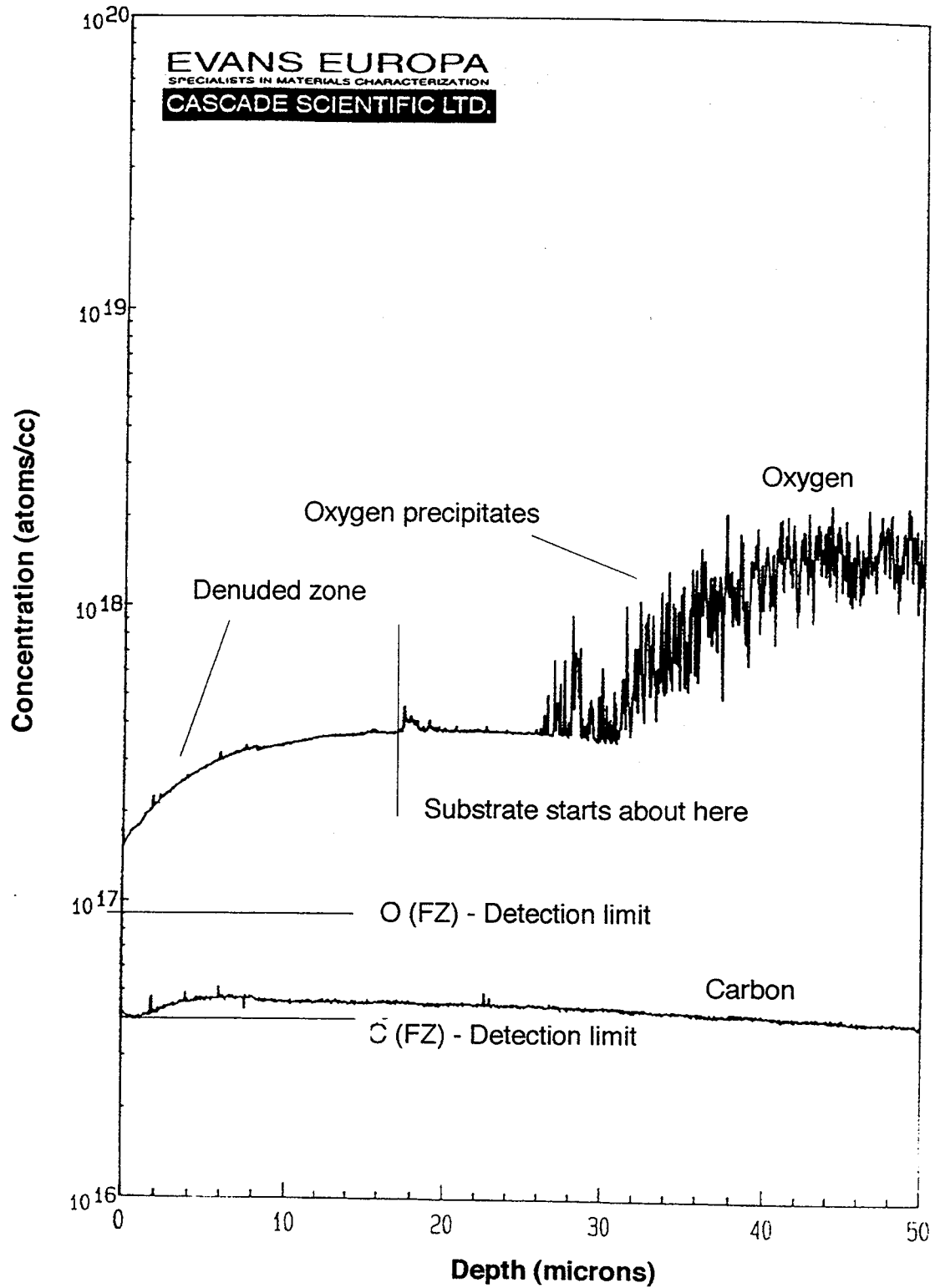
Fig. 5.1 SIMS analysis of a processed EEV CCD wafer
having a typical epitaxial layer (nominal 20 microns).
To avoid thick gate layers, the ion etch took place near
to the wafer's edge. CAMECA machine of EVANS/EUROPE
Uxbridge.

We have established that the oxygen environment in the active region of a CCD is quite dissimilar to that in crucible-grown silicon, which, if gettering has not been performed, has a flat profile at about 1E18 cm^{-3}. In parts of the active microvolumes in CCDs, the environment may be similar to that in float-zone silicon, which Matheson et al.(1995) measured to be about 5E15 cm^{-3} by DLTS measurements on gamma-irradiated FZ diodes. In CCDs, it is clear that the concentration of oxygen is sufficient to compete for vacancies - see section 5.2.2 - although the resulting concentration of VO centres may have a gradient over the active region in the z direction and the competition for vacancies provided by atoms of implanted phosphorus is severe. A better analysis of impurity concentrations in the epitaxial material would be possible if suitable test structures were added to CCD process masks.

c. Carbon

The diffusion constant for carbon is similar to that for oxygen. Thus, given available carbon at the silicon surface during processing, similar dissolution could take place and diffusion profiles form as noted in Section b. However, except possibly during CVD deposition stages, it is unlikely that unreduced carbon is present. Thus carbon will probably not figure in defects related to surface processing. The carbon concentration in float-zone silicon is around 0.5 to 1E16 cm^{-3}. DLTS measurements on irradiated diodes can be used to estimate both the oxygen and carbon levels in an expitaxial layer, so that we are actively pursuing the fabrication of suitable test structures in the pursuit of improved estimates of these impurity concentrations.

d. Displacements and other impurities

While it is usually assumed that the intense damage (amorphization) produced by the channel implant has been completely wiped out by the subsequent high-temperature processing, it should be remembered that, in some samples, clusters of very stable defects could remain and interact with vacancies and interstitials produced by proton irradiation.

5.4 Summary of defect engineering ideas

Our discussion in Section 5.2 on defect engineering can be summarized as follows:

Defect formation in the buried channel of EEV CCDs is dominated by the phosphorus doping. One might expect that the epitaxial silicon would contain a fairly low concentration of oxygen and carbon, having been deposited pyrolytically from pure chlorosilane vapours in an atmosphere free of oxygen. However, the SIMS measurement indicates quite high carbon and oxygen levels for a 20 μm epitaxial substrate. For thicker epitaxial layers, this autodoping is likely to produce much lower oxygen and carbon levels in the buried channel. Thus, from first principles, it is likely that the predominant reaction of vacancies (those which are not claimed by well-known "sinks" such as interstitials, the surface and dislocations) is with implanted phosphorus.

This predominance is confirmed :

(a)   by the lack of recovery in the CTI damage when irradiated at room temperature or at -90°C and then stood at room temperature,

b)   by the temperature dependence of the CTI damage, confirming a trap energy of about $(E_c - 0.4)$ eV for the dominant defect,

c)   by the annealing of 90 percent of damage at temperatures near 150°C (WO1).

This situation is inconvenient but may also be avoidable. If oxygen were introduced into the implant region in amounts larger than the implanted phosphorus, then the damage to CTI of a cooled CCD could be reduced. The effect of oxygen is to capture vacancies, so that the trap

energy ((Ec-0.17) eV for the VO centre) is too small for serious electron trapping/emission effects to take place at the CCD operating temperature.

Although oxygen can be diffused deeply into silicon at 1000°C, the amounts introduced during CCD oxidative process steps do not seem to be sufficient to bring about this improved state of affairs . Experiments which suggest this view include:

(a)   the reaction radius of the VO centre is one-tenth of that of the VP centre, (Su1990).

(b)   defect engineering experiments in which Li et al. (1992) found that the radiation hardening of high-resistivity silicon detectors by the diffusion of oxygen and carbon was generally unsuccessful.

There are, however, more radical methods for defect engineering of CCDs available. For example, the oxygen concentration could be greatly increased by ion implantation. Doping of the melt or epitaxial layer during growth with various elements, including germanium and tin (isoelectronic with silicon) may provide competition with the phosphorus. Topsil have recently manufactured Si/Ge high resistivity wafers as part of a programme of work aimed at making more radiation tolerant microstrip detectors for the LHC experiments at CERN (Lemeilleur, private communication). Oxygen doping is possible only up to the point at which the solubility limit is passed. After this level, precipitation invalidates the approach. It remains to be seen whether there is a suitable window between the two thresholds of oxygen concentration, namely the lower one of useful competition with phosphorus and the higher one of precipitation during heat treatment.

6. Data Delivered

Images of dark frames, three per device at three temperatures;-30 $^{\circ}$C, -50 $^{\circ}$C and -70 $^{\circ}$C. The data is in binary format on a CD-ROM. Text files contain an index of the data and decoding instructions. The number of images is approximately 60.

7. Tools for in-flight prediction and design tradeoffs

7.1   Solar flares and CCD damage

In the WO1 report, we calculated that a major flare which took place in October 1989 would cause damage behind 10 mm Al of about 5E8 cm^{-2} equivalent 10 MeV protons, This is sufficient to give a step degradation of CTI in a CCD02 of the order of 1E-4 at -90 ^oC. This is a serious amount of damage for an X-ray camera. The flare protons arrive in a relatively short pulse of a few hours whereas Van Allen Belt proton damage is received daily and will provide a steadily rising increase of CTI with time. Electrons and bremsstrahlung will be present but it is unlikely that their effects will be as large as that of the protons.

It is beyond the scope of this project to make precise recommendations about spacecraft shielding or orbit choice but we have been encouraged to describe, for the system engineers, the calculation tools that can derived from this project. We do this by means of a worked example for a temperature of -90 ^oC and typical x-ray data.

7.2   A worked example

7.2.1   Input radiation environment

As a working assumption, we use a lifetime fluence for the device under study of 5E8 equivalent 10-MeV protons cm^{-2}. This equivalence should be calculated on the basis of Non-Ionising Energy Loss (NIEL), **NOT** ionising dose (Rads). The method described below work for radiation delivered at temperatures between room temperature and -110 ^oC. One also needs to know the total ionising dose from all sources - protons, electrons and bremsstrahlung. For illustration we assume a value of 1.5 krad.

7.2.2   Bulk damage - estimate of CTI changes

The CCD type, channel dimensions etc., have to be specified. We will assume that the readout conditions are slow-scan as used by the XMM camera. There is enough information in this report to extrapolate to other readout conditions but the process is complex. Taking a CCD12(OE) epitaxial device at -90 ^oC (Table 1.1), then from Figs. 4.19, 4.22 and Tables 4.3 and 4.4, the CTI Damage Constant for **worst case** conditions of just 10 hits per CCD is 1.3 10^{-13} and 0.2 10^{-13} cm^2. Thus for signals of 1600 electrons and above:-

ΔCTI(parallel) is: 5E8*1.3E-13 = 6.5E-5 and
ΔCTI(serial) is: 5E8*0.2E-13 = 1.0E-5.

The curves of fig 4.3 and 4.4 give some guide to the best CTI value that one should achieve with high hit rates. It would be unwise to use the curves of Fig 4.1 for intermediate rates. An improvement of a factor 3 in ΔCTI(parallel) should be obtained at high hit rates.

The use of a charge injection pulse, or "bright row", as described in Section 4.8 would improve the DCTI(parallel) by a factor of 1.5 to 2.0.

For signal sizes below 1600 electrons (6 KeV), the CTI is increased further. This is shown in Fig 4.13 and Section 4.4.
A final check concerns statistical fluctuations due to the G-factor (Section 4.3). Assume that there are 150 hits on the whole of the CCD area, and that there are no significant background hits - either external or from dark current. We will take a readout rate of 20 μs. For the readout register, there will be a hit every 2773 pixels. This corresponds to a time of 55 ms. From Fig. 4.9 this corresponds to a "critical temperature" of 215K, or -60 ^oC. Thus one should operate at temperatures below T_c -10 ^oC, i.e. -70 ^oC.

We have done the above exercise for a range of temperatures and this is shown in Table 7.1.

Table 7.1 Estimates of dark current and CTI after exposure to a radiation environment of 5 10^8 10 MeV equiv. protons and 1.5 krad for a CCD12(OE) on epitaxial material. For signal sizes of 1600 electrons and above.

Hit rate (photons cm^{-2} s^{-1})	Temperature ($^{\circ}$C)	DCTI (parallel) (10^{-6})	Dark Current (e/pixel/s)
Very low e.g. 10	-110	26.5	1.15e-4
	-90	65	0.013
	-70	85	0.73
	-50	-- *	22
	-30	-- *	409
High e.g. 250 +	-110	16	As above
	-90	21	
	-70	42	

*Indeterminate values due to thermal generation of background charge much higher than the photon induced charge.

7.2.3 Estimate of dark current changes.

The devices tested in this project were NOT able to operate in inversion mode. The majority of the dark current increase is from the surface. However, the behaviour of the bulk current (depletion region), has been determined (Section 4.9), and the prediction formulae can be applied to inversion mode CCDs. From the data in this report we can write two simple expressions for the dark current damage constants:-

Dark Current (Bulk) - use 10 MeV equiv. proton fluence.

DIB = 0.04*exp(-6532/T)*(NIEL Particle/NIEL 10 MeV protons)

This has units of nA/particle/μm. The temperature T (Kelvin) dependence is 0.56 eV. To get the dark current in nA/cm^2, you multiply this by the fluence, and the depletion thickness of the CCD in μm. For 5E8 cm^{-2} 10 MeV equiv. protons, and estimating a 25 μm depletion in the CCD12 device, one arrives at 9.5E-5 nA/cm^2 at -50 $^{\circ}$C

Dark Current (Surface) - use ionising dose in krad.

DIS = 1.95E12*exp(-8151/T)

This has units of nA/cm^2/krad.The temperature dependence is 0.70eV. This dependence is based upon data from Roy et al. 1989 and is consistent the WO2 dark current data given in section 4.9.2.1. To get the dark current in nA/cm^2, you multiply this by the ionising dose in krad. For our example (1.5 krad), one arrives at 3.9E-4 nA/cm^2 at -50 $^{\circ}$C. This is for a conventional CCD clocked normally - not inverted, and no dither clocking.

These damage constants are plotted in Fig. 7.1, and predicted dark current as a function of temperature for this worked example is shown in Fig. 7.2 and Table 7.1. Note that the $T^{1.5}$ factor has been ignored for simplicity in both of these formulae. More precise formulae are given in Roy's thesis, 1992. The expressions given here are for simple order of magnitude estimates.

7.2.3   Estimate of flat-band voltage shift

For the worst case situation - device biased and cold during irradiation - a figure of 120 mV/krad (Robbins 1992) can be used for EEV devices which are not radiation hardened. For our example, this corresponds to a voltage shift of 0.18 V. Such a change will have no effect on device operation.
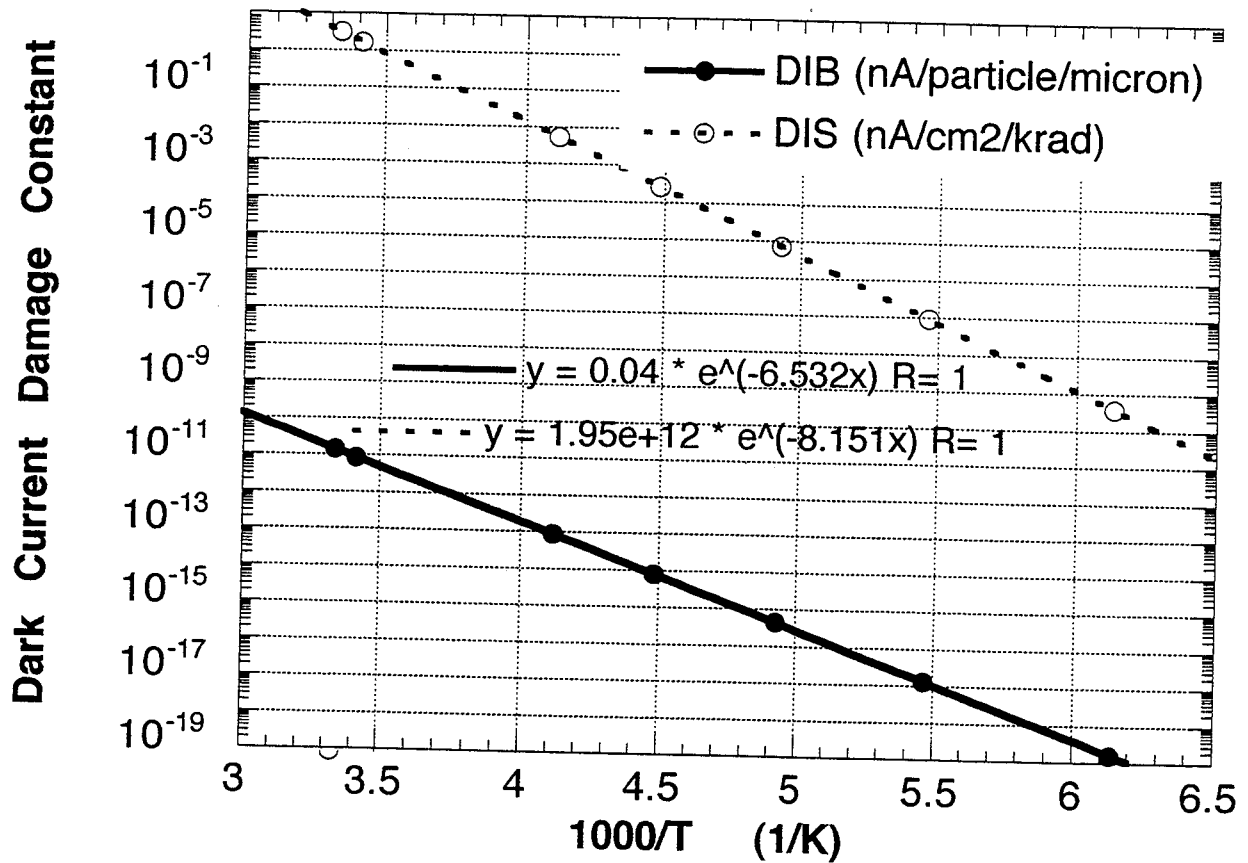
Fig 7.1 Dark current damage constants - surface and bulk components

Estimated dark current from engineering formulae
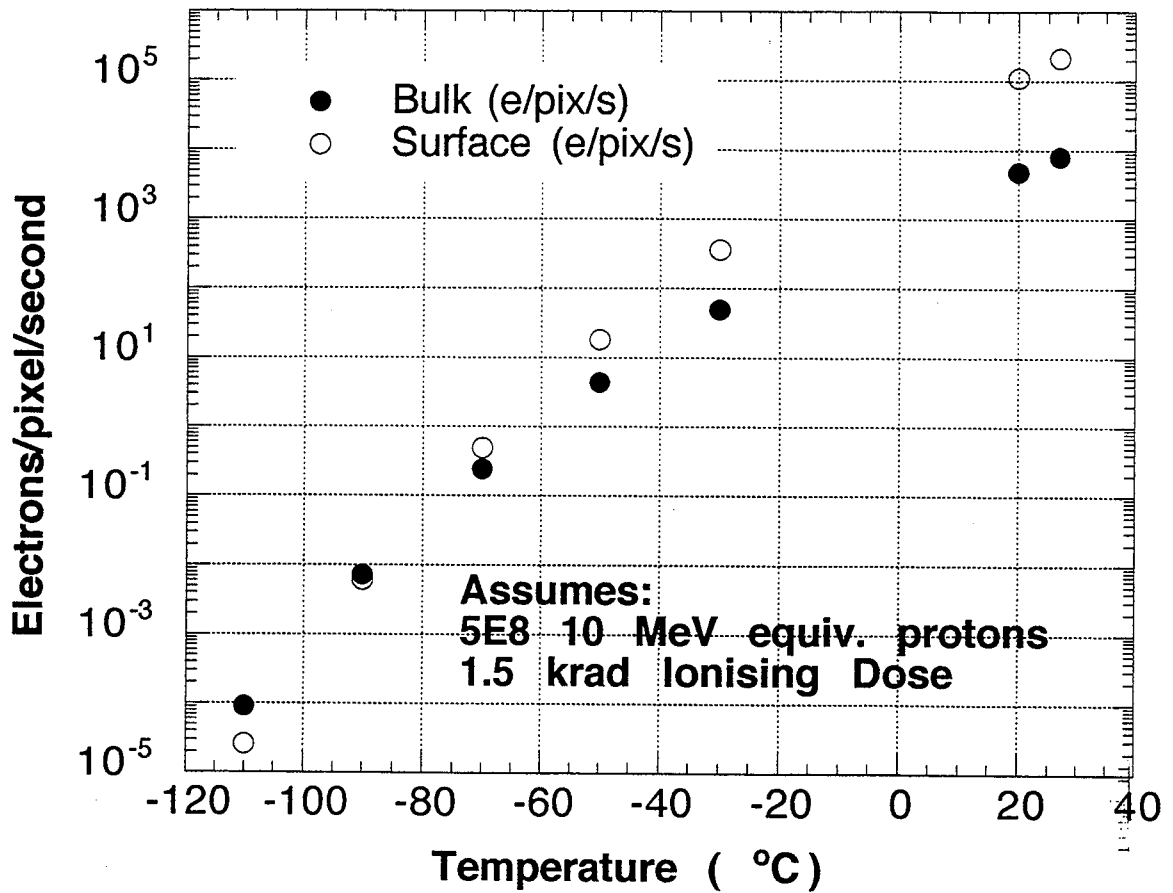
Fig 7.2 Example of predicted dark current for given radiation environment

8. RECOMMENDATIONS

8.1 General

The experience of the present authors derived from this project, the EPIC camera development, microstrip development and a number of CCD technology evaluations, can be focussed into a number of specific recommendations. These would concern (a) more penetrating methods for establishing the tolerance of CCD devices to radiation in the various stages of evaluation, production screening and lot acceptance. (b) CCD design concepts for devices more tolerant of bulk damage (c) similar concepts for devices which are more tolerant of inonization effects (due to electrons and bremsstrahlung). The recommendations listed below concentrate on type (a) , although (b) has been touched on in Section 4.5 and Section 5. Item (c) falls outside the need of XMM because of the position of cameras in the spacecraft.

A considerable number of topics within these headings have suggested themselves to us. The Present project has addressed some of these problems but cannot claim to have solved them all. Understanding in all of these problem areas should be made to evolve continuously as far as it can within the effort available.

8.2. Work needed on physical problems - all come under the umbrella of "defect engineering"

Spread of CTI and dark current damage with process batch and chip technology -characterisation of wafers before and after processing.

Comparison of damage values at cryogenic vs. room temperature

Characterization of the electron and hole traps in CCDs and suitable test structures - Trap spectroscopy by DLTS etc.

Temperature dependence of CTI +20 to -150 degC - especially use of the periodic pulse technique.

Effect of implant type and anneal

Surface Interface states and oxide charge concentration

Sources of dark current - especially hot-spots and RTS behaviour.

8.3 Work needed on test techniques

CCD modelling - CTI correction and defect kinetics models

CCD irradiation at incidence angle other than normal

Optimization of irradiation source

Optimization of test chambers

Bulk damage monitors (p-i-n diode , Brunel/Leicester Bulk Damage Monitor)

MOS dosimeters

8.4 Work needed on practical system hardening techniques

Annealing by long - term, low - level heating

Lowering temperature of operation (defect freeze-out)

Optimization of "fat zero" technique and CTI correction algorithms.

Flight experiments (see Brunel/Leicester Bulk Damage Monitor)

Bombardment of large samples under 10 MeV protons

Development of an acceptance test routine

8.5 Specific recommendations on device testing, fabrication and use

In future testing of CCDs, the following recommendations are made.

1. The use of X-rays to characterize CCDs is simple and functional but contains some inaccuracies (described in Chapter 4) which encourage parallel use of another method, namely electrical charge injection. We recommend the incorporation of simple charge injection structures suitable for CTI measurement by the well-established periodic pulse technique.

2. In order to separate bulk and surface contributions to dark current, the well-established elevated temperature static dark current measurement should be refined. This is an example of a parametric test requiring little equipment which can extract vital information about CCD performance. Such tests are probably suitable for lot acceptance.

3. Bulk dark current in inverted mode devices needs to be studied in light of the results of this work especially the annealing behaviour.

4. This report has shown new avenues for investigating hot spikes and flickering pixels. Room temperature measurements and short annealing studies could help to reveal the nature of the responsible defect(s).

5. For laboratory evaluation studies, alpha and neutron sources are more economical than proton machines. Apart from cost, the other advantage of a neutron source is the significant reduction of the ionising dose which creates surface state induced dark current. Both of these sources are particularly useful for investigating hot spikes.

6. It is fair to say that the QUALITY CONTROL tools for characterization of the stock silicon wafers used in CCD manufacture are not yet adequate to the present task. The cross-fertilisation of concepts and results (especially DLTS) from damage studies of high resistivity PN diodes, as noted in this report, suggests that the fabrication of simple diodes on the same material as used for CCDs would prove to be a useful and economical characterization tool.

7. The dark current responsivity to protons is considerably higher than expected with respect to the surface component. This may be due to a dependence of the creation of interface states on the LET of the bombarding particle. To our knowledge, this has not been observed before and requires more study. This could be followed up by measurements with CCDs and MNOS capacitors using particle beams of varying energy and type.

8. The variance in the CTI damage of Type CCD02 results is large and for the moment, impedes the planning of a straightforward screening or lot acceptance method for CCDs.

The devices using SBC technology appear to show less variation. As lot acceptance requires sampling we suggest that several SBC devices are now studied for CTI variation.

9. On the basis of one device it appears that the CTI radiation tolerance of high resistivity float-zone material may be better than epitaxial silicon. This should be investigated further. We believe this is due to lower boron and carbon levels in the FZ material.

10. During this project, we discovered a defect centre, EM2 (Section 4.11), which increases the serial CTI when the device is annealed at +130 ^{o}C. This could cause "overanneal" if attempting to recover performance by heating in orbit. The problem is material dependent. We suggest the use our growing knowledge of defect engineering to eliminate this defect from the CCD channel if possible. This is one of the pieces of technological research which is best performed using the periodic pulse technique -recommendation 1 - and DLTS studies on diodes. The issues of when to anneal, how many times and for how long, need further investigation.

11. Another piece of defect engineering suggested is the complete alteration of the dopant in the buried channel. Other n-type implants may be tested but it is thought likely that the best approach is the radical one of a "buried p-channel CCD", using boron in the place of phosphorus.

12. CCD output amplifiers have significantly improved in recent years. EEV's buried-channel output amplifier version of the CCD28 achieves 27 electrons noise with a 10 MHz clock rate. As Section 4.4 showed, asymmetric clocking improves the CTI for small signals. Such clocking and higher rate operation would provide modest but useful improvements in CTI damage factors.

13. The CTI correction algorithm gave some improvement in the X-ray energy resolution. It needs much further work before it can be used with real data - e.g. how to handle several X-ray lines and include the signal size dependence of the CTI.

These recommendations could form the backbone of a programme supported by space users (tracker systems as well as science projects) and manufacturers.

9. CONCLUSIONS

The project described above covers two phases of the investigation of radiation effects in cryogenic CCDs used for X-ray sensing in space science missions. The first part (Work Order 1) was managed by BNF-Fulmer using 10 MeV protons, which are taken to be representative of the particle exposure expected at the focus of an X-ray telescope in one of the preferred scientific observation orbits. The contract was passed to Brunel University and work was continued (under Work Order 2).

The present report summarizes the earlier work where relevant but concentrates on the work done by Brunel and Leicester University over the past year. The work has improved our knowledge of the latest, large CCD chips and characterized the EEV technology more fully. Cross-fertilzation has come from related projects in university and industry.

The formulation of lot acceptance tests which assure performance of X-ray telescopes despite damage to CCD efficiency during very severe solar flare events has, however, been somewhat disturbed by the degree of chip to chip variance in one of our tests, namely the puzzling variation in the CCD02 CTI results. The devices using SBC technology , CCD12 and CCD15, showed less variation. Also the CCD12 open electrode device manufactured on high resistivity float-zone material appears to be more radiation tolerant than those made on epitaxial silicon. Finally, the increase in the surface current is high and needs to be understood at a more fundamental level.

Features of our findings which are of physical interest concern our understanding of ;

(a)   the defect picture in the silicon as it exists in the active region of CCDs including a proposed new defect, denoted EX.

(b)   the importance of photon hit rate and X ray energy in determining the CTI damage constant.

(c)   a theoretical model describing the effects of clock rate in the serial and parallel registers.

(d)   the phenomena ocurring during annealing at room temperature and high temperatures, including the sources of dark current in damaged CCDs.

During the project, we made recommendations for improved measurements and models which can be used in future CCD research.

The project has improved confidence that that a radiation tolerant system can be procured for X-ray astronomy, provided system hardening tools such as CTI prediction and control techniques are added to a good understanding of the physics of radiation effects in CCDs. There are still some steps to be taken in advanced CCD technology and lot control.

10. ACKNOWLEDGEMENTS

11 REFERENCES

C. Claeys, E. Simoen and J. Vanhellemont, Final Report on "The Radiation Hardening Study of Displacement Damage in Silicon", Report No. P35278-IM-RP-0012, IMEC, Leuven, Feb. 1994.

G. Davies, E.C. Lightowlers, D. Griffiths and J.G. Wilkes (1987a). "Room-temperature irradiation of silicon doped with carbon". Semicond. Sci. Technol, 2, 554-7 (1987).

G. Davies, E.C. Lightowlers, R.C. Newman and A.S. Oates (1987b). "A model for radiation damage effects in carbon doped crystalline silicon". Semicond. Sci. Technol, 2, 524-32 (1987).

C. Dale, P. Marshall, B. Cummings, L. Shaney and A. Holland, (1993). "Displacement damage in mixed particle environments for shielded spacecraft CCDs". IEEE Trans. Nucl. Sci., NS-40 (6) 1628-37 (Dec 1993).

ESA 1989, "Radiation Design Handbook", ESA PSS-01-609 (European Space Agency), 1991

A. Holland (1993). "The effect of bulk traps in proton irradiated EEV CCDs". NIM A326 335-343 (1993).

A. Holland (1991). "The annealing of proton induced damage in CCDs for space use". Inst. Phys. Conf. Series, 121 33-40 (1991).

A. Holmes-Siedle and L. Adams (1993). "Radiation effects handbook" (Oxford University Press, Oxford UK 1993).

A. Holmes-Siedle, A. Holland and S.J. Watts (1994), "The irradiation, measurement and technology evaluation of X-ray sensitive CCDS for ESA scientific missions", WO1 Report, ESTEC Contract no. 8815/90/NL/PB(SC), Brunel University, UXBRIDGE UB8 3PH, England (May 1, 1995).

A. Holmes-Siedle, A. Holland and S.J. Watts (1994), Radiation experiment test plan, ESTEC Contract no. 8815/90/NL/PB(SC), Brunel University, UXBRIDGE UB8 3PH, England (Oct 12, 1994).

A. Holland, Holmes-Siedle, B. Johlander and L. Adams, "Techniques for minimizing proton damage in scientific charge-coupled devices", IEEE Trans. Nucl. Sci., NS-38 (6) 1663-1670 (Dec 1991)

A. Holmes-Siedle (1991). Final Report, Work Order 1, ESTEC Contract 8815 (BNF-Fulmer Research, Wantage, UK, 1991).

I. Hopkins, G. Hopkinson(1993) "Random telegraph signals from proton-irradiated CCDs" IEEE Trans, Nucl. Sci, NS-40 (6) 1567-74 (1993)

I. Hopkins, G. Hopkinson and B. Johlander (1944), "Proton induced charge transfer degradation in CCDs for near-room temperature applications". IEEE Trans, Nucl. Sci, NS-41 (6) 1984-91 (1994)

G. Hopkinson (1991). Final Report. "Proton radiation testing of CCDs for the SILEX programme", Report on ESTEC Order No. 103607 (SIRA Research and Development, CHISLEHURST, KENT UK, August1991)

G. Hopkinson (1992). Final Report. "Radiation testing of EEV CCDs for the MERIS programme", ESTEC Contract No. 9557/91/NL/LC(SC).(SIRA Research and Development, Chislehurst, Kent, UK, August1992)

G. Hopkinson (1995). Final Report. "CCD Radiation Damage Study", ESTEC Contract No. 9557/NL/LC(SC).

J. Janesick, T Elliott, and F Pool, "Radiation Damage in Scientific Charge-Coupled Devices", IEEE Transactions on Nuclear Science, Vol. 36, No. 2, Feb. 1989

J. Janesick "Sandbox CCDs", SPIE Conference, February 1995.

F. Jansen and J.W. den Herder (1995). "Report on X-ray and gamma ray induced radiation defects in CCDs" Report RGS-SRU-RD-95004, SRON, Utrecht, The Netherlands, April 1995.

Z. Li, H.W. Kraner, E. Verbitskaya, V. Eremin, A. Ivanov, M. Rattagi, P.G. Rancoita, F.A. Rubinelli and S.J. Fonash, C. Dale and P. Marshall (1992). "Investigation of the Oxygen-Vacancy (A-center) Defect complex profile in neutron irradiated high resistivity silicon junction particle detectors". IEEE Trans. Nucl. Sci., NS-40 (6) 1730-8 (Dec 1992).

T.P Ma and P.V. Dressendorfer (1991), Ionizing radiation effects in MOS devices" (Wiley New York 1991)

J. Matheson, M. Robbins, S. Watts (1995), "The effect of radiation induced defects on the performance of high resistivity diodes", RD20 Technical Report No 36, January 1995.

G. Messenger (1967), "A two-level model for lifetime reduction processes in neutron irradiated silicon and germanium", IEEE NS 14 (1967).

G. Messenger and M.S. Ash (1989). "The effects of radiation on electronic systems" (Wiley, New York 1989)

M. Robbins (1992). PhD Thesis, "Radiation Damage Effects in Charge Coupled Devices" Brunel University, July 1992.

T. Roy (1994). PhD Thesis, "Ionizing Radiation Induced Surface Effects in Charge Coupled Devices" Brunel University, Sept. 1993.

T. Roy, S. Watts, D. Wright, (1989) "Radiation Damage effects on imaging charge coupled devices", Nucl. Instr. Meths A275 545-557 (1989).

Z. Su et al. (1990), "Determination of oxygen in silicon by the ratio of A center to E center", J. Appl. Phys., 67, 1903, (1990).

P.W.A.M. Verhoeve et al (1992). "The development of back-illuminated CCDs for XMM ". In ESA-SP-356 "Photon detectors in space" (ESA Dec 1992)

S. Watts, " Overview of radaition damage -microscopic behaviour", Workshop on Radiation Hardening of Silicon Detectors, CERN, Geneva Oct 3-4 1995.

S. Watts, A. Holmes-Siedle and A. Mohammadzadeh (1995). Radiation damage evaluation of Loral CCDs for the VIMS-V channel on the Cassini spacecraft". Report No., BRUCRD-95-4 (Brunel Centre for Radiation Damage Studies , Uxbridge, UK, August 1995)

APPENDIX

Data Tables of measurements on shielded and irradiated areas of EEV CCDs at -70, -90 and -110 °C. 6.25 MeV protons, Birmingham 4th Quarter 1995, WO2 ESA Contract 8815.

TABLE 1. CCD02-1

Temp (°C)	1.46x10⁹ cm⁻² (10MeV equiv.)			Shielded		
	CTIs (x10⁻⁶)	CTIp (x10⁻⁶)	FWHM (eV)	CTIs (x10⁻⁶)	CTIp (x10⁻⁶)	FWHM (eV)
-70	350	400	-	25	27	-
-90	140	330	-	30	27	-
-110	110	125	234	12	18	200
-130	224	74	226	13	15	176

TABLE 2. CCD02-2

Temp (°C)	1.48x10⁹ cm⁻² (10MeV equiv.)			Shielded		
	CTIs (x10⁻⁶)	CTIp (x10⁻⁶)	FWHM (eV)	CTIs (x10⁻⁶)	CTIp (x10⁻⁶)	FWHM (eV)
-70	171	535	770	5	16	167
-90	128	471	677	25	19	172
-110	123	137	371	35	16	161
-130	115	63	238	40	12	214

TABLE 3. CCD02-3

Temp (°C)	1.43x10⁹ cm⁻² (10MeV equiv.)			Shielded		
	CTIs (x10⁻⁶)	CTIp (x10⁻⁶)	FWHM (eV)	CTIs (x10⁻⁶)	CTIp (x10⁻⁶)	FWHM (eV)
-70	147	481	779	64	15	167
-90	128	318	585	34	15	169
-110	114	142	289	27	12	159
-130	131	93	232	22	20	227

TABLE 4. CCD02-4

Temp (°C)	1.41x10⁹ cm⁻² (10MeV equiv.)			Shielded		
	CTIs (x10⁻⁶)	CTIp (x10⁻⁶)	FWHM (eV)	CTIs (x10⁻⁶)	CTIp (x10⁻⁶)	FWHM (eV)
-70	85	524	843	30	22	172
-90	115	367	555	36	19	164
-110	No data					
-130	117	53	236	84	24	190

TABLE 5. CCD02-5

Temp (°C)	1.46x10^9 cm^{-2} (10MeV equiv.)			Shielded		
	CTIs (x10^{-6})	CTIp (x10^{-6})	FWHM (eV)	CTIs (x10^{-6})	CTIp (x10^{-6})	FWHM (eV)
-70	122	593	970	20	22	175
-90	48	447	806	22	31	158
-110	33	156	361	18	10	168
-130	256	97	289	10	11	196

TABLE 6. CCD02-6 Device damaged - no data

Temp (°C)	1.44x10^9 cm^{-2} (10MeV equiv.)			Shielded		
	CTIs (x10^{-6})	CTIp (x10^{-6})	FWHM (eV)	CTIs (x10^{-6})	CTIp (x10^{-6})	FWHM (eV)
-70						
-90						
-110						
-130						

TABLE 7. CCD02-7

Temp (°C)	1.43x10^9 cm^{-2} (10MeV equiv.)			Shielded		
	CTIs (x10^{-6})	CTIp (x10^{-6})	FWHM (eV)	CTIs (x10^{-6})	CTIp (x10^{-6})	FWHM (eV)
-70	Dark current too high					
-90	138	599	1271	90	20	162
-110	72	573	842	25	19	154
-130	82	104	267	53	14	138

TABLE 8. CCD02-8

Temp (°C)	1.43x10^9 cm^{-2} (10MeV equiv.)			Shielded		
	CTIs (x10^{-6})	CTIp (x10^{-6})	FWHM (eV)	CTIs (x10^{-6})	CTIp (x10^{-6})	FWHM (eV)
-70	172	590	982	27	36	202
-90	117	487	790	27	33	198
-110	106	172	434	33	7	172
-130	175	83	261	~0	~0	195

TABLE 9. CCD02-9

Temp (°C)	1.22x10⁹ cm⁻² (10MeV equiv.)			Shielded		
	CTIs (x10⁻⁶)	CTIp (x10⁻⁶)	FWHM (eV)	CTIs (x10⁻⁶)	CTIp (x10⁻⁶)	FWHM (eV)
-70	33	582	1147	-	18	248
-90	34	471	906	63	32	193
-110	33	269	667	16	23	176
-130	116	88	315	~0	9	151

TABLE 10. CCD15-1

Temp (°C)	.53x10⁸ cm⁻² (10MeV equiv.)			1.0x10⁸ cm⁻² (10MeV equiv.)			Shielded		
	CTIs (x10⁻⁶)	CTIp (x10⁻⁶)	FWHM (eV)	CTIs (x10⁻⁶)	CTIp (x10⁻⁶)	FWHM (eV)	CTIs (x10⁻⁶)	CTIp (x10⁻⁶)	FWHM (eV)
-70	0	16	60	13	38	73	0	2	53
-90	7	15	53	19	30	59	0	1	48
-110	2	7	50	60	18	57	0	1	50
-130	10	3	41	76	12	59	0	2	44

TABLE 11. CCD15-2 Damaged bond wires after irradiation

Temp (°C)	1.3x10⁸ cm⁻² (10MeV equiv.)			2.6x10⁸ cm⁻² (10MeV equiv.)			Shielded		
	CTIs (x10⁻⁶)	CTIp (x10⁻⁶)	FWHM (eV)	CTIs (x10⁻⁶)	CTIp (x10⁻⁶)	FWHM (eV)	CTIs (x10⁻⁶)	CTIp (x10⁻⁶)	FWHM (eV)
-70									
-90									
-110									
-130									

TABLE 12. CCD15-3

Temp (°C)	2.4x10⁸ cm⁻² (10MeV equiv.)			6.5x10⁸ cm⁻² (10MeV equiv.)			Shielded		
	CTIs (x10⁻⁶)	CTIp (x10⁻⁶)	FWHM (eV)	CTIs (x10⁻⁶)	CTIp (x10⁻⁶)	FWHM (eV)	CTIs (x10⁻⁶)	CTIp (x10⁻⁶)	FWHM (eV)
-70	0	68	92	10	174	173	0	1	40
-90	0	59	73	18	164	165	0	0	42
-110	0	31	51	24	75	93	0	1	45
-130	1	12	46	4	32	58	0	1	44

TABLE 13. CCD12-1

Temp (°C)	.66x10^8 cm^{-2} (10MeV equiv.)			1.2x10^8 cm^{-2} (10MeV equiv.)			Shielded		
	CTIs (x10^{-6})	CTIp (x10^{-6})	FWHM (eV)	CTIs (x10^{-6})	CTIp (x10^{-6})	FWHM (eV)	CTIs (x10^{-6})	CTIp (x10^{-6})	FWHM (eV)
-70	9	14	144	0	34	165	18	3	142
-90	10	13	143	0	25	163	28	7	145
-110	18	10	143	5	21	146	30	9	148
-130	25	10	208	5	11	210	21	8	224

TABLE 14. CCD12-2

Temp (°C)	1.2x10^8 cm^{-2} (10MeV equiv.)			1.7x10^8 cm^{-2} (10MeV equiv.)			Shielded		
	CTIs (x10^{-6})	CTIp (x10^{-6})	FWHM (eV)	CTIs (x10^{-6})	CTIp (x10^{-6})	FWHM (eV)	CTIs (x10^{-6})	CTIp (x10^{-6})	FWHM (eV)
-70	0	19	178	0	37	190	14	5	183
-90	5	20	184	0	32	198	17	14	171
-110	Charge trailing became too severe for isolated events								
-130									

TABLE 15. CCD12-3

Temp (°C)	1.2x10^8 cm^{-2} (10MeV equiv.)			2.4x10^8 cm^{-2} (10MeV equiv.)			Shielded		
	CTIs (x10^{-6})	CTIp (x10^{-6})	FWHM (eV)	CTIs (x10^{-6})	CTIp (x10^{-6})	FWHM (eV)	CTIs (x10^{-6})	CTIp (x10^{-6})	FWHM (eV)
-70	11	21	162	42	40	200	11	12	158
-90	13	25	160	45	41	187	14	12	148
-110	8	19	176	24	13	168	14	15	164
-130	6	12	252	14	4	261	15	12	257

TABLE 16. CCD12-4

Temp (°C)	.84x10^8 cm^{-2} (10MeV equiv.)			2.0x10^8 cm^{-2} (10MeV equiv.)			Shielded		
	CTIs (x10^{-6})	CTIp (x10^{-6})	FWHM (eV)	CTIs (x10^{-6})	CTIp (x10^{-6})	FWHM (eV)	CTIs (x10^{-6})	CTIp (x10^{-6})	FWHM (eV)
-70	0	18	154	10	49	190	11	4	138
-90	1	28	150	12	46	196	12	8	137
-110	0	19	145	8	25	153	12	7	140
-130	9	7	202	0	8	198	19	7	196

TABLE 17. CCD12-5 Device with poor serial CTE - difficult to evaluate

Temp (°C)	4.2x10^8 cm^{-2} (10MeV equiv.)			6.6x10^8 cm^{-2} (10MeV equiv.)			Shielded		
	CTIs (x10^{-6})	CTIp (x10^{-6})	FWHM (eV)	CTIs (x10^{-6})	CTIp (x10^{-6})	FWHM (eV)	CTIs (x10^{-6})	CTIp (x10^{-6})	FWHM (eV)
-70	-	85	-	-	118	-	-	7	-
-90	-	63		-	91	-	-	2	-
-110	-	28		-	47	-	-	10	-

TABLE 18. CCD12-6

Temp (°C)	3.9x10^8 cm^{-2} (10MeV equiv.)			6.2x10^8 cm^{-2} (10MeV equiv.)			Shielded		
	CTIs (x10^{-6})	CTIp (x10^{-6})	FWHM (eV)	CTIs (x10^{-6})	CTIp (x10^{-6})	FWHM (eV)	CTIs (x10^{-6})	CTIp (x10^{-6})	FWHM (eV)
-70	0	75	241	85	101	326	29	5	183
-90	0	51	222	87	93	308	38	8	138
-110	12	33	206	34	34	223	28	6	145
-130	0	0	114	50	0	128	41	0	112

TABLE 19. CCD12-7 (Bulk)

Temp (°C)	1.1x10⁸ cm⁻² (10MeV equiv.)			5.4x10⁸ cm⁻² (10MeV equiv.)			Shielded		
	CTIs (x10⁻⁶)	CTIp (x10⁻⁶)	FWHM (eV)	CTIs (x10⁻⁶)	CTIp (x10⁻⁶)	FWHM (eV)	CTIs (x10⁻⁶)	CTIp (x10⁻⁶)	FWHM (eV)
-70	21	15	177	39	100	215	21	15	209
-90	6	15	173	27	22	193	23	10	197
-110	13	10	146	0	12	149	0	10	152
-130	7	9	187	0	6	178	0	7	189

TABLE 20. CCD12-10a

Temp (°C)	0.58x10⁸ cm⁻² (10MeV equiv.)			Shielded		
	CTIs (x10⁻⁶)	CTIp (x10⁻⁶)	FWHM (eV)	CTIs (x10⁻⁶)	CTIp (x10⁻⁶)	FWHM (eV)
-70	17	21	145	0	4	121
-90	19	20	147	0	5	125
-110	16	14	140	0	6	138
-130	60	26	220	0	23	240

TABLE 21. CCD12-10b

Temp (°C)	2.4x10⁸ cm⁻² (10MeV equiv.)			Shielded		
	CTIs (x10⁻⁶)	CTIp (x10⁻⁶)	FWHM (eV)	CTIs (x10⁻⁶)	CTIp (x10⁻⁶)	FWHM (eV)
-70	60	90	257	0	8	127
-90	50	67	217	0	9	135
-110	20	34	182	0	10	169
-130	30	37	400	0	29	414

TABLE 22. CCD12-10c

Temp (°C)	6.3x10⁸ cm⁻² (10MeV equiv.)			Shielded		
	CTIs (x10⁻⁶)	CTIp (x10⁻⁶)	FWHM (eV)	CTIs (x10⁻⁶)	CTIp (x10⁻⁶)	FWHM (eV)
-70	36	161	588	0	5	119
-90	50	143	480	0	8	122
-110	28	75	190	0	11	137
-130	21	40	238	11	19	235